Spring 1-1-2010

Two-Species Ion Arrays for Quantum Logic Spectroscopy and Entanglement Generation

David Brian Hume
david.hume@colorado.edu

Two-Species Ion Arrays for Quantum Logic Spectroscopy and Entanglement Generation

by

David B. Hume

B.S., University of Kentucky, 2002

A thesis submitted to the

Faculty of the Graduate School of the

University of Colorado in partial fulfillment

of the requirements for the degree of

Doctor of Philosophy

Department of Physics

2010

This thesis entitled:
Two-Species Ion Arrays for Quantum Logic Spectroscopy and Entanglement Generation
written by David B. Hume
has been approved for the Department of Physics

David J. Wineland

Dr. Neil Ashby

Date

The final copy of this thesis has been examined by the signatories, and we find that both the content and the form meet acceptable presentation standards of scholarly work in the above mentioned discipline.

Hume, David B. (Ph.D., Physics)

Two-Species Ion Arrays for Quantum Logic Spectroscopy and Entanglement Generation

Thesis directed by Dr. David J. Wineland

The quantum states of trapped atomic ions can be highly isolated from external perturbation, and precisely manipulated with applied laser fields. This makes them an excellent medium for quantum-limited experiments such as quantum information processing and precision spectroscopy. A relatively small number of ion species have been used for these types of experiments because most species are difficult to laser cool and detect directly. This thesis demonstrates a way to overcome this limitation by use of sympathetic cooling and state detection based on quantum logic. We apply these techniques to mixed-species arrays of $^{27}Al^{+}$ and $^{9}Be^{+}$ ions. A mathematical model for the motion of such a two-species array is presented in order to explore some features of the ion dynamics that are relevant for the experiments. Repetitive quantum nondemolition measurements of the electronic states of a $^{27}Al^{+}$ ion show detection fidelities as high as 99.94 %. We also demonstrate the simultaneous detection of two $^{27}Al^{+}$ ions and observe a detection fidelity of 99.8 %. The basic ideas behind the detection strategy are extended to potentially enable similar experiments on a more general class of atomic and molecular ions.

We have also investigated, theoretically and experimentally, a method for preparing entangled Dicke states in trapped atomic ions. We consider a linear chain of N ion qubits that is prepared in a particular Fock state of motion, $|m\rangle$. The m phonons are removed by applying a laser pulse globally to the N qubits, and converting the motional excitation to m flipped spins. The global nature of this pulse ensures that the m flipped spins are shared by all the target ions in a state that is a close approximation to the Dicke state $|D_N^{(m)}\rangle$. We calculate numerically the fidelity limits of the protocol and find small deviations from the ideal state for $m = 1$ and $m = 2$. We have demonstrated the basic features of this protocol by preparing the Bell state $|D_2^{(1)}\rangle$ in two $^{25}Mg^{+}$ target ions trapped simultaneously with an $^{27}Al^{+}$ ancillary ion.

Dedication

For Addie.

Acknowledgements

The work described in this thesis comes from a collaboration of many excellent scientists. In particular I owe a huge amount of gratitude for the hard work and patience of my closest advisors, Dave Wineland and Till Rosenband, without whom nothing in the experiment would have ever worked. Their technical expertise, creativity and nuanced knowledge of physics have guided this project from the start. I am also greatly indebted to Chin-Wen "James" Chou, Piet Schmidt and Jeroen Koelemeij, who worked skillfully, tirelessly (and even cheerfully!) to make the aluminum clocks tick. I would like to give a special thanks to Jim Bergquist who has generously shared his knowledge, hard work and encouragement to help me at every step along the way. Many more people have contributed to designing, building, operating and troubleshooting the experiment. Listing all of their names and contributions would really boost my page count, but I don't want to risk leaving anyone out, so instead I will just acknowledge all of the past and current members of the ion storage group collectively. Over the years, the people in the group have been a consistent source of ideas and inspiration as well as experimental support. I also want to acknowledge the work of the members of the Optical Frequencies Measurement Group at NIST, which has been essential for much of the work in this thesis. In addition, Neil Ashby who has served as my titular advisor, has been a valuable source of scientific guidance.

Just as important has been the support of my friends and family who saw me through graduate school with an incredible amount of love, understanding and grace. In particular I want to thank Lenore Sparks who (1) physically sat me down and forced me to dictate the really onerous parts of the dissertation while she dutifully typed them, (2) proof-read the whole mess of it when it came down to do-or-die time and (3) dragged me multiple times from my disintegrating shack in Eldorado Springs where I would hide from

anything thesis-like. My parents and brother performed similarly heroic tasks. I really hope someday I can return the favors. Thanks!

Contents

Figures

Figure

Chapter 1

Introduction

Quantum theory describes the behavior of the physical world at a fundamental level. Despite being supported by precise measurements on a vast range of physical systems, it continues to confound human imagination with seemingly bizarre implications. For example, the Copenhagen interpretation of quantum mechanics seems to imply the existence of nonlocal effects [Bell 64] - a condition challenged historically as unphysical [Einstein 35]. However, this property of quantum mechanics has been confirmed repeatedly in measurements with increasing accuracy [Aspect 82, Rowe 01], making it an accepted aspect of the theory if not completely understood. At the same time, quantum mechanical effects play an increasingly central role in the technology that drives the modern world. The band structure of semiconducting materials arises from a quantum mechanical description of the electrons in crystalline materials and is central to the operation of semiconducting devices such as the transistors in computer chips. These aspects of quantum theory makes it simultaneously one of the most confirmed, debated, applied and misconstrued discoveries of science.

From the original conception of quantum theory, atomic spectroscopy has played a central role in motivating its development and confirming its predictions. Measurements in atomic spectroscopy, particularly observations of the spectra of atomic hydrogen, guided the formulation of the Bohr atom in 1913 - a direct precursor to the formal quantum theory developed in subsequent years. Likewise, precise observations of the hyperfine splitting in hydrogen [Lamb 47] presented a puzzle to physicists in the 1940's that was explained with the development of quantum electrodynamics (QED). The predictions of QED continue to be tested with improved precision in atomic physics labs.

Conversely, theoretical developments in quantum theory have given rise to ground breaking progress

in atomic spectroscopy. In 1917 Albert Einstein wrote a paper, "On the quantum theory of radiation" [Einstein 17], which showed theoretically the necessity for stimulated emission of radiation. This concept laid the foundation for the eventual amplification of radiation through stimulated emission, first with the invention of the ammonia maser [Gordon 54] then with its optical counter part, the laser [Maiman 60]. Since that time, the laser has become a bedrock tool for the study of atomic systems. The spatial and temporal coherence of laser light give rise to an array of techniques that together have improved numerous aspects of atomic spectroscopy.

In this way, quantum theory and atomic spectroscopy have often played a complementary role in pushing forward our understanding of the physical world and improving our ability to interact with it. The interplay between these two scientific programs has been invaluable to both, and the symbiotic relationship is likely to continue far into the future. Currently, the breadth of applications and the achievable performance in atomic spectroscopy is increasing rapidly. A relevant example is the recent development of optical atomic clocks, which combine advances in laser stability and laser frequency measurements with newly developed techniques in the trapping and cooling of atoms and ions to produce clocks that have demonstrated performance exceeding that of existing microwave frequency standards.

On the other side, quantum mechanics has undergone a revolution in the past couple of decades with the advent of quantum information processing (QIP) theory. This is the study of how information behaves and can be manipulated when encoded in coherent quantum states. It has implications for encryption, computation, metrology and quantum simulation. Again here, atomic spectroscopic techniques are central to some efforts to realize the protocols in QIP. Likewise, the theoretical developments in QIP motivate novel and challenging experiments in atomic physics, sometimes providing researchers with new avenues for experiments or a new perspective on the physical systems they investigate.

In this thesis I describe a set of experiments that, along with a diversity of other experimental efforts underway, lie at the intersection of QIP and precision spectroscopy. I believe the work reflects on the continued interaction between developments in quantum mechanics and experimental atomic physics. In particular, we demonstrate how techniques developed in the context of QIP can also be applied to enable precision spectroscopy on an interesting atomic system. We apply QIP techniques in an ion trap to enable

the detection of electronic states $^{27}Al^+$ (Ch. 5), enabling precision spectroscopy of the $^1S_0 \rightarrow ^3P_0$ "clock" transition. Reapplying the same capabilities in a different experiment, we use $^{27}Al^+$ as an ancillary ion to entangle the internal states of two $^{25}Mg^+$ (Ch. 6). To motivate these experiments I will first introduce the ideas behind single-ion optical clocks and ion trap quantum computing.

1.1 Single-Ion Optical Clocks

The Bureau International des Poids et Mesures (BIPM) is responsible for defining the SI system of units. Since 1967 the second has been defined based on a resonance frequency in atomic cesium[1] :

> The second is the duration of 9192631770 periods of the radiation corresponding to the transition between the two hyperfine levels of the ground state of the caesium 133 atom.

By defining the speed of light in vacuum as $c = 299792458$ m/s, atomic clocks also provide the basis for the definition of the meter. Since these base units, the meter and the second, both appear in many derived units (i.e. Hz = 1/s) thinking of atomic clocks as timekeeping devices is an oversimplification. Much of the motivation for improving the stability and accuracy of atomic clocks is not directly related to timekeeping, since the signals from state-of-the art clocks are not maintained continually and the distribution of the signals globally is subject to various inaccuracies. However, stable atomic clocks have been applied to a variety of important technological problems such as network synchronization and precise satellite navigation as required, for instance, in GPS satellites. They have been central to tests of Einstein's relativity theory [Hafele 72, Vessot 80]. Since the development of the first atomic clocks they have been continually improved, both in terms of their frequency stability and their absolute accuracy[2] . State-of-the-art cesium fountain clocks use laser-cooled atoms and exhibit fractional frequency inaccuracies below 5×10^{-16} [Parker 10] dominated by frequency shifting effects such as Stark shifts due to background blackbody radiation [Itano 82]. Frequency stability of Cesium fountain clocks has been reported in the range of 4×10^{-14} at a one second integration time [Santarelli 99], averaging in time according to the Allan deviation as $\sigma_y(\tau) \propto 1/\sqrt{\tau}$, where τ is the total measurement duration.

[1] This is the official English translation of the French text published by BIPM. It specifically refers to a cesium atom at rest and and at a temperature of 0 K.

[2] For readers interested in an accessible history of atomic clocks and atomic timekeeping I recommend *Splitting the second: the story of atomic time* by Tony Jones [Jones 00].

Recently, a new generation of atomic clocks based on optical transitions in trapped atoms or ions (optical clocks) have been developed that demonstrate higher accuracy and stability than the Cesium fountains. Although the potential for high accuracy optical clocks was recognized in the pioneering efforts of Hans Dehmelt as early as 1981 [Dehmelt 81], the experimental demonstrations have been enabled by recent advancements of several techniques in atomic physics. For example, laser cooling of trapped atoms to low temperatures allows for recoil-free optical spectroscopy. This suppresses inhomogeneous Doppler broadening of the optical resonance. In addition, it reduces small shifts of the atomic absorption spectrum due to relativistic time dilation. As another example, the improvement of laser stabilization [Young 99] by use of isolated, ultra-high finesse optical cavities has been key for the measurement of narrow optical resonances. Laser stabilization remains an important area of research for further improving optical clock performance. Finally, the invention of the self-referenced femtosecond frequency comb [Jones 00] has simplified the measurement of optical frequencies. In a relatively compact and reliable package these lasers transfer the stability of an optical signal into the electronically countable radio frequency (RF) domain[3] .

Clock performance is quantified primarily on the basis of accuracy and stability, both being normalized to the center frequency of the atomic resonance. The inaccuracy of a clock quantifies how well systematic shifts to the clock frequency are characterized. Generally, these frequency shifts are calibrated through separate measurements, theoretical considerations, and sometimes by periodically monitoring the shifts during clock operation. The clock stability, on the other hand, quantifies the magnitude of random statistical noise in the clock frequency. It is typically characterized in terms of the Allan deviation. Ultimately the stability of a clock is limited by quantum projection noise, and the Allan deviation in this case is given by

$$\sigma_y(\tau) \approx \frac{\Delta\nu}{\pi\nu_0}\sqrt{\frac{T_c}{\tau N}} \tag{1.1}$$

where $\Delta\nu$ is the linewidth of the transition at frequency ν_0, T_c is the experimental cycle time, τ is the averaging time and N is the number of atoms probed simultaneously. The higher frequency, ν_0, of an optical atomic clock, being many orders of magnitude greater than a microwave clock, is the central feature that leads to higher stability and accuracy.

[3] Before the invention of the femtosecond laser frequency comb optical frequencies could only be counted through a complicated mechanism by which signals between the optical and RF domains where phase-locked in stages.

Most optical clock experiments currently underway take one of two primary approaches. One is based on individual atomic ions trapped in a RF Paul trap, like the experiments of this thesis, while the other is based on an atomic ensemble trapped in an optical lattice. Each of these approaches offers a number of basic advantages and disadvantages that affect various performance characteristics and have a bearing on other practical considerations. One attractive feature of an ion optical clock, is that the ion's charge provides a means for trapping it and precisely controlling its position. With an RF Paul trap, trap depths on the order of ~ 1 eV and secular mode frequencies above 1 MHz can be achieved. The trap depth ensures that long interaction times can be achieved between an ion and an applied electromagnetic pulse during spectroscopy. For example, the typical lifetime of a laser-cooled ion in a room-temperature trap is on the order of an hour (often limited by chemical reactions with residual hydrogen in vacuum) while the interrogation pulse time is currently limited by laser instability to ~ 300 ms. This interrogation time leads to Fourier transform limited linewidths on the order of 1 Hz. The ion can remain trapped through many experimental cycles so that T_c does not include the extra time that would be required for reloading the ion. On the other hand, the Coulomb repulsion between ions limits the ion density that can be achieved. In fact, frequency shifts due to the presence of the RF trapping fields have forced the high-accuracy ion clocks developed so far to operate with a single ion (or a 1 dimensional array of a small number of ions) at the null of the trapping fields. With $N = 1$, the clock stability (Eq. 1.1) suffers compared to neutral atom clocks that typically have many thousands of atoms. Optical transitions in ions are typically at a higher frequency compared to neutral atoms (ultraviolet rather than visible frequencies) due to the higher nuclear charge.

Several ion systems have been investigated as a frequency reference for an optical atomic clock, including Hg^+, In^+, Sr^+, and Yb^+. One motivation behind the experiments in this thesis is an optical clock based on $^{27}Al^+$, which is unique among ion clocks studied experimentally in that it does not have a suitable electronic structure to perform direct laser cooling and state detection. Instead laser cooling of Al^+ is performed sympathetically via the Coulomb interaction with a simultaneously trapped ion, which can be directly laser cooled. Although, we specifically study Al^+ for precision spectroscopy, similar techniques may be applied to other atomic and molecular ions. These ion species may be attractive for use as a frequency reference in an atomic clock or other precision spectroscopy experiments such as a search for the possible

time-variation of the fundamental constants. The basis for the techniques I describe is a procedure for mapping information in the electronic state of one ion, through a collective mode of motion and into the electronic state of the sympathetic cooling ion. These ideas were inspired by progress in the field of ion trap quantum computing, which I will introduce now.

1.2 Ion Trap Quantum Computing

The basic unit of information in a classical computer is the bit, which can take one of two values: 0 or 1. In analogy the basic unit of quantum information is the quantum bit or qubit. The qubit, like the classical bit, is a system containing two states: $|0\rangle$ and $|1\rangle$. However, unlike the classical bit, a qubit can exist in a superposition state $|\psi\rangle = c_0|0\rangle + c_1|1\rangle$, where the complex amplitudes obey $|c_0|^2 + |c_1|^2 = 1$. The Hilbert space of a qubit is conveniently represented by the Bloch sphere. In this representation $c_0 = \sin(\theta/2)$ and $c_1 = \cos(\theta/2)e^{i\phi t}$, such that ψ is specified by two parameters θ and ϕ corresponding to a point on a sphere of unit radius. From this representation it is clear that, whereas a classical bit occupies a discrete value, a qubit occupies a point in a continuous space.

Another key difference between quantum information and classical information relates to observation or measurement of a quantum state. In the Copenhagen interpretation, a superposition state "collapses" to a particular basis state when measured. For instance, a measurement on $|\psi\rangle$ yields the result $|0\rangle$ ($|1\rangle$) with probability $|c_0|^2$ ($|c_1|^2$). Since quantum measurement is a central theme in this thesis (Ch. 5) I will introduce it more formally here, following the treatment in [Nielsen 00]. Extending the Hilbert space of state $|\psi\rangle$ to arbitrary dimensions we can write,

$$|\psi\rangle = \sum_i c_i|\psi_i\rangle, \tag{1.2}$$

where we assume an orthonormal basis such that $\langle\psi_i|\psi_{i'}\rangle = \delta_{ii'}$ and $|\langle\psi|\psi\rangle|^2 = \sum_i |c_i|^2 = 1$. A projective measurement of ψ can be described in terms of a set of projection operators $\{\hat{P}_m\}$ with eigenvalues $\{m\}$. I assume that the decomposition of state ψ in Eq. 1.2 is done in terms of the measurement basis such that $\hat{P}_m = |\psi_m\rangle\langle\psi_m|$ and $\hat{P}_m\hat{P}'_m = \delta_{mm'}\hat{P}_m$. Then any measurement on $|\psi\rangle$ is described by the observable $\hat{O} = \sum_m mP_m$ and has an expectation value of $\langle\psi|\hat{O}|\psi\rangle$. Any individual measurement of $|\psi\rangle$, however, can give only a single result corresponding to a particular eigenvalue. Since I have defined the decomposition of

$|\psi\rangle$ in terms of the measurement basis, the outcome of the measurement will be m with probability $|c_m|^2$ and the quantum state after measurement will be $|\psi_m\rangle$. In this formal outline of a projective measurement it is typically assumed that the result of the measurement is unchanged by further application of $\hat{O}$ since the eigenvalue m will be observed with unit probability. In practice, this is a difficult experimental proposition, since quantum states are often perturbed by any interaction with the environment (or equivalently the experimental apparatus) as required by measurement. A measurement that does not perturb the projected quantum state has been termed a quantum nondemolition (QND) measurement, which I will examine in the context of trapped ion experiments in Ch. 5.

The physical interpretation of state projection during measurement has been the subject of significant debate, but here I consider it as a fundamental postulate of quantum theory. Independent of any interpretation, quantum state projection has profound implications in QIP, the recognition of which led to some of the first theoretical work in quantum information theory. A well-known example is the no-cloning theorem, first reported in 1982 [Wootters 82], which states that an arbitrary unknown quantum state cannot be copied. In quantum cryptography, information transmitted via coherent quantum states enables secure communication. Here, the no-cloning theorem forbids a potential eavesdropper from intercepting a quantum message, copying it, and sending one copy forward. Any attempt to gain information in this way can be detected due to the inevitable state projection. The idea of secure communication by use of a quantum information channel was developed soon after the no-cloning theorem [Bennett 84].

Given the early results in quantum cryptography, it is natural to ask what other applications exist for quantum information. In particular, could a computer that processes quantum information give an advantage in efficiency over a classical computer? In 1985 David Deutsch studied this problem and discovered a simple example in which a quantum algorithm could outperform the best classical counterpart [Deutsch 85]. In the intervening years several important quantum algorithms have been developed. 1n 1994 Peter Shor discovered algorithms for prime factorization and computing the discrete logarithm [Shor 94], which are of great importance because they provide an exponential speed-up compared to the best classical algorithms for problems that are central in classical cryptography. These key results and others have motivated the continued theoretical investigation of QIP.

In parallel, experimental groups around the world, working with a diverse array of physical systems have begun serious efforts to implement the basic building blocks of a quantum computer. Any physical system capable of QIP must meet a certain set of requirements related to qubit initialization, measurement, coherence, and interaction. One famous formulation of these requirements is called the Divincenzo Criteria [DiVincenzo 01]. An experimental effort to meet these requirements presents numerous challenges, not the least of which is the notoriously fragile nature of a quantum state. Any interaction between a qubit and the environment can collapse the qubit state, just like a measurement, causing decoherence. For this reason, the qubits in a quantum computer must be highly insulated from their environment, while allowing for strong interactions with the experimental systems that control the computation. This juxtaposition and other technical challenges have made progress in experimental quantum computing both difficult and interesting.

Despite the difficulties, basic demonstrations of QIP protocols have been made in several physical systems. Perhaps the most advanced of these efforts uses individual trapped ions to store information. This idea, originally proposed by Cirac and Zoller [Cirac 95], takes two spectroscopically isolated states in the atomic system as a qubit. Typically these states are initialized with optical pumping and measured with fluorescence detection. The qubit state of an individual ion can be manipulated by applying properly tuned laser pulses that rotate the qubit state on the Bloch sphere. The breakthrough in this proposal was a protocol for coupling the state of two ions stored in the same trap through a collective state of motion, to perform a two-qubit controlled-not (CNOT) gate. The CNOT gate is one member of a finite set of operations necessary for universal quantum computation, and, like the classical controlled-not gate can be summarized by the following truth table,

$$|00\rangle \rightarrow |00\rangle$$

$$|01\rangle \rightarrow |01\rangle$$

$$|10\rangle \rightarrow |11\rangle$$

$$|11\rangle \rightarrow |10\rangle.$$

Here the state of the two qubits is compressed into a single ket (i.e. $|0\rangle_1 \otimes |1\rangle_2 \equiv |01\rangle$). The first qubit is the "control" qubit that modulates a bit flip on the second, "target" qubit. The quantum CNOT operation

can be used to entangle two quantum bits. If the initial state of the two qubits is $|\psi\rangle = 1/\sqrt{2}(|0\rangle + |1\rangle)|0\rangle$, after a CNOT gate, state will be $|\psi'\rangle = 1/\sqrt{2}(|00\rangle + |11\rangle)$. This is called an entangled state because it cannot be separated into the form $|\psi\rangle_1 \otimes |\psi\rangle_2$. In addition to being a basic building block for quantum computing experiments, the CNOT gate is the central operation that enables spectroscopy of Al^+ in this thesis. The current state of the art for ion trap QIP involves the entanglement of up to eight trapped-ion qubits [Leibfried 05, Häffner 05], and two-qubit CNOT gates with fidelities as high as 99.3 % [Leibfried 03, Benhelm 08]. Both of these are significant steps towards realizing practical applications of QIP. By contrast, the work I discuss involves operations that entangle only two qubits and require relatively low fidelity (in our case ∼85 %) to demonstrate precision spectroscopy on an otherwise inaccessible system. We have operated an atomic clock based on Al^+ in this way and have achieved inaccuracy as low as 8×10^{-18} and clock stability of 2.8×10^{-15} at a one second averaging time. More broadly, this shows, in principle, that the controlled interaction of two quantum systems can open new doors in the field of precision metrology. Whereas large-scale QIP requires the precise interaction of many quantum bits, applications in metrology are well within reach with the current state of the art.

Chapter 2

Laser Ion Interactions

2.1 Ion Energy Levels

The singly-ionized elements of group II in the periodic table (alkaline earth metals) have one electron in their outer shell, and thus exhibit a relatively simple atomic structure. In a general sense, this is the feature that allows them to be efficiently laser cooled and detected in single ion experiments and for that reason they are the ions most commonly used. $^9Be^+$ has a nuclear spin of $I = 3/2$ so its $^2S_{1/2}$ ground state splits into two hyperfine levels with F = 2 and F = 1 respectively. The relevant levels are shown in Fig. 2.1. With them I show the main atomic transitions used in our experiments and label the lasers used in addressing them as described in Sec. 3.2. We use two particular levels in the ground state $(F = 1, m_F = -1)$ and $(F = 2, m_F = -2)$ as a qubit. In the experiments the ions are subjected to a quantization magnetic field of 1 - 4 G, which causes Zeeman splitting of the m_F sublevels of the hyperfine manifolds so that they are spectroscopically resolved. At these magnetic fields the linear Zeeman effect is a good approximation to the energy shifts, which is given by $\Delta E = \mu_B g_F m_F B$, where B is the magnetic field magnitude, μ_B is the Bohr magneton, g_F is the g-factor for the hyperfine level (+1/2 or -1/2 for F = 2 and F = 1 respectively), and m_F is the Zeeman sublevel.

Aluminum has one naturally-occurring isotope with nuclear spin I = 5/2. The singly-ionized atom has two outer-shell electrons and thus exhibits a helium-like structure, with a $^1S_0$ ground state. It was chosen for our experiments because the $^1S_0 \rightarrow {}^3P_0$ transition is particularly well suited as a stable reference for an optical atomic clock [Rosenband 07, Rosenband 08, Chou 10]. The $^3P_0$ state has a lifetime of 20.6(1.4)

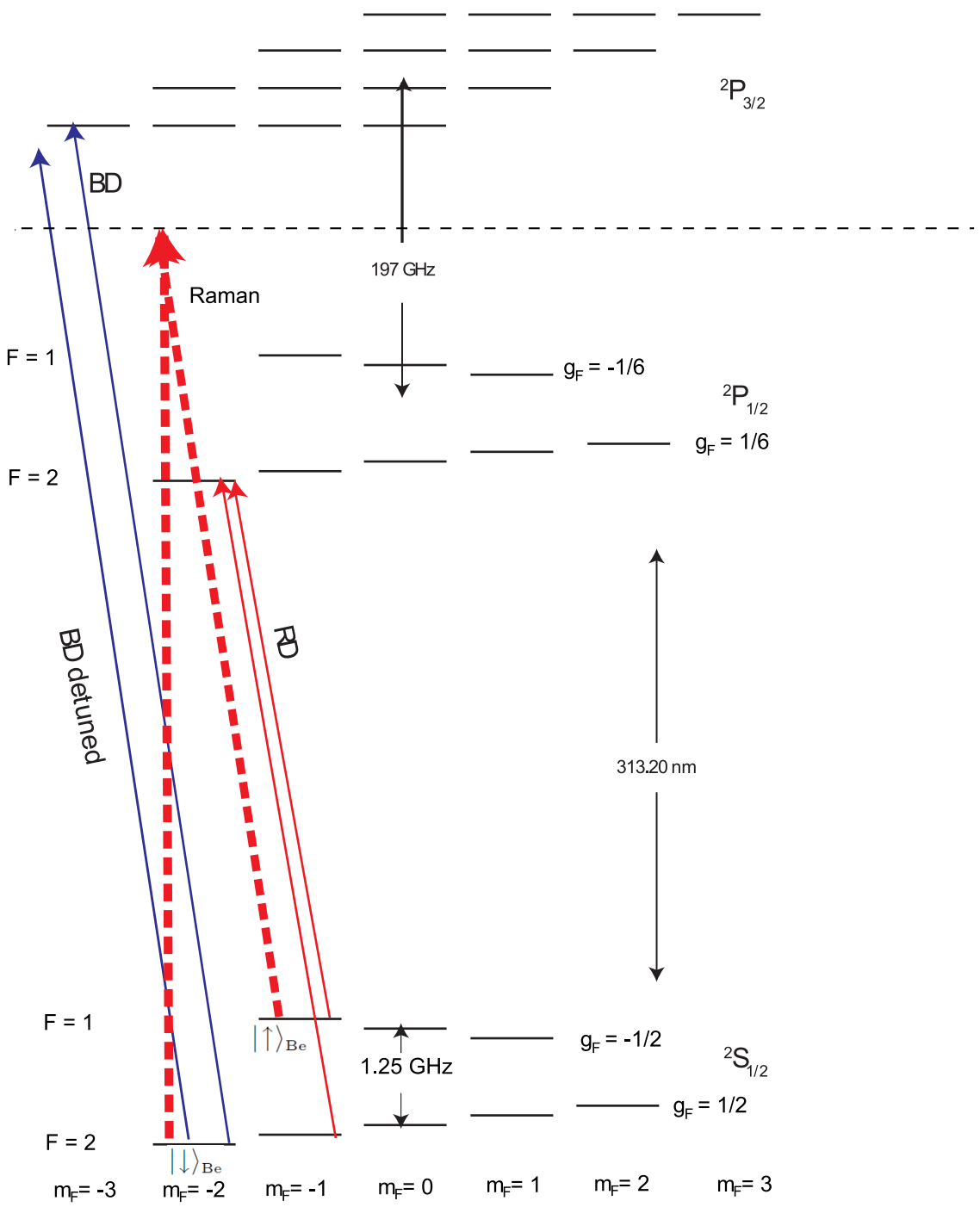

Figure 2.1: Relevant Be^+ levels and lasers.

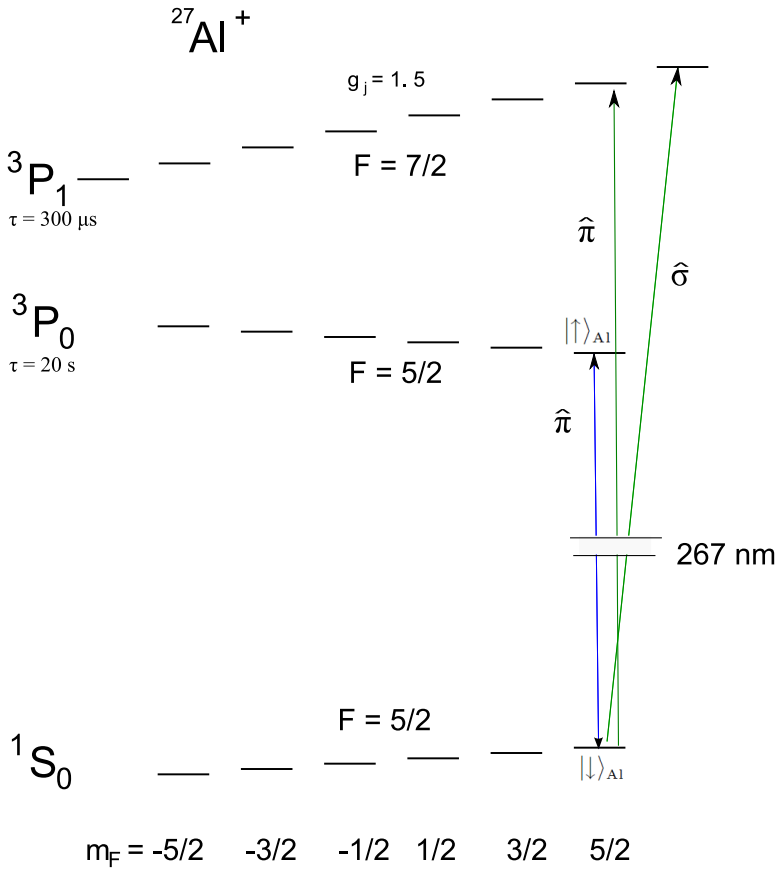

Figure 2.2: Relevant Al^+ levels and lasers.

s corresponding to a natural linewidth of 8 mHz, and has a measured frequency of 1121015393207857.4(7) Hz. Details of the Al^+ optical clock have been omitted from this dissertation to focus instead on the state detection techniques. For this, the relevant levels are sketched in Fig. 2.2. We generally use the $^1S_0$, $m_F = 5/2$ and $^3P_0$, $m_F = 5/2$ levels as a qubit. Both the ground state and $^3P_0$ energy levels, with angular momentum $J = 0$, exhibit only a weak dependence on the magnetic fields through the Zeeman effect. The g-factor for the $^1S_0$ arises primarily from the nuclear g-factor and has been measured as $g^1S_0) = -0.00079248(14)$. The g-factor for the $^3P_0$ arises from a combination of the nuclear g-factor and mixing with states have $J \neq 0$, and has been measured as $g^3P_0) = -0.00197686(21)$. The difference in the g-factors for these two manifolds is experimentally accessible and has been measured to be $g[^1S_0] - g[^3P_0] = 0.00118437(8)$ [Rosenband 07]. The $^3P_1$ state with $J = 1$ has $g_J \sim 1.5$.

The energy level diagrams also show the electronic transitions typically addressed by laser beams in

the experiments. These laser-ion interactions form the core of our experimental process.

2.2 Laser Ion Interactions

The evolution of a quantum mechanical system obeys the Schrödinger equation,

$$-i\hbar\frac{\partial\psi}{\partial t} = \hat{H}\psi, \tag{2.1}$$

where $\hat{H}$ is the total Hamiltonian for the system. Analytical solutions to Eq. 2.1 exist for a relatively small number of simple quantum systems. However, given $\hat{H}$, the quantum dynamics of the system can, in principle, be simulated numerically. The challenge in generating an accurate numerical model for an experimental system is in producing a Hamiltonian that incorporates all of the significant effects present. Conversely, it can be difficult experimentally to generate a physical system that approximates a relatively simple Hamiltonian. Fortunately, trapped ions do provide an experimental realization of an interesting, and relatively simple, quantum system. In this section I introduce the model we use to describe the behavior of trapped ions under the influence of applied fields. This will be a brief outline that closely follows previous treatments of the subject [Wineland 98], but I will point out particular details that relate to mixed-species ion arrays, and which may differ slightly from earlier work.

We model the behavior of a trapped ion as spin-1/2 particles coupled to a quantum harmonic oscillator. This model takes into account only a small subset of the internal and external degrees of freedom, and is justified only to the extent that we can insulate the system from other effects. A real ion moves in three dimensions, and contains many electronic eigenstates. The effects of these additional states in the system can often be ignored because they do not participate in the system dynamics. For example, since the motional sidebands are resolved, a pulse tuned to one resonance but we can laser cool all modes, and spectroscopically isolate one mode, so that the "spectator" modes have little effect on the system dynamics. The Hamiltonian for free evolution (without the application of external fields) of the system consists of terms representing the ion motion, $\hat{H}_m$, and the electronic states, $\hat{H}_e$, such that,

$$\hat{H}_0 = \hat{H}_m + \hat{H}_e. \tag{2.2}$$

For a single mode of motion,

$$\hat{H}_m = \hbar\omega_m(\hat{n}_m + \frac{1}{2}), \tag{2.3}$$

where $\omega_m/2\pi$ is the frequency and $\hat{n}_m$ is the number operator for mode m. To include more modes of motion, Eq. 2.3 would need to include a sum over the relevant degrees of freedom. Through optical pumping we can spectroscopically isolate a two-level subspace of electronic states, so that we treat the electronic degrees of freedom as to a spin-1/2 particle. In an N-ion array,

$$\hat{H}_e = \hbar\sum_{i=1}^{N}\omega_i\hat{S}_{z,i}, \tag{2.4}$$

where ω_i is the electronic resonance frequency for the ith ion and $S_{z,i}$ is the z-component of the fictional spin for the ith ion. Usually, we make the assumption that all ions of the same species have the same resonance frequency. In practice, this means that any perturbation to the frequency does not exhibit a significant gradient along the length of the ion array, which is the case in our experiments.

The Hilbert space of the system spans the eigenspace of $\hat{H}_0$, consisting of $N+1$ degrees of freedom (one for each ion and one for the motion). A particular eigenstate of the system is represented by, $|s_l\rangle = |M_z\rangle_1|M_z\rangle_2\ldots|M_z\rangle_N|n\rangle$, with $|M_z\rangle_i \in \{|\downarrow\rangle_i, |\uparrow\rangle_i\}$. To simplify notation, we can drop the ion subscripts and assume that the ion spin states appear in order (i.e. $|\downarrow\rangle_1|\downarrow\rangle_2 \rightarrow |\downarrow\downarrow\rangle$). A general pure state in the system can be written as

$$\sum_{l=1}^{2^N}\sum_{n=0}^{\infty} c_{l,n}|s_l\rangle|n\rangle \tag{2.5}$$

where each $|s_l\rangle$ is one of the set of 2^N spin states. In the interaction picture we consider how the state amplitudes in Eq. 2.5 evolve under the application of applied laser fields.

The electric field, $\mathbf{E}(\mathbf{x},t)$, of an applied laser beam interacts with the electronic state of an ion through the electric dipole operator, $\mu_{\mathbf{d}}$, producing the Hamiltonian,

$$\hat{H}_I = \sum_{i=1}^{N} -\mu_{\mathbf{d},\mathbf{i}}\cdot\mathbf{E}(\mathbf{x},t). \tag{2.6}$$

For a plane wave $\mathbf{E}(\mathbf{x},t) = E_0\cos(\mathbf{k}\cdot\mathbf{x}-\omega_L t+\phi_L)\hat{\xi}$, and we identify $\hbar\Omega_0 \equiv -\mu_d\cdot E_0\hat{\xi}$. We can rewrite Eq. 2.6 as

$$\hat{H}_I = \hbar\Omega_0\sum_{i=1}^{N}(S_{+,i}+S_{-,i})(e^{i(\mathbf{k}\cdot\mathbf{x}-\omega_L t+\phi)}+e^{-i(\mathbf{k}\cdot\mathbf{x}-\omega_L t+\phi)}), \tag{2.7}$$

where $S_{+,i}(S_{-,i})$ is the angular momentum addition (subtraction) operator for ion i. Switching to an interaction picture,

$$H_I' \equiv e^{iH_0 t/\hbar} H_I e^{-iH_0 t/\hbar}$$

$$H_I' = \hbar\Omega_0 \hat{S}_{+,i} \exp(i[\eta_i(\hat{a}e^{-i\omega_m t} + a^\dagger e^{i\omega_m t}) - \Delta t + \phi]) + h.c. \tag{2.8}$$

where $\eta_i \equiv \mathbf{k} \cdot \mathbf{x}_i$ is the Lamb-Dicke parameter for the ith ion, and $\hat{a}$ ($\hat{a^\dagger}$) is the raising (lowering) ladder operator for the relevant motional mode. To arrive at Eq. 2.8 we make the rotating wave approximation, so that terms oscillating at a frequency $\omega_0 + \omega_L$ are ignored. The evolution of the state amplitudes, $c_{l,n}$, is determined by the matrix elements $\langle s_{l'}|\langle n'|\hat{H}_I'|s_l\rangle|n\rangle$. In experiments we use laser pulses that are near-resonant either with the carrier transition at ω_0 or a motional sideband at $\omega_0 \pm (n' - n)\omega_m$. Thus, the only non-zero matrix elements are those for which a single ion undergoes a spinflip. Furthermore, in the resolved sideband regime we can safely take only the matrix elements where $|\omega_L - \omega_0| \approx |(n' - n)\omega_m|$. That is, we ignore the off-resonant coupling to other motional sidebands, which is justified because $\Omega_0/\omega_m \ll 1$. With these assumptions the coupling strength between two states can be written as [Wineland 98],

$$\Omega_i = \Omega_0 \exp[-\eta_i^2/2](n_<!/n_>!)^{1/2} \eta_i^{|n'-n|} L_{n_<}^{|n'-n|}(\eta_i^2). \tag{2.9}$$

This matrix element involves a spinflip on only the ith ion and connects the Fock state n to the state n', with $n_<$ and $n_>$ the lesser and greater of these respectively. The generalized Laguerre polynomial, $L_{n_<}^{|n'-n|}(\eta_i^2)$ has the ith ions Lamb-Dicke parameter, η_i, as its argument.

The discussion above applies to single photon transitions like those employed in interactions with Al^+. In the case of Be^+ we drive transitions between Zeeman sublevels in the ground state hyperfine manifolds using two-photon Raman transitions. In this case the $^2P_{1/2}$ and $^2P_{3/2}$ optically excited states act as intermediary states that are never populated to a significant degree. In general, if the Raman detuning, Δ_R, from the optically excited state is large compared to the on-resonance Rabi rate, Ω_0, this state can be "adiabatically eliminated" [Wineland 98], and we recover an interaction Hamiltonian that has the same form as Eq. 2.8. However Ω_0 is replaced with $\Omega_0' = \Omega_0^2/\Delta_R$, $\Delta = \omega_0 - (\omega_1 - \omega_2)$ and $\eta_i \equiv (\mathbf{k_1} - \mathbf{k_2}) \cdot \mathbf{x}_i$, where ω_1, ω_2, $\mathbf{k_1}$ and $\mathbf{k_2}$ are the frequencies and k-vectors of the the two Raman beams. From this we see that, in order to have reasonably fast Rabi rates for sideband transitions, the Raman beams must not be

copropagating. In most cases, for Be^+ Raman beams we choose $\mathbf{k_1} - \mathbf{k_2}$ to lie along the trap axis so that we address only axial modes of motion.

In our experiments we globally address all ions simultaneously with laser beams having a waist much larger than the interion spacing. If N ions of the same species are simultaneously addressed with a sideband pulse, there will, in general be N degenerate states that are simultaneously resonant, and the state evolution becomes a complicated process involving coupling with all of these levels. In this case there will not generally be analytical solutions for Schrödingers equation and we resort to numerical integration. However, in some cases, I have found the state evolution can be conceptually simplified by a basis transformation called the Morris Shore transformation.

2.3 Morris-Shore Transformation

The Morris Shore transformation [Morris 83] simplifies the evolution of a degenerate two-level system by factoring it into some number of independent two-level systems and isolated "dark" states. This would be the situation, for example, of resonantly driving the $F = 2$ to $F = 1$ hyperfine transition of $^9Be^+$, where $F = 2$ is five-fold degenerate and $F = 1$ is three-fold degenerate at $B = 0$ T. It applies to an arbitrary initial state with rf fields of arbitrary polarization. A conceptual schematic of this idea is given in Fig. 2.3. With certain conditions, the Morris-Shore transformation can be extended to the case of systems with a greater number of energy levels [Rangelov 06]. Both of these mathematical techniques apply to situations encountered in the ion trap experiments described here. Since I have found this technique useful I will review some relevant results and point out how they apply to ion experiments.

2.3.1 Two-Level Morris-Shore Transformation

Following the discussion in [Morris 83] and [Rangelov 06], we consider a quantum system Fig. 2.3 with two energy levels, E_a and E_b, with a number of degeneracies d_a and d_b respectively. The interaction Hamiltonian describing this system's evolution under the application of external fields may contain matrix elements connecting each of the states at E_a to each of the states at E_b, making a total of $d_a \times d_b$ linkages. However, we assume the off diagonal terms connecting states in the same energy level are zero. This situation

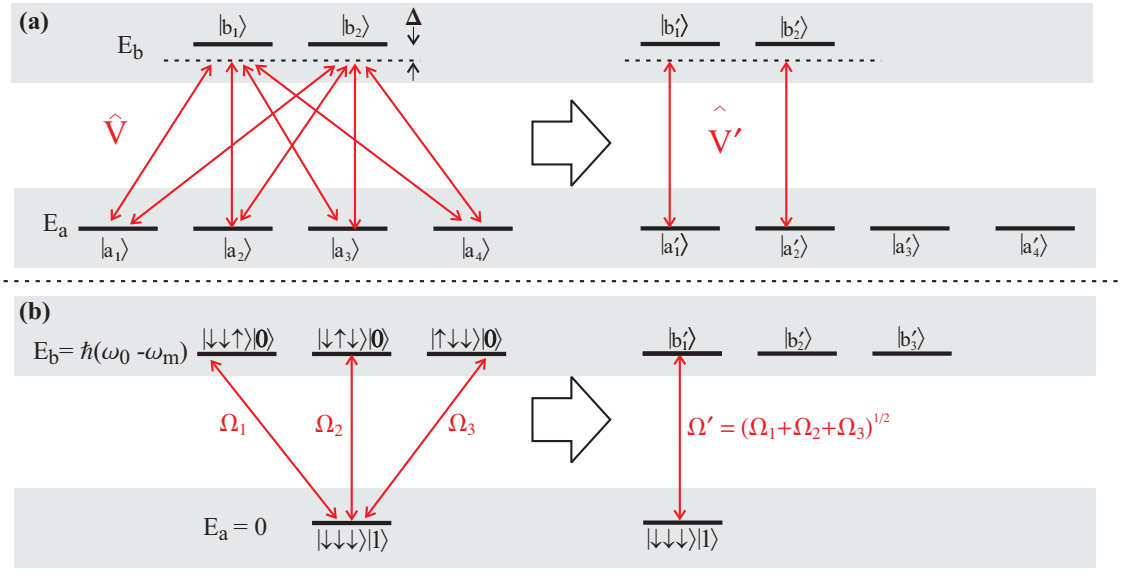

Figure 2.3: Conceptual diagram for the two-level Morris-Shore tranformation

can be represented by a Hamiltonian in the rotating-wave approximation of the form,

$$\hat{H} = \begin{bmatrix} \hat{0}_a & \hat{V} \\ \hat{V}^\dagger & \Delta \times \hat{I}_b \end{bmatrix}, \tag{2.10}$$

where $\hat{0}_a$ the null matrix in the subspace a (the result of choosing $E_a = 0$), $\hat{V}$ is a $d_a \times d_b$ rectangular matrix where V_{ij} is the coupling strength between state i and state j. The lower right block matrix is the identity matrix in the subspace b multiplied by the constant detuning Δ.

If $\vec{c}(t)$ is the state vector corresponding to the state of the system at some time, t, then the task at hand is to solve simultaneously the set of $d_a + d_b$ linear differential equations given by the Schrödinger equation,

$$i\frac{d}{dt}\vec{c}(t) = \hat{H}(t)\vec{c}(t). \tag{2.11}$$

We can apply a unitary transformation $\hat{U}$ to the basis states such that $\vec{c}' = \hat{U}\vec{c}$ and $\hat{A}' = \hat{U}\hat{A}\hat{U}^\dagger$, for any operator A acting on the system. This preserves the values of all observables since $\hat{U}^\dagger\hat{U} = \hat{I}$. The Morris-Shore unitary transformation mixes only the degenerate levels, so we consider unitary operators of the form

$$\hat{U} = \begin{bmatrix} \hat{U}_a & 0 \\ 0 & \hat{U}_b \end{bmatrix}. \tag{2.12}$$

The transformed Hamiltonian, $\hat{U}\hat{H}\hat{U}^\dagger$ has off-diagonal blocks $\hat{V}' \equiv \hat{U}_a\hat{V}\hat{U}_b$ and its Hermitian conjugate. To reduce this interaction to a basis with at most two-state couplings, we require that the rectanguluar matrix $\hat{V}'$ contain at most one non-zero element per row and per column. Notice that, under this condition, the square matrices $\hat{V}'\hat{V}'^\dagger = \hat{U}_a\hat{V}\hat{V}^\dagger\hat{U}_a^\dagger$ and $\hat{V}'^\dagger\hat{V}' = \hat{U}_b\hat{V}^\dagger\hat{V}\hat{U}_b^\dagger$ are both diagonal. This identifies the condition that U_a and U_b diagonalize $\hat{V}\hat{V}^\dagger$ and $\hat{V}^\dagger\hat{V}$ respectively as a necessary condition for the desired transformation. In [Morris 83] it is demonstrated that $\hat{V}\hat{V}^\dagger$ and $\hat{V}^\dagger\hat{V}$ have the same eigenvalues ignoring the $|d_a - d_b|$ null eigenvalues of the larger matrix, and that the previous condition on $\hat{U}_a$ and $\hat{U}_b$ always exists, providing the desired transformation.

The basis states after the transformation, expressed in terms of the original basis, for states at E_a and E_b are the eigenvectors of $\hat{V}\hat{V}^\dagger$ and $\hat{V}^\dagger\hat{V}$ respectively. If λ_i is a particular non-zero eigenvalue, those eigenvectors corresponding to λ_i form a two-state system with the effective Rabi rate $\sqrt{\lambda_i}$.

In Fig. 2.3 (b) we sketch one application of the Morris Shore transformation for state evolution in ion qubits, with qubit states denoted $|\downarrow\rangle$ and $|\uparrow\rangle$ respectively. We consider a string of three ions initialized in the electronic state $|\downarrow\rangle$ and prepared in the Fock State $|1\rangle$ for a particular mode of motion. A laser pulse tuned to resonance for the first red sideband of the qubit transition is applied to the ions, connecting the initial state to the three possible excited states, which are in the ground state of motion and have one qubit excitation. The coupling strength between the ground state and excited states, represented by Ω_i for ith ion, might be unequal due to imbalanced laser illumination or unequal motional amplitudes. These coupling strengths affect the eigenstates and the Rabi rates for the transformed system.

For zero detuning, the Hamiltonian matrix is

$$\hat{H} = \begin{bmatrix} 0 & \Omega_1 & \Omega_2 & \Omega_3 \\ \Omega_1 & 0 & 0 & 0 \\ \Omega_2 & 0 & 0 & 0 \\ \Omega_3 & 0 & 0 & 0 \end{bmatrix}, \tag{2.13}$$

so that

$$\hat{V} = \begin{bmatrix} \Omega_1 & \Omega_2 & \Omega_3 \end{bmatrix}. \tag{2.14}$$

Since there is only one state in the ground-state manifold there will be only one non-zero eigenvalue of $\hat{V}^\dagger \hat{V}$, given by $\Omega'^2 = \Omega_1^2 + \Omega_2^2 + \Omega_3^2$. This eigenvalue corresponds to the normalized eigenvector

$$|b_1'\rangle = (\Omega_1^2 + \Omega_2^2 + \Omega_3^2)^{-1/2} \begin{bmatrix} \Omega_1 \\ \Omega_2 \\ \Omega_3 \end{bmatrix} \tag{2.15}$$

The factorization also identifies the "dark" states of the system (state vectors that do not evolve under application of $\hat{H}$) as vectors in the null space of $\hat{V}^\dagger \hat{V}$. In the present example the state $(\eta_1^2+\eta_2^2)^{-1/2}(-\Omega_2|\uparrow\downarrow\downarrow\rangle + \Omega_1|\downarrow\uparrow\downarrow\rangle)$ corresponds to a zero eigenvalue.

The result above can be generalized to an arbitrary number of ion qubits undergoing red sideband excitation from the Fock state $|1\rangle$. The Rabi rate for the transformed system is given by

$$\Omega'^2 = \sum_{i=1}^{N} \Omega_i^2 \tag{2.16}$$

and the excited state can be written as

$$|b_1'\rangle = \frac{1}{\Omega'}\Big(\Omega_1|\uparrow\downarrow\ldots\downarrow\rangle + \Omega_2|\downarrow\uparrow\ldots\downarrow\rangle + \ldots + \Omega_N|\downarrow\downarrow\ldots\uparrow\rangle\Big). \tag{2.17}$$

This transformation is applied to the simulations of some experiments in Sec. 6 as well as Sec. 5.2.3.

2.3.2 Multilevel Morris-Shore Transformation

This convenient basis change has also been applied to systems with more than two degenerate manifolds [Rangelov 06]. If the system has N_E energy levels, each level will have some degree of degeneracy, d_j with $j \in [1, N_E]$. The total number of states is $\sum_j d_j$, but we consider, as before, a Hamiltonian, $\hat{H}$ that only connects states in adjacent energy levels. The maximum number of linkages in the Hamiltonian for the system is then $\sum_{j<N_E} d_j d_{j+1}$. The desired change of basis transforms the system into a set of isolated systems with, at most, N_E levels each. This can significantly simplify the evolution of the system because now the number of non-zero off-diagonal matrix elements $\hat{H}$ is $\sum_{j<N_E} d_{j,\min}$ where $d_{j,\min}$ is the lesser of d_j and d_{j+1}.

The Hamiltonian for a degenerate N_E-level system can be expressed in block-matrix form as

$$\hat{H} = \begin{bmatrix} \hat{0} & \hat{V}_1 & \hat{0} & \cdots \\ \hat{V}_1^\dagger & \Delta_2 & \hat{V}_2 & \\ \hat{0} & \hat{V}_2^\dagger & \Delta_3 & \\ \vdots & & & \ddots \end{bmatrix}, \tag{2.18}$$

where each matrix $\hat{0}$ is the null matrix with the appropriate dimensionality $d_j \times d_{j'}$, the matrix $\hat{V}_j$ contains all the elements connecting states in system j to system $j+1$, and $\hat{\Delta}_j$ is the scalar detuning of the applied fields from the state j multiplied by the identity. In analogy to the two-level transformation described above, this Hamiltonian can be transformed by a block-diagonal unitary matrix of the form

$$\hat{U} = \begin{bmatrix} \hat{U}_1 & \hat{0} & \hat{0} & \cdots \\ \hat{0} & \hat{U}_2 & \hat{0} & \\ \hat{0} & \hat{0} & \hat{U}_3 & \\ \vdots & & & \ddots \end{bmatrix}. \tag{2.19}$$

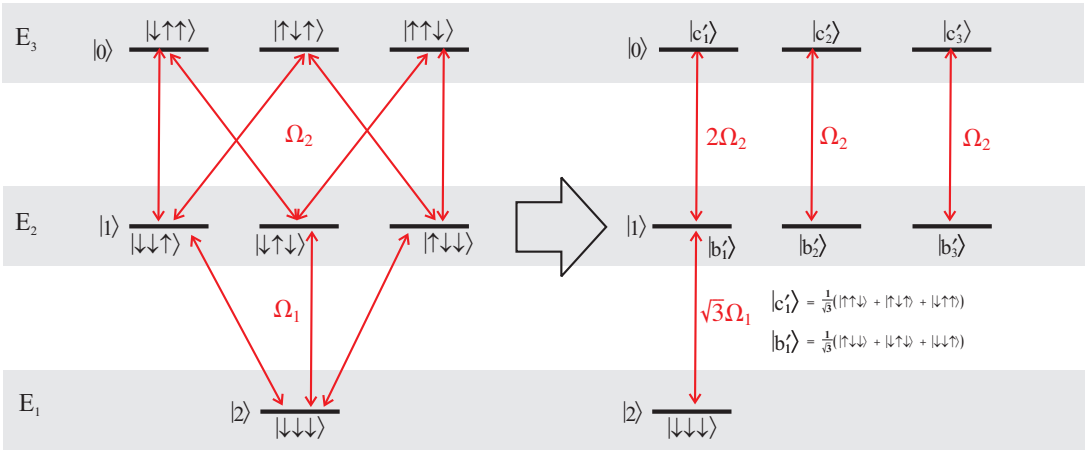

Figure 2.4: Conceptual diagram for a multilevel Morris-Shore transformation

The transformed Hamiltonian,

$$\hat{H}' = \hat{U}\hat{H}\hat{U}^\dagger = \begin{bmatrix} \hat{0} & \hat{U}_1\hat{V}_1\hat{U}_2^\dagger & \hat{0} & \cdots \\ \hat{U}_2\hat{V}_1^\dagger\hat{U}_1^\dagger & \Delta_1 \times \hat{I} & \hat{U}_2\hat{V}_2\hat{U}_3^\dagger & \\ \hat{0} & \hat{U}_3\hat{V}_2^\dagger\hat{U}_2^\dagger & \Delta_2 \times \hat{I} & \\ \vdots & & & \ddots \end{bmatrix}, \tag{2.20}$$

has upper off-diagonal blocks $\hat{V}_j' = \hat{U}_j\hat{V}_j\hat{U}_{j+1}^\dagger$ representing the interactions in the transformed Hamiltonian, which must be diagonal after removing null rows and columns. As a consequence, the matrices $\hat{V}_j'\hat{V}_j'^\dagger = \hat{U}_j\hat{V}_j\hat{V}_j^\dagger\hat{U}_j^\dagger$ and $\hat{V}_j'^\dagger\hat{V}_j' = \hat{U}_{j+1}\hat{V}_j^\dagger\hat{V}_j\hat{U}_{j+1}^\dagger$ must be diagonal. If all $\hat{V}_j'\hat{V}_j'^\dagger$ are to be diagonal under the transformation $\hat{U}$, then U_{j+1} must simultaneously diagonalize $\hat{V}_j^\dagger\hat{V}_j$ and $\hat{V}_{j+1}\hat{V}_{j+1}^\dagger$ for $j \in [1\, N_E - 1]$. Thus, we arrive at the stringent constraint that

$$[\hat{V}_j^\dagger\hat{V}_j, \hat{V}_{j+1}\hat{V}_{j+1}^\dagger] = 0, \tag{2.21}$$

where brackets indicate the commutator. If this condition is satisfied, any eigenstate $|\psi_j^{(\mu)}\rangle$, is connected via $\hat{H}'$ to at most two other eigenstates $|\psi_{j-1}^{(\mu)}\rangle$ and $|\psi_{j-1}^{(\mu)}\rangle$ where we have identified the eigenvectors in any two adjacent energies with respect to a common eigenvalue $\lambda_j^{(\mu)}$. The eigenvalues are, again, the square of the coupling strength between the two levels.

Following the example of Fig. 2.3 (b) we present a concrete example of the application of the generalized Morris-Shore transformation applied to trapped ions. Similar calculations have been used in Sec. 6 in

analyzing the state evolution of multiple ions under global sideband pulses. The energy levels and couplings are sketched in Fig. 2.4. As in the previous example, we consider three ions each prepared in the state $|\downarrow\rangle$ and addressed by a red sideband laser pulse. This time they begin in the motional Fock state $|2\rangle_M$.

There are three energy levels to consider. The ground state of the system is non-degenerate and the red sideband interaction connects to all three states at energy E_2 in the untransformed basis. Likewise each of these states connects to two states at energy E_3, making six total non-zero matrix elements between the upper two energy levels. The off-diagonal blocks in the Hamiltonian can be written as

$$V_1 = \begin{bmatrix} i\Omega_1 & i\Omega_1 & i\Omega_1 \end{bmatrix} \tag{2.22}$$

$$V_2 = \begin{bmatrix} i\Omega_2 & i\Omega_2 & 0 \\ i\Omega_2 & 0 & i\Omega_2 \\ 0 & i\Omega_2 & i\Omega_2 \end{bmatrix}. \tag{2.23}$$

We can confirm that $\left[\hat{V}_1^\dagger \hat{V}_1, \hat{V}_2 \hat{V}_2^\dagger\right] = 0$. Note that we have assumed equal motional amplitudes and equal illumination for all ions, which is necessary for satisfying the condition of Eq. 2.21. In the Lamb-Dicke limit, the only other conditions under which Eq. 2.21 holds is the trivial case of with zero motional amplitude for two of the ions, however, outside of the Lamb Dicke limit other non-trivial solutions to Eq. 2.21 may exist.

The product $\hat{V}_1 \hat{V}_1^\dagger$ is a scalar since the ground state is non-degenerate, and the coupling strength for connecting the ground state to the next level is given by $\sqrt{\hat{V}_1 \hat{V}_1^\dagger} = \sqrt{3}\Omega_1$. The complementary product, $\hat{V}_1^\dagger \hat{V}_1$, is a 3×3 matrix with a single non-null eigenvector corresponding to the entangled state $|b_1'\rangle = 1/\sqrt{3}(|\downarrow\downarrow\uparrow\rangle + |\downarrow\uparrow\downarrow\rangle + |\uparrow\downarrow\downarrow\rangle)|1\rangle_M$ (see Sec. 6), which connects to $|\downarrow\downarrow\downarrow\rangle|2\rangle_M$. The evaluation of eigenvectors and eigenvalues for the matrices, $\hat{V}_2^\dagger \hat{V}_2$, $\hat{V}_2 \hat{V}_2^\dagger$ gives the states involved in coupling levels E_2 and E_3 and their respective strengths. Since Eq. 2.21 is satisfied, we know $|b_1'\rangle$ is an eigenvector also of $\hat{V}_2 \hat{V}_2^\dagger$. It has eigenvalue $4\Omega_2^2$ and connects to the state $|c_1'\rangle = 1/\sqrt{3}(|\uparrow\uparrow\downarrow\rangle + |\uparrow\downarrow\uparrow\rangle + |\downarrow\uparrow\uparrow\rangle)|0\rangle_M$ in the manifold of E_3. There are two other eigenvectors and eigenvalues for both of the matrices $\hat{V}_2^\dagger \hat{V}_2$ and $\hat{V}_2 \hat{V}_2^\dagger$, and each of the sets defines an isolated two-level system under the red sideband interaction.

In this section we have reviewed the mathematical formalism behind a useful basis change called the Morris-Shore transformation. In certain trapped ion experiments this allows us to express complicated state

dynamics in terms of the evolution of isolated systems each with a small number of equally spaced states. In particular, when considering sideband pulses globally addressing multiple ions, as in the experiments of Ch. 6 and Ch. 5 this transformation represents a conceptual and numerical simplification.

Chapter 3

Apparatus

3.1 Ion Trap

3.1.1 Ion Trap Theory

In this section I review some of the basic features of ion traps and point out how some results relate to practical experimental considerations. The fundamental property of an ion that gives us an experimental handle for controlling its external degrees of freedom is its charge. The Lorentz force law relates the force on a particle from local electric and magnetic fields, $\mathbf{E}$ and $\mathbf{B}$ respectively, to a particle's charge, Q and velocity $\mathbf{v}$ by

$$\mathbf{F} = Q(\mathbf{E} + \mathbf{v} \times \mathbf{B}). \tag{3.1}$$

These fields provide an experimenter with the means to influence the motion of any charged particle. The goal may be to accelerate a proton to near the speed of light, or to hold an atomic ion nearly motionless as in the experiments of this thesis.

Various configurations of electric and magnetic fields have been devised to trap ions. Many aspects of these methods have been compiled in recent books on the subject [Ghosh 95, Major 05], which are good overviews of the science and history of ion trapping and are useful references toward primary sources. Two major categories of ion traps are the Penning trap and the Paul trap. The Penning trap combines a strong magnetic field with electric fields to provide three-dimensional harmonic confinement. The Paul traps discussed here use time-varying electric fields (sometimes in combination with static electric fields) to achieve the same goal.

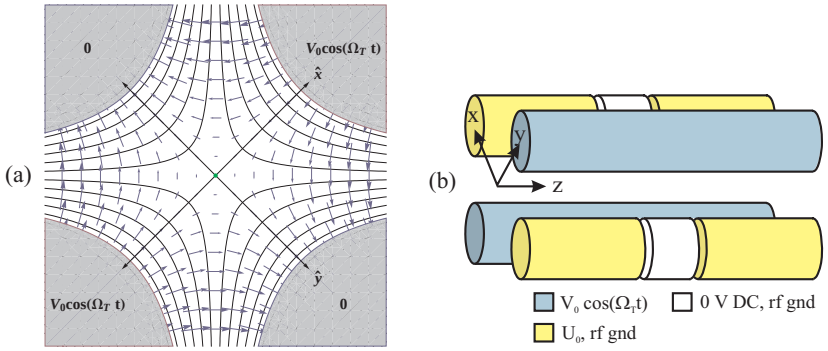

Figure 3.1: (a) A cross section of the ideal linear Paul trap. Radio frequency voltages applied to the electrodes (gray corner regions) set up an oscillating quadrupolar potential (contour lines). The electric field (arrows) ideally vanishes at the trap center. Any displacement of the ion (green circle) from the trap center leads to driven motion (micromotion) perpendicular to the direction of displacement at the frequency Ω_T. (b) A model for a simple linear Paul trap. In addition to the radial confinement provided by rf fields, a static potential U_0 applied to the endcaps (yellow) provides axial confinement. The center electrodes (white) are held at DC ground.

For a particle of mass m and charge Q confined harmonically in three dimensions, the external potential energy can be described generally by

$$Q\Phi = \frac{1}{2}\sum_{i=1}^{3} k_i u_i^2, \tag{3.2}$$

where $i \in \{x, y, z\}$ and k_i is the oscillator spring constant in coordinate u_i. The Laplace equation, $\nabla^2\Phi = 0$ provides the constraint

$$\sum_i k_i = 0, \tag{3.3}$$

such that either $k_i = 0$ for all i (the trivial case of a free particle) or $k_i < 0$ for some i. Since a negative spring constant is anticonfining this means that no configuration of static electric fields can be used to harmonically trap charged particles - one case of a general result called Earnshaw's theorem. However, Earnshaw's theorem does not preclude the use of time-varying electric fields to confine ions.

The linear Paul traps in this thesis use RF electric fields to constrain a chain of positively charged atomic ions to one axis, and DC electric fields to provide stable confinement in the third dimension. The development of this hybrid rf-DC trap was preceded by the development of spherical Paul traps that used RF fields for confinement in all three dimensions [Schuessler 69, Motz 67]. In either case a single ion is pushed toward a null in the RF electric fields by their time averaged effects (called the ponderomotive force) [Motz 67]. If there are multiple ions in a trap they will experience mutual repulsion according to Coulomb's

law. In the case of a spherical Paul trap they will tend to displace each other from the null of the RF field, and will experience driven motion. This RF ion motion can cause several deleterious effects in the context of precision spectroscopy and quantum information processing [Berkeland 98]. The development of the linear Paul trap was motivated by the idea of reducing these effects while trapping multiple ions in a single trap [Prestage 89, Raizen 92]. The linear Paul trap sets up a nodal line, along which the RF electric fields vanish, constraining the ions to one dimension through the ponderomotive force then "capping" the ends of the nodal line with DC fields.

The ideal linear Paul trap consists of four parallel, rod-like electrodes. I follow the convention that the rods extend in the z direction, which defines the axis of the ion chain to be at the trap centroid in the x-y plane. I define the x direction to connect two diagonally opposing electrodes (x electrodes) and the y direction to connect the remaining two electrodes (y electrodes). With these definitions, a radio frequency voltage $V_0 cos(\Omega_T t)$ applied to the x electrodes, while the y electrodes are held at ground, sets up an oscillating quadrupolar potential given by

$$\Phi_{rf} = \frac{V_0 cos(\Omega_T t)}{2}\left(1 + \frac{x^2 - y^2}{R^2}\right), \tag{3.4}$$

where R denotes the shortest distance from the trap axis to an electrode. A snapshot in time of such a potential is depicted in Fig. 3.1(a). The contour lines represent equipotentials and define the borders of the four electrodes (gray corner regions). Any deviation from the hyperbolic electrode border will lead to higher-order terms in Φ_{rf}, as well as a weakening of the quadrupolar potential. For a radial ion position, $r = \sqrt{x^2 + y^2} \ll R$ these effects are small and can be taken into account by multiplying Eq. 3.4 by a factor on the order of unity [Wineland 98]. The arrows in Fig. 3.1(a) show the relative magnitude and direction of the electric field

$$\mathbf{E}_{rf} = -\nabla\Phi_{rf} = \frac{V_0 cos(\Omega_T t)}{R^2}\left(-x\hat{x} + y\hat{y}\right), \tag{3.5}$$

at a particular RF phase. This oscillating field vanishes at the trap axis. As the ion is displaced radially from the center of the trap it gains kinetic energy due to its driven motion at frequency Ω_T, which is in a direction perpendicular to the direction of displacement. This geometry becomes important when considering the measurement and compensation of excess micromotion.

I sketch a model for the three dimensional geometry of a linear Paul trap in Fig. 3.1(b). Two diagonally opposing cylindrical electrodes carry RF potential, while the remaining two segmented electrodes are kept at RF ground. We apply a DC voltage U_0 to the outer segments of these electrodes (called endcaps) to provide confinement of the ions in the axial direction. To second order this produces a harmonic trapping potential in the z direction and an "antitrapping" potential in the radial direction that is given by

$$Q\Phi_s = \frac{1}{2}k_z\Big(z^2 - \big[\epsilon x^2 + (1-\epsilon)y^2\big]\Big), \tag{3.6}$$

where $k_z \equiv 2\kappa U_0 Q$ is the axial spring constant for an ion of charge Q, and both κ and ϵ are geometrical factors. For the harmonic approximation in Eq. 3.6 to be valid we must have $\kappa u^2 << 1$ for $u = x, y, z$.

Consider a single ion of mass m and charge q trapped in a potential given by $\Phi = \Phi_s + \Phi_{rf}$. In the axial direction, only DC terms appear in the potential energy $V = -Q\Phi$. Treating the problem classically, the equation of motion

$$\ddot{z} = -\frac{k_z}{m}z, \tag{3.7}$$

is the equation for a simple harmonic oscillator, which is solved by

$$z = Re[z_0 e^{i(\omega_z t + \phi_z)}], \tag{3.8}$$

where $\omega_z = \sqrt{\frac{k_z}{m}}$. The amplitude, z_0, and phase ϕ_z are given by initial conditions.

In the radial directions, the equations of motion involve contributions from the DC potential (Eq. 3.6) and the oscillating RF potential (Eq. 3.4). They can be cast into a form identical to the canonical Mathieu equation [McLachlan 47],

$$\frac{d^2u_i}{d\zeta_i} = [a + 2q_i cos\,(2\zeta)]u_i = 0, \tag{3.9}$$

with $a = -4Q\kappa U_0/m\Omega_T^2 = -2k_z/m\Omega_T^2$ (for the symmetric case with $\epsilon = \frac{1}{2}$) and $q_x = -q_y = 2QV_0/\Omega_T m R^2$. The solution to this equation to lowest order in q_i is

$$u_i(t) = A_i cos(\omega_i t + \phi_i)[1 + \frac{q_i}{2}cos(\Omega_T t)], \tag{3.10}$$

where A_i and ϕ_i are determined by initial conditions. In the preceding analysis we have assumed the trap strength is equal in the x and y coordinates and aside from the RF phase in Eq. 3.10 the solutions for $i = x, y$ are the same. In the following discussion we use $i = r$ to refer to either coordinate.

The motion at frequency

$$\omega_r = (a + q_r^2/2)^{1/2}\Omega_T/2 \tag{3.11}$$

is called secular motion and is the higher amplitude motion in the experiments discussed here since $a \ll q_r \ll 1$. We refer to the driven motion at frequency Ω_T as micromotion. This motion is important because, in the frame of the ion, it can divert optical power of an applied laser pulse into micromotion sidebands, depleting the carrier, and potentially affecting the efficiency of laser cooling. Typically in our experiments the ions are cooled to low temperatures ($\sim$ 0.1 mK) so the motional amplitude, $A_i q_i$, is small and these effects of micromotion are negligible. In the case of ion frequency standards, where the relativistic time-dilation shift of $\delta\nu/\nu = \langle v^2\rangle/2c^2$ may cause appreciable shifts at relatively low velocities ($\langle v^2\rangle = 1$ m^2/s^2), micromotion amplitudes at these low temperatures cannot be ignored.

Considering only the secular motion (that is averaging over the micromotion), the ion behaves as if it is confined in a harmonic potential well in the radial direction. The spring constant for this harmonic oscillator is given by $k_r = m\omega_r^2 = 4Q^2V_0^2/mR^4 - k_z/2$. The first term arises from the radial RF fields, while the second term accounts for the antitrapping effect of the axial trapping fields. If we write

$$a_r \equiv 4Q^2V_0^2/mR^4, \tag{3.12}$$

then we can define an effective pseudopotential, Φ_P as

$$Q\Phi_P = \frac{1}{2}a_r r^2/m. \tag{3.13}$$

This identifies the radial secular motion as harmonic motion and is called the pseudopotential approximation.

Note that the harmonic pseudopotential is different from the axial harmonic potential in that it is inversely proportional to the ion mass. Thus, heavier ions are bound less tightly to the axis of the trap. The solution to the Mathieu equation given in Eq. 3.10 is valid only for $a_i \ll q_i \ll 1$. In the case that q_i approaches one, $\Omega_T \simeq \omega_i$ and the ion motion can become unstable. This is the key feature that enables the use of radiofrequency electric fields for mass spec applications. Since $\omega_x \propto 1/m$ lighter mass ions have a larger q-parameter, and enter the region of instability at lower V_0.

In setting up the single ion experiments discussed in this thesis, we sometimes accidentally load unwanted ions of different mass from the experimental ions. If V_O can be raised to a sufficient level we

can, in principle, selectively eject unwanted lighter-mass ions. This can be difficult in practice because, in designing the ion traps, we prefer radial confinement as high as possible to maintain linear crystals ($\omega_r \gg \omega_z$) while being able to resolve the motional sideband spectrum. Without being able to significantly raise V_0 or lower Ω_T we cannot significantly affect trap stability in this way. For unwanted heavier-mass ions, however, we can use a different technique. By raising U_0 (or equivalently lowering V_0) we decrease $k_i = a_r/m - k_z/2$. A heavier mass ion will reach an unstable condition where $k_i = 0$ at lower U_0 (or higher V_0), and will be ejected from the trap. We have found this technique to be reliable for eliminating ions with mass ratios as low as $\mu = 1.11$ (i.e. separating BeH^+ from Be+).

3.1.2 Experimental Trap

One of the major design goals for the ion traps used in our experiments is a high radial confinement frequency. This allows for a well-resolved motional mode spectrum while maintaining fast sideband pulses. With the constraint that $\omega_r > \omega_z$ for linear chains of ions, the scale of the trapping frequencies is set by the radial confinement strength. Maximizing this amounts to maximizing the parameter a_r of Eq. 3.12, which scales as $1/R^4$ ($\omega_r \propto 1/R^2$), so, for high confinement frequencies, we desire a small electrode-ion distance. However, practical considerations such as machining tolerances often limit how small trap features can be made. In addition, experiments on individual ions often suffer from anomalous heating of the ion secular motion [Turchette 00, Wineland 98]. This can reduce the fidelity of quantum protocols and cause time-dilation shifts in ion-based atomic clocks [Rosenband 08]. Although the exact mechanism for this heating is an active question [Dubessy 09], controlled observations [Deslauriers 06] of the heating rate for a particular mode show that $\dot{\bar{n}} \propto R^p$ where $p \sim 4$.

In the experiments described in this thesis, we used two different experimental systems. Most of the work was done in a system designed for experiments on Be^+ and Al^+, while the experiments in the final chapter involve a separate system designed for Mg^+ and Al^+. Aside from the two laser systems that interact with Al^+, the experiments, including the linear Paul traps are completely separate. To compare the relevant parameters of these two traps, we sketch a general picture of the electrodes surrounding the trap region in Fig. 3.2(a), and tabulate values for the two traps in Fig. 3.2(b). The radial confinement frequency is also

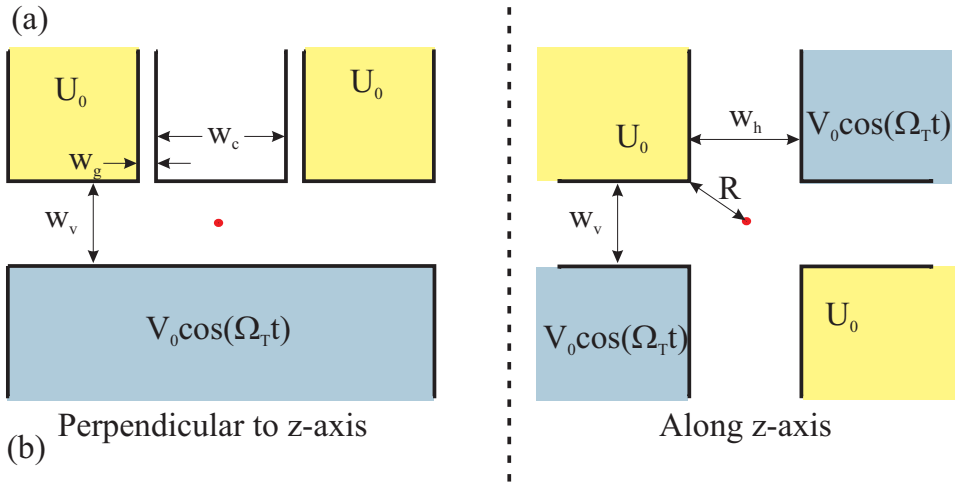

Trap	w_v [μ m]	w_h [μ m]	w_g [μ m]	w_c [μ m]	R [μ m]	V_0 [V]	Ω_T [MHz]	U_0 [V]
Wafer	200	450	20	200	250	$\sim$ 400	103	12
Knifeblade	600	600	200	1600	425	1000	59	100

Figure 3.2: (a) Diagram of a generic trap structure showing the relevant physical dimensions. These measurements, together with the applied electric fields, and geometrical factors on the order of unity, determine the trap frequencies. (b) The dimensions for the two traps with the Be-Al trap labeled "wafer" and the Mg-Al trap labeled "knifeblade".

proportional to the applied RF voltage, V_0. To obtain higher ω_r we mount the ion trap at the end of a coaxial, quarter-wave RF resonator and typically obtain a quality factor on the order of 200. Coupling 5-20 W of RF power into the resonator achieves the voltages tabulated in Fig. 3.2(b).

A picture of the wafer trap used in Ch. 5 is shown in Fig. 3.3(a). This trap was originally used in a sympathetic cooling experiment [Barrett 03], then adapted for work on quantum logic spectroscopy [Schmidt 05] with $^9Be^+$ and $^{27}Al^+$. With a single $^9Be^+$ ion we generally work with conditions such that $\{\omega_x, \omega_y, \omega_z\} \simeq \{14, 13, 4\}$ MHz. The design is based on a gold coated, laser-machined, alumina substrate to define both the RF and DC electrodes [Rowe 02]. Two identical wafers (one flipped relative to the other by 180 degrees about the long axis) separated by an insulating spacer produce a close approximation to the model of a linear Paul trap in Fig. 3.1(b). In addition, the machining tolerances for the microfabricated electrode structures can be very low, leading to well characterized trap conditions.

The second trap was designed specifically for the Al^+ optical clock, where factors limiting the clock accuracy, such as micromotion compensation and ion heating rate, are a more severe limitation. Thus the

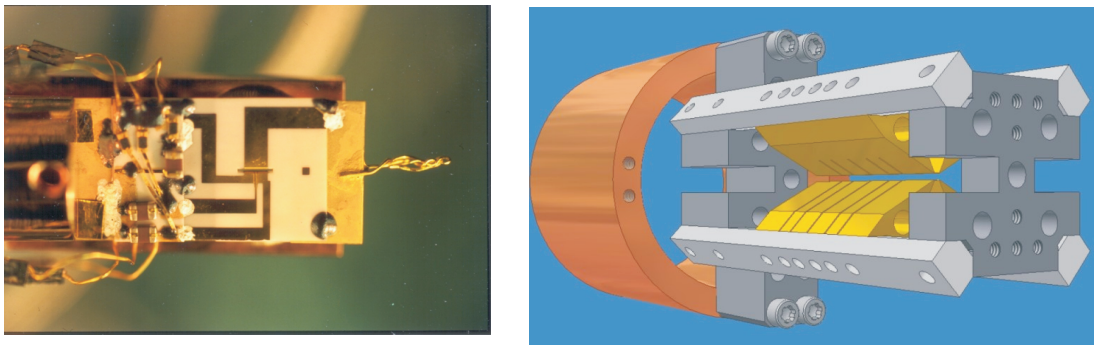

Figure 3.3: (a) A photograph of the gold-plated alumina wafer trap. (b) A drawing of the knife-blade style trap used in the experiments of Ch. 6 with the end of a copper RF resonator also shown.

trap is larger and constructed from solid metal electrodes with the nearest insulating surface relatively far from the ion, reducing the effects of stray charges. This trap was used in the experiments of Ch. 6 where we use $^{25}Mg^{+}$ as a sympathetic cooling and quantum logic ion. For a single $^{25}Mg^{+}$ ion and the parameters in the table of Fig. 3.2(b), we obtain frequencies of $\{\omega_x, \omega_y, \omega_z\} \simeq \{6.7, 4.9, 3.0\}$ MHz. In this case, the difference in the x and y mode frequencies comes primarily from applying DC voltages to both center electrodes.

Each ion trap is mounted in an ultrahigh vacuum system at the end of a quarter-wave coaxial resonator. The basic features of both vacuum systems are the same. The traps are surrounded by a cylindrical glass envelope featuring several flat windows that allow optical access for both the laser beams and an ∼F/1 imaging system. This glass envelope connects to a stainless steel vacuum chamber via a glass-metal seal. The vacuum chamber consists of several arms that house an ion pump, a titanium sublimation pump and an ion gauge for monitoring pressure. We baked out the assembled systems at a temperature near 200 C [1] while pumping on it with a turbopump, which was later disconnected. The final pressure we achieve for both systems is near 1×10^{-11} Torr. The quarter wave resonator is partly inside and partly outside the vacuum chamber, with the inner conductor transmitted through a vacuum feed-through. The RF trap drive is coupled using an antenna into the resonator mode and the coupling is optimized by monitoring the reflected power through a directional coupler. The RF power incident on the resonator can be switched between two levels using a TTL switch and an attenuator. In order to maintain ions in the trap while switching between these two arms of the circuit we found it was necessary to adjust the cable lengths properly so that the RF

[1] The exact value differed between the two systems due to different temperature sensitivity of the components.

phase was matched at the resonator. The voltages applied to the endcap electrodes and the separate bias electrodes are fed into the vacuum system via a feed through and filtered using RC filters both internal and external to the vacuum chamber providing corner frequencies near 10 kHz.

3.2 Laser Systems

The lasers required for interacting with our ions are all at frequencies in the ultraviolet spectral range. The laser sources involve frequency stabilized visible or infrared lasers that are then frequency doubled or quadrupled using nonlinear optical crystals in a buildup cavity. I briefly describe the laser systems used to interact with Be^+, Al^+ and Mg^+ separately here.

3.2.1 Be^+ lasers

To interact with the Be^+ atomic system, we require lasers at 313 nm. We derive these beams from three separate frequency-doubled dye lasers at 626 nm. For convenience, we call the laser systems: 1) Blue Doppler (BD), which is used for Doppler cooling and state detection, 2) Red Doppler (RD), which is used for repumping and state preparation, and 3) Raman, which is used for driving stimulated Raman transitions between the qubit levels. All of these laser systems are home-built, verdi-pumped, ring dye lasers in a bowtie configuration. The basic design was developed in house over several years [Bergquist 10], and I will give only a brief overview of the system here.

A thin jet of Rhodamine dye (dissolved in ethylene glycol) passes through the strong focus of the laser cavity with the liquid-air interfaces oriented at Brewster's angle with respect to the cavity mode. The 532 nm Verdi laser at a power between 2 W and 6 W is focused onto a point in the dye stream that is coincident with the focus of the cavity mode. Although the emission spectrum of the Rhodamine dye is many tens of nanometers wide, several intracavity elements limit the laser gain to a narrower frequency region around 626 nm. From coarsest to finest they are: 1) a birefringent filter, for which the angle is adjusted with a micrometer screw, 2) a current controlled etalon (thin etalon), and 3) a piezo-mounted etalon (thick etalon). The thick etalon is actively stabilized with a slow servo loop to the maximum laser output using a lock-in amplifier. One mirror of the bowtie cavity is mounted on a piezoelectric transducer. This provides a means

to stabilize the overall cavity length to an external reference cavity (finesse approximately 300). To lock to the reference cavity, we use a Hansch-Couillaud (H.-C.) [Hansch 80] locking scheme based on the phase shift between beams transmitted and reflected from the reference cavity. The difference signal from 2 photo diodes is amplified and fed back to the dye laser cavity piezo. The combination of these frequency selective elements produces a laser linewidth of approximately 100 kHz, which is sufficient for precisely interrogating the ∼20 MHz optical resonance in Be^+. In addition, we lock the laser to a molecular absorption feature in I2 by performing saturated absorption spectroscopy in a gas cell [Preston 96]. Here, two weak laser beams (probe beam and reference beam) traverse the length of the I^2 cell. The probe beam is overlapped using a polarizing beam splitter (PBS) with a strong, counter-propagating saturation beam. The transmitted probe and reference beams are focused onto an autobalancing difference detector. The electronic signal from the difference detector is demodulated and amplified to feed back on a ring piezo in the reference cavity. This feedback loop stabilizes the reference cavity, and in turn the dye laser, to the molecular iodine signal.

Depending on the Verdi pump power, these dye lasers produce between a few hundred mWs and 1 W of laser power at 626 nm. The bulk of this light is coupled into an optical fiber and transmitted to a separate laser table. Here, the visible light is frequency doubled in a build up cavity. The design of the frequency doubling cavity is nearly the same for all three Be^+ laser systems. A type-II, critically phase matched, Brewster-cut barium triborate (BBO) crystal of 1 cm length is mounted at the strong focus of a bow tie cavity at Brewster's angle. We typically couple approximately 90% of the incident light into the cavity and achieve a build up between 50 and 100. We compensate astigmatism introduced by the BBO crystal by using an appropriate angle of reflectance on the curved mirrors of the build up cavity. We lock the length of the cavity to the input light using an H.-C. locking scheme with feedback on a small, piezo-mounted mirror. This produces a beam of 313 nm light of 10-25 mW in the case of the RD and BD lasers. In the case of the Raman laser, with significantly higher visible laser power, we obtain approximately 100 mW. The astigmatism of these UV beams is corrected using the combination of a cylindrical lens and a spherical lens.

From these UV laser sources, we derive pulses of the correct frequency and duration for experimental operation using a series of AOMs. I will describe the AOM system independently for the three laser systems. For the RD laser, we need separate beams that connect the two ground state hyperfine manifolds to the $P_{1/2}$

resonance. We lock the visible laser to a molecular iodine feature such that the second harmonic is centered between the resonances of the two hyperfine ground state manifolds and the $P_{1/2}$. In order to produce the two frequencies required for repumping, we span the hyperfine splitting using two AOM's tuned to produce beams shifted by ±636 MHz. Both beams are switched using a 200 MHz AOM in double pass configuration (Fig. 3.2.1).

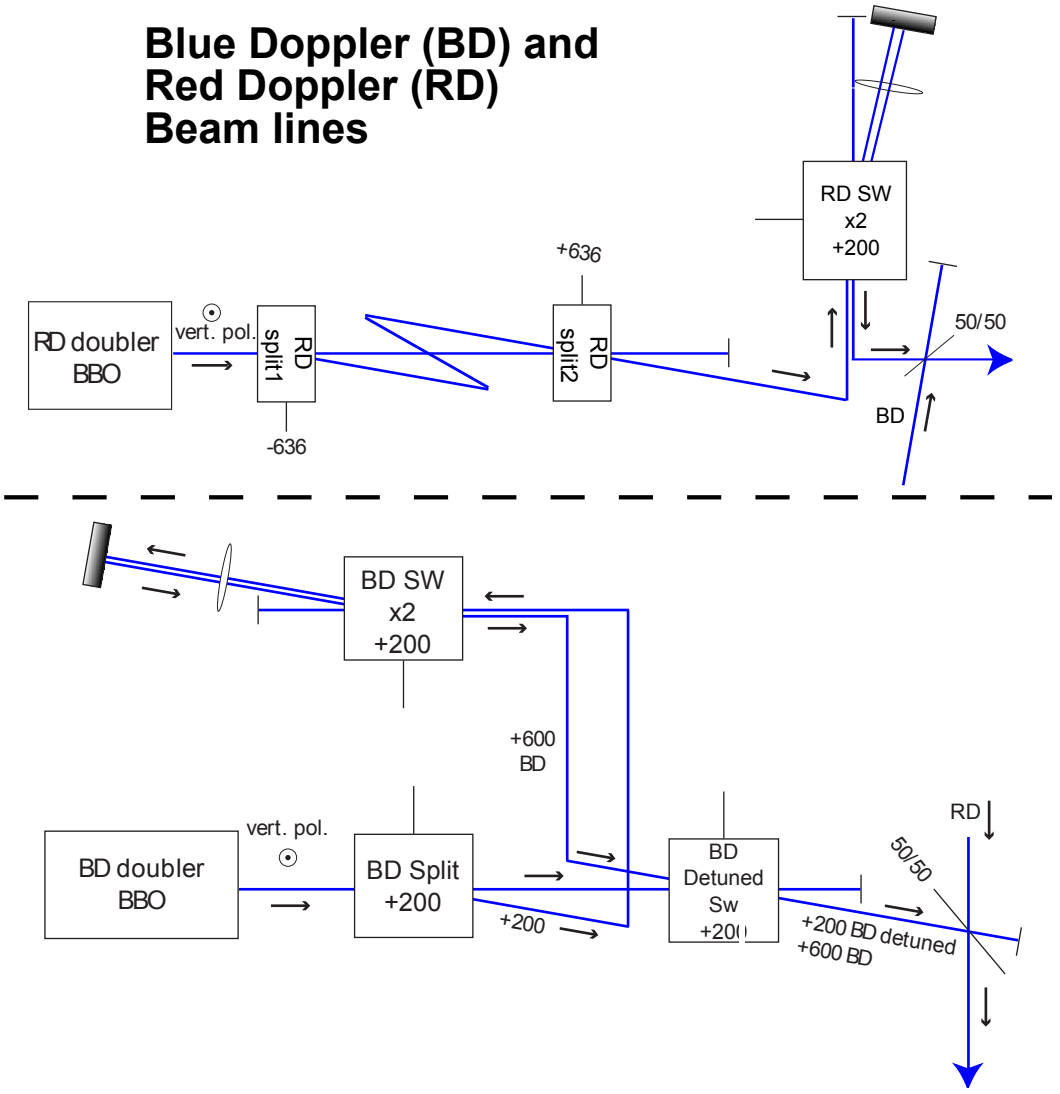

Figure 3.4: Blue Doppler and red Doppler AOM schemes.

For Doppler cooling and detection with the BD laser, we require one beam that is tunable across the $|\downarrow\rangle_{\mathrm{Be}} \rightarrow |P\rangle_{\mathrm{Be}}$ optical resonance (BD), and a separate beam detuned 200 MHz lower in frequency (blue

Doppler detuned or BDD). Near the output of the doubling cavity, a 200 MHz AOM splits the near resonant beam toward a double pass AOM with a tuning range of approximately 40 MHz (Fig. 3.2.1). A third 200 MHz AOM is used to switch the detuned beam and to overlap it with the near resonant beam. The two beams from the BD laser are overlapped with the two beams of the RD laser using a 50/50 beam splitter. Together, they are spatially filtered using a 25 um pinhole at the focus of a telescope and directed towards the trapping region. All of the beams need to be σ^- polarized. The polarization is filtered using a Wollaston prism and adjusted with a quarter wave plate mounted on a mirror mount so that the angle can be precisely adjusted.

The Raman laser is tens of GHz detuned from either of the ${}^2S_{1/2} \rightarrow^2 P_{1/2}$ or ${}^2S_{1/2} \rightarrow^2 P_{3/2}$ resonances. Due to this detuning, the linewidth and the absolute frequency of the Raman laser is not as critical as for BD or RD. For this laser system we neither stabilize to an external reference cavity nor to molecular iodine. We require two beams separated in frequency by the hyperfine splitting (approximately 1.2 GHz) with the difference frequency tunable in order to scan across the ion motional spectrum. We accomplish this with a double pass AOM in both beams as well as a single pass switch AOM in both beams, all centered near 200 MHz. One set of AOMs is aligned to diffract the beam into the -1 order producing "red Raman" (RR) while the other set of AOMs is aligned to diffract the beam into the +1 order producing "blue Raman" (BR). The double pass AOM in the RR beamline has a tuning range of 40 MHz to provide the necessary adjustments in the difference frequency (Fig 3.2.1). Both beams are spatially filtered and focused into the trap with beam waists of approximately 20-40 μm. The BR beam is set to π-polarized and the RR beam is σ^--polarized, both using a quarter-wave plate in combination with a half-wave plate, to drive transitions between the two qubit levels.

3.2.2 Al^+ lasers

To interact with the Al+ atomic system we require two laser sources near 267 nm. I will call them respectively the ${}^3P_0$ laser and the ${}^3P_1$ laser referring to the atomic resonance each one drives. The basic design of both of these systems is the same. The laser source is a commercial fiber laser near 1070 nm with a approximately 50 mW in a linewidth of a few kHz. This light is amplified to a power between 1 W and 2 W

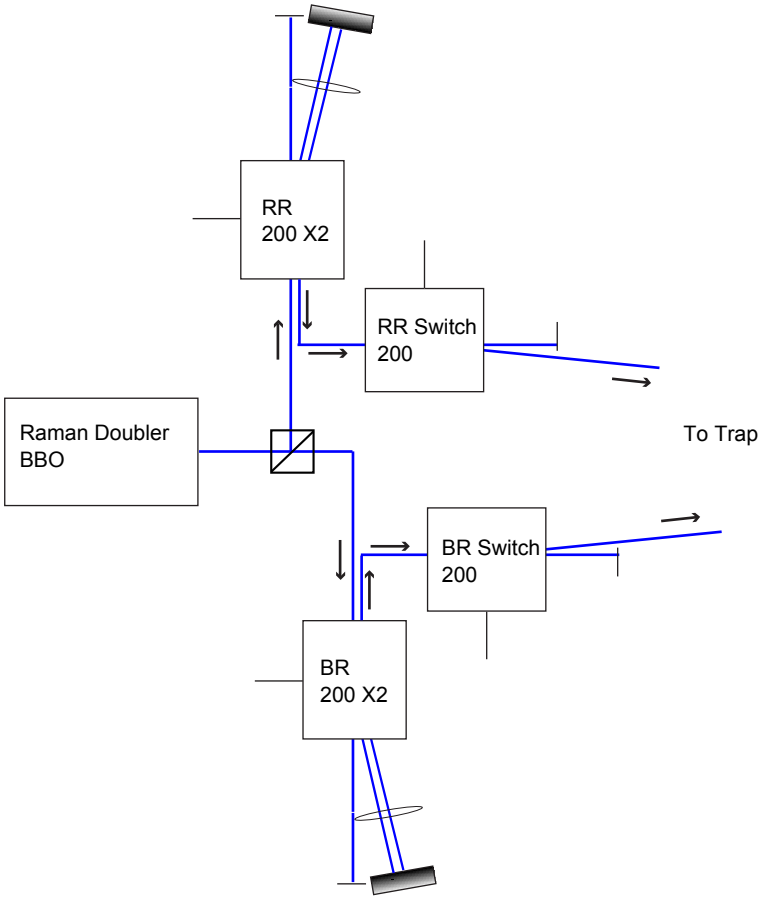

Figure 3.5: Raman AOM scheme.

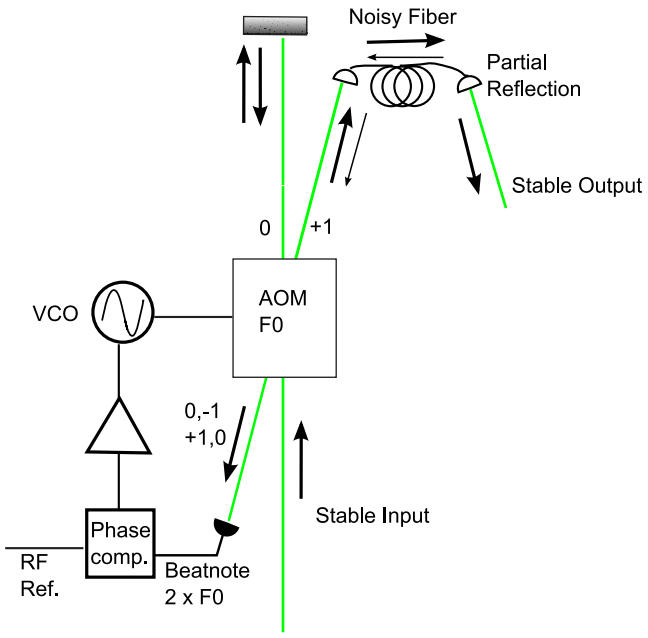

Figure 3.6: Diagram of the fiber-noise cancelation setup.

with a home-built Yb-doped fiber amplifier pumped with laser diodes (4 W) near 976 nm. The 976 nm pump light is combined with the 1070 nm signal light into a dual-clad fiber using a wavelength-division multiplexer and they co-propagate in the gain fiber. To limit the effect of optical feedback to the laser source we use two optical isolators - one between the laser source and the amplifier and another at the output of the amplifier. The 1070 nm light is frequency doubled using non-critical phasematching (T $\sim$ 140 C) in a lithium triborate (LBO) crystal (2 cm in length) surrounded by a build-up cavity. Both laser systems achieve several hundred mW of visible power, most of which is directed through an optical fiber to the optical table that supports the ion trap. A small part of the visible light is sent via optical fiber towards an ultra high-finesse cavity. The laser is locked to the cavity using a Pound-Drever-Hall (PDH) locking scheme that feeds back on an AOM at the fiber laser output. The visible light is frequency doubled in a bowtie cavity using BBO in the case of the $^3P_0$ laser and potassium dideuterium phosphate (KD*P) in the case of the $^3P_1$ laser. The $^3P_1$ laser typically produces 5 - 25 mW of UV power while the $^3P_0$ laser typically produces 1 mW. For most experiments only a small fraction of this laser power is needed.

The $^3P_0$ laser needs to have an ultranarrow linewidth on the order of 1 Hz for addressing the $^1S_0 \rightarrow {}^3P_0$ resonance. For this reason the reference cavity (finesse $\sim$ 50000) used to stabilize it is housed in a vacuum

chamber that is carefully isolated from vibrations and thermal fluctuations [Young 99]. In addition, the laser beam can acquire noise due to vibrations in the optical fibers that transmit visible light between optical tables. A beam coupled into the fiber with a linewidth of 1 Hz might be broadened to the kHz level at the output facet. This noise is actively canceled by monitoring the phase of a beatnote between a reference beam near the input to the optical fiber and a partial reflection from the fiber endface [Bergquist 92, Ma 94]. A diagram of the basic setup for canceling fiber noise is given in Fig. 3.2.2. The stable input light is diffracted by an AOM with frequency $F0$ (generally 40 - 80 MHz), and the +1 order diffracted beam is launched into the fiber. The end face of the fiber is cleaved flat so that a 4 % reflection travels back through the fiber and overlaps with the first order diffraction from the AOM. The reference beam is derived by retroreflecting the zero-order beam from the AOM. The geometry of this setup ensures that the retroreflected beam is aligned to be diffracted into the -1 order of the AOM, and is overlapped with the undiffracted return beam from the fiber. These two beams impinge on a fast photodiode which picks up their beatnote at frequency $2 \times F0$. The phase of this beatnote is compared to an RF reference signal and the phase difference is fed back to a voltage-controlled oscillator (VCO), which drives the AOM. Separate, but nearly identical systems compensate fiber noise for the light directed through optical fiber toward several different components of the experimental system including the ion trap and the reference cavity. In contrast, the $^3P_1$ laser system requires a linewidth on the level of 1 - 10 kHz, so the reference cavity used to stabilize it is not housed in a highly isolated environment and it is not necessary to compensate for noise introduced in the optical fibers.

The 267 nm laser beams from both the Al^+ laser systems is switched toward the ion trap using AOMs. In the case of the $^3P_0$ laser two AOMs centered at 200 MHz switch the light through two different laser access ports towards the ions. In the case of the $^3P_1$ laser system, a greater tuning range (10s of MHz) is required to tune across the ion Zeeman structure and motional spectrum. We use a double-pass AOM to provide a tuning range of 40 MHz. Two single-pass AOMs near 200 MHz, can separately switch the beam through either of two laser access ports towards the trap (Fig. 3.2.2). One of these (3P1-σ) is used to provide a pure σ^+ or pure σ^- polarization depending on the side of the Al^+ Zeeman structure being probed. This polarization depends on the rotation of a half-wave plate, which is mounted on a servo-motor system and controlled digitally by adjusting the duty cycle of a TTL signal. The polarization of the second beam 3P1-π

can be adjusted to be pure π polarization or σ^+/σ^-.

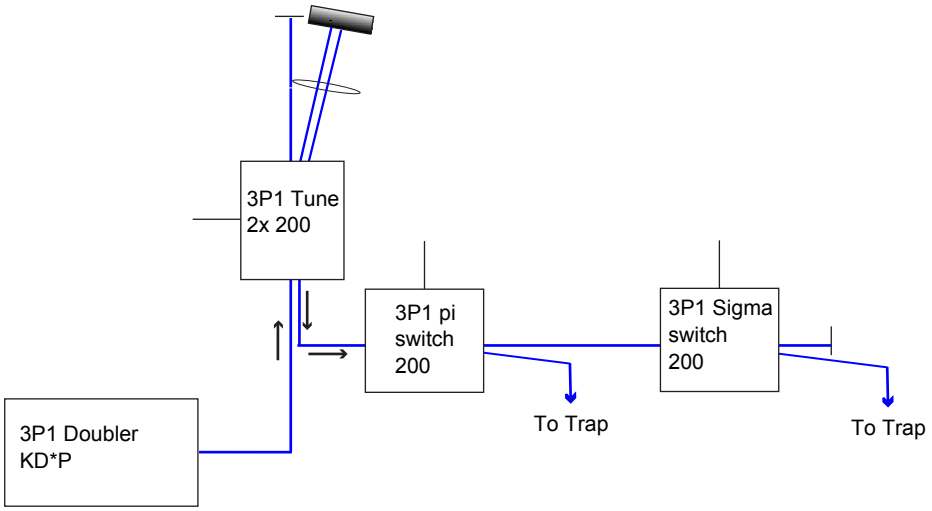

Figure 3.7: $^3P_1$ AOM setup.

3.2.3 Mg^+ Lasers

To interact with Mg^+ we require lasers at 280 nm. The capabilities necessary for controlling the Mg^+ atomic system (i.e. cooling, state preparation, detection and stimulated raman transitions) are similar to those described for Be^+. In the case of Mg^+, a different scheme for repumping and state preparation has been developed to eliminate the need for a laser equivalent to the RD laser. Instead of two beams resonant with the $S_{1/2} \rightarrow P_{1/2}$ transition we use a combination of pulses connecting $S_{1/2}$, F= 2 to $P_{3/2}$, as well as stimulated Raman pulses connecting the two hyperfine levels. The end result is the same, with the pulses driving population from one qubit level to another with a minimal number of spontaneous scattering events that could heat the ions. The two laser sources, Mg-Doppler and Mg-Raman, are respectively derived from 1) a dye laser at 560 nm similar to the Be^+ laser systems and 2) a fiber laser at 1120 nm similar to the Al^+ laser systems. Mg-Doppler is frequency stabilized by dither locking to a reference cavity external to the dye laser cavity. The visible light is frequency doubled to 280 nm with a BBO doubling cavity. The 1120 nm fiber laser has a natural stability that is sufficient for stimulated Raman transitions in Mg^+ and is not stabilized to any external reference. Like the Al^+ laser system it is frequency doubled first to 560 nm using an LBO doubling cavity, then to 280 nm using a BBO doubling cavity. The 1.8 GHz hyperfine splitting in

Mg^+ is spanned for both Mg-Doppler and Mg-Raman with a series of AOMs similar to the basic design of the Be^+ laser systems, but in slightly different configurations.

3.2.4 Experimental Control

In a general sense, the input to each ion experiment is a series of laser pulses at a particular frequency, duration and phase. The output is a number of photon counts observed during a detection pulse at the end of the experiment. Both the application of laser pulses and the acquisition of ion fluorescence is controlled by a field-programable gate array (FPGA) system designed specifically our ion trap experiments [Langer 06]. At a higher level, we use a C++ program written in-house by Till Rosenband that controls and schedules sets of experiments and analyzes their outcome. Although it is outside the scope of this thesis (and my knowledge) to discuss technical details of the system, I will give a basic overview of it and describe how the architecture is necessary for our experiments.

The FPGA is clocked at 62.5 MHz and is programmed to control the frequency and phase of a set of direct digital synthesizers (DDSs), which have a clock speed of 1 GHz. The FPGA also applies TTL pulses of the appropriate duration to switch the RF signals toward various AOMs. The photon counts during fluorescence detection are imaged onto a photomultiplier tube (PMT) and the resulting electronic signals are passed through a thresholding circuit that converts them to a TTL signal, which is input to the FPGA. The FPGA records the number of photon counts for a particular experiment and stores them where they can be read out digitally. A particular experiment is defined by the sequence of RF pulses, sometimes overlapping in time, and each consisting of (at most[2]) a DDS frequency, a DDS phase and a TTL pulse duration. The set of instructions that we use to define this pulse sequence is called a digital control file (dc-file) and it is translated into FPGA code by a compiler designed in-house [Langer 06]. This system allows for precisely defined pulse frequencies, phases and times all switchable at a fast time-scale. The FPGA system can scan variables so that the ion response as a function of any of the pulse characteristics can be observed. This affords a great degree of flexibility in quickly designing and redesigning an experiment.

The C++ control program performs the basic tasks of writing a series of dc-files, and interpreting the

[2] Many pulses are applied to an AOM at a fixed frequency, so they consist of only the TTL pulse duration.

results of experiments. These capabilities combined allow for a high degree of automation in the experimental control. For example, it enables automatic calibration of atomic resonance frequencies and optimum pulse durations. It also enables interleaved experiments so that certain aspects of the experiments can be actively monitored and adjusted to protect the experimental results from slow uncontrolled drifts in such parameters as bias fields near the ion or laser frequencies.

As an example of the way this automation is applied, consider the precise calibration of an atomic resonance frequency. The experiment consists, of laser cooling, an interrogation pulse near the atomic resonance frequency, and detection of the ion state. The FPGA is instructed to scan the interrogation pulse across a certain range near the frequency where the atomic resonance should be, and the results are read out as a series of photon counts each referring to a particular frequency. The C++ program can then perform such tasks as binning and averaging the photon counts and plotting the average fluorescence as a function of frequency. It can also fit the plot to a known functional form, thereby extracting a calibration of the atomic resonance frequency. Furthermore, the program is set up to sequentially calibrate many parameters, such that, for example, all of the resonances in the motional spectrum and their Rabi rates can be calibrated at once. This is convenient because many tasks must be performed periodically to maintain optimum calibration and this reduces the work to a single button press.

A related feature that has been crucial to performing the experiments described in this thesis is the ability to continuously servo such parameters as resonance frequencies or trap voltages. To do this the parameter can be modulated between two states from one set of ion experiments to the next, and the difference in the fluorescence signal from the ion serves as an error signal. If a particular "primary" experiment requires the constant recalibration of a parameter, the control program interleaves these servo experiments with the primary experiments to maintain a continuous calibration. As an example, our experiments require that position of the ions be maintained on the trap axis to avoid micromotion. The position often changes due to stray electric field from photoelectrons that build up on insulating surfaces. To servo this, we modulate a control electrode and perform an experiment that looks for the presence or absence of micromotion. Several experiments can be designed to make ion fluorescence sensitive to micromotion, but in all cases the servo attempts to adjust the center voltage of the control electrode such that the fluorescence signal is balanced

and the ion rests at a micromotion minimum.

3.3 Experimental Primitives

Several operations are necessary for carrying out the experiments of this thesis, and I will describe the basics for the Be-Al experiment in particular here. The protocols for the Mg-Al experiment are similar, but will not be discussed.

3.3.1 Loading ions

The loading of Be^+ is performed by electron-impact ionization of neutral beryllium atoms from a thermal beam. The thermal beam comes from a beryllium oven, which consists of a thin beryllium wire coiled around a tungsten "heater" and is mounted near the trap volume. We run a current of ∼0.9 A through the tungsten wire, heating the beryllium near its melting point of 1278 C. A cone of metal surrounding the oven shields most of the electrode surfaces from the beryllium atoms and transmits only a small solid angle of the beam through an aperture toward the trapping region. Simultaneously, an electron gun filament is heated by running ∼1 A of current through it, emitting electrons, which are accelerated across a voltage of 50-80 mV and bombard atoms in the trapping region. Typically, after 20-40 seconds, an atom will be ionized in the trap with a sufficiently low energy for it to be laser cooled by the detuned BD beam. This ion will be imaged on the CCD camera and appear as a bright dot, which allows us to manually stop the loading process before more ions appear.

We can only load Al^+ when a Be^+ is already trapped, since we can not detect the Al^+ directly through fluorescence. However, the presence of a second "dark" ion can be detected by monitoring the position of the Be^+, which moves by a couple microns due to Coulomb repulsion. The process is similar to loading Be^+. The aluminum oven is composed of an aluminum reservoir heated by a tungsten wire, both embedded in an alumina tube. Neutral aluminum atoms are either ionized by electron impact or by resonance-enhanced two-photon ionization (photoionization). For photoionization, we use a commercial external cavity diode laser with a wavelength of 396 nm. Aluminum has a $3s^2 3p$ ground state with two fine-structure components, $^2P_{3/2}$ and $^2P_{1/2}$, split by a wavenumber of approximately 100 cm^{-1}. Both of the ground state fine-structure

components are significantly occupied at the oven temperature and we address the $^2P_{3/2} \rightarrow ^2 S_{1/2}$ transition with the photoionization laser. From the $^2S_{1/2}$ state, another 396 nm photon is sufficient to reach the ionization threshold at $\tilde{6}$ eV.

Since the presence of an Al^+ ion can only be inferred by its effect on Be^+, the successful loading of a Be-Al pair must be confirmed by measuring the motional frequencies of the two-ion array. Similarly, for loading a larger number of ions the number of dark ions can often be determined by examining the position of the Be^+ ion(s), but the species of the ions can only be verified through spectroscopy of the motional spectrum.

3.3.2 Laser Cooling

Laser cooling is the first step in most experiments. This process first involves Doppler cooling all normal modes of motion by applying a series of BD laser pulses [Wineland 79, Wineland 78]. First a BD-detuned pulse of 200 μs serves to cool ions that may have too high an energy to be efficiently cooled by the near resonant beam. Next we apply a series of near resonant pulses (detuned red by $\gamma/2$) lasting 200-1000 μs depending on the number of ions and their configuration. For a single Be^+ ion there are only 3 normal modes which are all cooled efficiently, so a single pulse for 200 μs is sufficient. For the ion array Al-Be-Al, we need two pulses at different trap conditions, lasting close to 1 ms in order to approach the Doppler limit (see Sec. 4.4 and Sec. 5.2.3.2). In general, due to differences in motional coupling strength, each particular configuration of ions will require different trap conditions and Doppler cooling times to reach the Doppler limit.

After Doppler cooling, for many experiments, we also cool the axial modes of motion close to the ground state [Diedrich 89] by resolved-sideband Raman cooling. Raman cooling involves a series of pulses with the Raman lasers addressing the first red sideband for each axial mode separated by repumping pulses using the RD laser. We choose the range of Fock-states to cover in the cooling process which improves the cooling efficiency by adjusting the sideband π-time based on the Fock state according to Eq. 2.9. For example, consider the case of cooling one Be^+ and one Al^+ using sideband pulses on Be^+. We cool both the in-phase and out-of-phase axial modes beginning from a π-time appropriate for $n = 15$ using 2 repetitions

at each π-time. The π-times are calculated based on the calibrated π-time near the ground state of motion, the known Lamb-Dicke parameter and Eq. 2.9. We interleave cooling cycles on the two modes so that first we apply a sideband pulse at the in-phase mode frequency, for the appropriate time, repump using RD, then repeat the process for the out-of-phase mode frequency. Interleaving cooling cycles reduces the probability that one mode heats while the other is being cooled. The interleaved cycles are repeated at the same π-times, then we move to the next lower Fock-state π-times and perform another set of cooling cycles. In this example, we step down the ladder from $n = 15$ to $n = 1$ performing interleaved cooling cycles for each Fock state on the two axial modes twice each. The entire process takes approximately 1 ms.

3.3.3 Al^+ State Preparation

At the beginning of each experiment involving the Al^+ system, the state of Al^+ must be prepared in either $^1S_0, m_F = \pm 5/2$. This is accomplished by applying a series of lasers pulses on transitions from $^1S_0$ to $^3P_1$ using the 3P1-σ beam with polarization σ^+ or σ^- matched to the sign of the target m_F state. We attempt to maximize the efficiency of this process by first optimizing the polarization of the 3P1-σ beam and second calibrating the frequencies and π-times of all of the transitions leading to the target state.

To optimize the polarization of 3P1-σ we perform a depumping experiment. If the polarization is pure σ then, in applying a pulse to $^1S_0$, $m_F = \pm 5/2 \rightarrow {}^3P_1$, $m_F = \pm 7/2$, the transition probability will be maximized. However, if the polarization is imperfect, there will be a finite probability of making a transition to $^3P_1, m_F = \pm 5/2$ or $^3P_1, m_F = \pm 3/2$, both of which can decay out of the target $^1S_0$ state. This will show up in the experiment as a drop in the transition probability. To optimize the polarization we run this experiment continuously and adjust the angle and rotation of both a HWP and QWP to maximize the transition probability.

We also calibrate the frequency and π-times of the optical pumping pulses in order to pump Al^+ more efficiently to the target state. To do this, we first calibrate the frequency and π-times of the two carrier transitions at opposite sides of the Zeeman spectrum, ($^1S_0$, $m_F = \pm 5/2$) $\rightarrow {}^3P_1$, ($m_F = \pm 7/2$). Although during the calibration the polarization is not perfected, we still can get a reasonable signal assuming the polarization is not grossly misaligned. Based on the difference frequency between the two transitions, the

magnetic field can be determined. With this, we use the Breit-Rabi formula, to determine the frequencies of all of the transitions[3] . In addition, we scale the Rabi rates based on the Clebsch-Gordon coefficients for each of the transitions. Based on these calibrations we apply a series of pulses at a particular frequency, duration and polarization appropriate for the target state desired. The lifetime of $^3P_1$ is approximately 300 μs, which is the limiting timescale for optical pumping. At any step in the process we do not know which state the Al^+ system occupies, so we apply a series of pulses sweeping towards the target state, then wait for a time that allows the $^3P_1$ state to decay. We repeat this through a specified number of repetitions. To confirm that we have reached the target state, we apply pulses to the target state from ($^1S_0$, $m_F = \pm 5/2$) to $^3P_1$, ($m_F = \pm 7/2$) and see that we do indeed make transitions.

3.3.4 Monitoring and Locking the Trap Conditions

Due to the effects of stray charges on insulating surfaces in the trap several trap conditions can drift during the course of a set of experiments. As a result we typically use periodic, interleaved experiments of the type described in Sec. 3.2.4 to fix the ion positions in three dimensions and to lock the axial confinement frequency.

3.3.4.1 Micromotion

Radial displacement of the ions due to uncompensated radial bias fields cause excess micromotion. All of the experiments we perform require the micromotion to be minimized, because its amplitude can affect the laser cooling efficiency and cause time-dilation shifts to the ion resonance frequency. To actively compensate micromotion, we use the strategy described in Sec. 4.3 to servo the DC bias fields (see Sec. 3.2.4). To detect uncompensated bias fields, we look for radial mode amplitude along the trap axis by applying a sideband pulse with the Raman beams. To the extent that the Raman beams are well-aligned $\mathbf{\Delta k}$ will be directed along the trap axis and should not couple at all to the radial modes. However, if there is a radial bias field, the mode amplitudes change direction, and the radial modes will, in general, have some projection along $\hat{z}$. This can be observed by looking for Rabi flopping on the radial sidebands. For the

[3] An evenly spaced set of frequencies based on the linear Zeeman effect would be sufficient at the B-fields we typically apply.

different ion configurations used in this thesis (Be-Al, Al-Be-Al, and Be-Al-Al-Be) we choose an appropriate radial mode for which the axial mode amplitude on Be^+ increases significantly with a radial bias field. We modulate the voltage on compensation electrodes symmetrically about the nominally compensated value. An uncompensated field shows up as a difference in the transition probability between the two modulation states, which we compensate by adjusting the nominal center. In addition to changing the mode amplitudes, a radial bias field will change the mode frequencies. For this reason, in conjunction with the bias fields, we monitor the mode frequencies by modulating the sideband pulse frequency about the nominal center and adjusting based on an imbalance in the transition probability. To fully compensate the bias fields we servo two orthogonal radial directions (along the $\hat{x}$ and $\hat{y}$ directions). We generally achieve at least a 50:1 ratio between the transition strengths of the carrier and the micromotion sideband.

3.3.4.2 Trap Frequency

Stray charge buildup on the trap can also cause a change in the axial trap frequency, which affects the fidelity of sideband pulses. This is actively compensated using a similar servo strategy to that described above. In this case we apply an RF signal to a trap endcap to excite motion at the ion in-phase axial frequency. If the RF signal is at the motional resonance it will drive energy into the motion. We can detect the motion because it depletes the strength of a qubit carrier transition into the motional sidebands. We use a servo to fix the motional resonance to a particular value, by modulating the frequency of the RF signal between two symmetric values about resonance. We raise or lower the voltage to all endcap electrodes simultaneously to balance transition probabilities between the two modulated values. In this way the resonance frequency is fixed to be the desired value.

3.3.4.3 Axial Position

Due to imperfections in the trap geometry there is residual micromotion directed along the axis of the trap, for which the amplitude depends on the ion position in relation to the trap electrodes. As a result, this micromotion amplitude changes with stray charge buildup. We actively compensate this during the course of experiments by relying the the alignment of the laser beams with the minimum of the axial

micromotion. If we align the beams at conditions where we know axial micromotion is compensated, we can then adjust the position of the ions to be centered in the laser beams to restore this compensation. The parameter modulated in this case is a differential endcap voltage, which adjusts the ion position axially without changing the motional frequencies. We balance the qubit carrier Rabi rate in the two modulated states to identify the compensated differential voltage.

Chapter 4

Two-Species Ion Dynamics

Two fundamental requirements for both precision spectroscopy and quantum information processing in an ion trap are the ability to laser cool and detect a single ion. This places a stringent constraint on the ion electronic structure, and only a small number of ion species, including the singly ionized atoms of group IIa and IIb, can be directly investigated in this way [Metcalf 99]. In particular, Doppler cooling [Wineland 79] and resonance fluorescence detection [Bergquist 86] both benefit from the presence of a strongly-allowed cycling transition. For most ions, the electronic level structure is complicated enough that isolating a cycling transition is experimentally infeasible. Other ions, such as Al^+, have appropriate transitions but only at laser wavelengths that are currently inaccessible [Wineland 02]. Molecular ions are also interesting candidates for spectroscopy and quantum information processing [DeMille 02, Schmidt 06], but optical pumping to many states of the rovibrational degrees of freedom generally prohibit cycling transitions. Another situation where Doppler cooling can be problematic is in quantum information processing (QIP) experiments. Here, direct cooling may be possible, but doing so would disturb the information stored in the qubit [Kielpinski 02].

All of these considerations motivate the use of two ion species trapped in a single trap and coupled via Coulomb repulsion to enable sympathetic laser cooling. In this technique the primary ion species is cooled indirectly through its Coulomb interaction with the cooling ion species. Sympathetic cooling has been demonstrated in several systems [Barrett 03, Blinov 02, Schmidt 05]. In recent experiments, sympathetic recooling of ion qubits has enabled the entanglement of harmonic oscillator states in an ion trap array [Jost 09] as well as the realization of repeated logic operations without loss of fidelity [Home 09]. The exchange of energy between two ion species also provides the means for indirect state detection, whereby information in

an ion's electronic structure is transferred to the shared motion and read out by the sympathetic cooling ion. A particular scheme for indirect detection has been applied to precision measurements of $^{27}Al^{+}$[Schmidt 05, Rosenband 07].

In this chapter we investigate the properties of two-species ion arrays in a linear rf Paul trap. First, in Sec. 4.1, we present a mathematical model for dynamics of the two-species arrays. In Sec. 4.2 we describe a method for fixing the arrangement of the ions, which takes advantage of the mass dependence of the trap confinement. We show specific examples of this for small numbers of ions. In Sec. 4.3 we consider the implications of these ideas for the suppression of motion at the frequency of the rf potential, or "micromotion". We discuss how properties of a two-species ion array can enhance or diminish micromotion caused by uncontrolled electric fields and we briefly review how micromotion can be actively compensated by monitoring the motional spectrum. In the final section, Sec. 4.4, we consider Doppler cooling in the context of multiple species ion arrays and examine ways of optimizing the cooling efficiency.

4.1 Mathematical Model for Multiple Species Ion arrays

The basic geometry of a linear rf Paul trap [Paul 90] has been described in numerous publications [Wineland 98]. In this section, we denote the ion positions as the components of $\mathbf{u}$, such that $\{u_{3i+1}, u_{3i+2}, u_{3i+3}\}$ respectively specify the x, y and z coordinates of the ith ion. We consider an array of N ions such that and $i \in [0,\, N-1]$. In some cases it will be convenient to use the equivalent notation $\mathbf{r}_i = \{x_i, y_i, z_i\}$. We take the z coordinate to be parallel to the axis of the trap, along which the rf electric fields vanish. Typically in experiments, the saddle point in the static potential coincides with a point on the rf nodal line. This is the condition that minimizes the effects of micromotion, because the static fields do not displace the ions into the rf pseudopotential. However, in what follows, it will be important to also consider the effects of a bias field, $\mathbf{E}_{\mathrm{r}} = E_x\hat{x} + E_y\hat{y}$.

The equilibrium positions of N trapped ions in three dimensions are determined by minimizing the potential energy of the system with respect to the $3N$ degrees of freedom. The total potential energy includes terms from the external electric fields as well as terms from the Coulomb interaction between ions. We write

the potential energy from static external fields as

$$V_{\rm dc} = \frac{1}{2}\sum_{i=0}^{N-1}\sum_{j=1}^{3}\kappa_j u_{3i+j}^2 + Q\sum_{i=0}^{N-1}(E_x u_{3i+1} + E_y u_{3i+2}), \tag{4.1}$$

where the first term sums components from the static trapping fields, specified by the parameters κ_1, κ_2 and κ_3, which represent the curvatures associated with the static potential in the x, y and z directions respectively. To satisfy Laplace's equation, we must have $\sum_j \kappa_j = 0$. Since we rely on the static potential to provide confinement in the z direction, $\kappa_3 > 0$ and $\kappa_1 + \kappa_2 < 0$. The particular values of these curvatures are determined by the magnitudes and geometries of the applied fields. The second term in Eq. 4.1 takes into account a bias field in the x and y directions. A bias field in the z direction amounts to a shift of the coordinate origin, and has been omitted.

In the pseudopotential approximation we write the potential energy from the radial rf fields as

$$V_{\rm rf} = \frac{1}{2}a_r\sum_{i=0}^{N-1}\frac{1}{m_i}(u_{3i+1}^2 + u_{3i+2}^2), \tag{4.2}$$

where m_i is the mass of the ith ion and a_r characterizes the strength of the radial confinement. The potential energy of a single ion of mass m_0 is $V_{\rm dc} + V_{\rm rf}$. In this case we can easily relate $\{\kappa_j\}$ and a_r to experimentally accessible quantities. Since the axial confinement depends only on the static trapping potential, $\kappa_3 = m_0\omega_z^2$, where ω_z is the observed resonance frequency for ion motion along the trap axis. In the radial direction we have $a_r/m_0 + \kappa_1 = m_0\omega_x^2$, and $a_r/m_0 + \kappa_2 = m_0\omega_y^2$, which together with $\kappa_1 + \kappa_2 = -\kappa_3$ fully characterize the trap conditions for a single ion. Note that these measurable frequencies for a single ion are independent of $\mathbf{E}_R$, a condition which is not true for multiple ions of different species.

For $N > 1$, the ions interact via their mutual Coulomb repulsion. This contributes to the total potential energy with

$$V_{\rm ion} = \frac{Q^2}{8\pi\epsilon_0}\sum_{\substack{i,i'=0\\ i\neq i'}}^{N-1}\frac{1}{|\mathbf{r}_{i,i'}|} \tag{4.3}$$

where $|\mathbf{r}_{i,i'}|$ is the distance between ions i and i' and is given by

$$|\mathbf{r}_{i,i'}| = \Big[\sum_{j=1}^{3}(u_{3i+j} - u_{3i'+j})^2\Big]^{\frac{1}{2}}. \tag{4.4}$$

The total potential energy, then, is

$$V_{\rm tot} = V_{\rm dc} + V_{\rm rf} + V_{\rm ion}. \tag{4.5}$$

The equilibrium ion positions, $\mathbf{u}'$, which minimize this potential have been found analytically for $N = 2$ and $N = 3$ in the special case of an axial array [James 98]. In all the results that follow $\mathbf{u}'$ is found by numerically minimizing $V_{\rm tot}$.

In analyzing the motion of the ions about their equilibrium positions, we write the time dependent position as $\mathbf{u}(t) = \mathbf{u}' + \mathbf{q}(t)$. For laser cooled ions ($T \approx 0.1$ mK) the motional amplitudes are on the order of 10 nm, while the inter-ion spacing is on the order of 3 μm. This allows us to take the limit of small oscillations and approximate the potential energy to second order in $\mathbf{q}(t)$. If we define coordinate indices for the $3N$ dimensional space as $l \equiv 3i + j$ and $l' \equiv 3i' + j'$, we can identify the components of a mass matrix $\tilde{M}$ as $M_{l,l'} = \delta_{l,l'} m_i$. Similarly the components of a spring constant matrix $\tilde{K}$ are given by $K_{l,l'} = \frac{\partial^2 V_{\rm tot}}{\partial q_l \partial q_{l'}}|_{\{q_l\}=0}$. Now we can write the Lagrangian as

$$L = \frac{1}{2}\dot{\mathbf{q}}^T \tilde{M} \dot{\mathbf{q}} - \frac{1}{2}\mathbf{q}^T \tilde{K} \mathbf{q}, \tag{4.6}$$

where superscript T denotes the vector transpose. This Lagrangian gives the $3N$ equations of motion

$$\tilde{M}\ddot{\mathbf{q}} + \tilde{K}\mathbf{q} = 0. \tag{4.7}$$

All forces in Eq. 4.7 are linear, leading to oscillatory solutions for $\mathbf{q}(t)$ of the form

$$\mathbf{q}(t) = \mathrm{Re}[\mathrm{C}\mathbf{v}\mathrm{e}^{\mathrm{i}(\omega \mathrm{t} + \phi)}], \tag{4.8}$$

where the scaling factor C and the oscillator phase ϕ are determined by initial conditions. Substituting Eq. 4.8 into Eq. 4.7 leads to the following eigenvalue equation

$$\tilde{M}^{-1}\tilde{K}\mathbf{v} = \omega^2 \mathbf{v}. \tag{4.9}$$

In solving the eigenvalue equation we get the $3N$ oscillator frequencies $\{\omega^{(\alpha)}\}$ and their corresponding normalized eigenvectors $\{\mathbf{v}^{(\alpha)}\}$, for which the component $\mathrm{v}^{(\alpha)}_{3i+j}$ corresponds to the ith ion's relative amplitude in the direction specified by j (x, y, or z) for the mode labeled α. To simplify the notation in what follows we drop the label α and refer to a particular mode implicitly.

The scaling factor C depends on the ion motional state. The state of each mode can be expanded in terms of Fock number states, $|n\rangle$, for which the characteristic amplitude is

$$C(n) = (2n + 1)^{1/2} C_0, \tag{4.10}$$

where C_0 is the amplitude for the ground state of motion. The amplitudes for the ground state of motion can be found using the total kinetic energy,

$$\frac{1}{4}\hbar\omega = \frac{\omega^2}{2}\mathbf{v}^T\tilde{M}\mathbf{v}C_0^2, \tag{4.11}$$

which identifies the effective mass as $m_{\text{eff}} = \mathbf{v}^T\tilde{M}\mathbf{v}$ leading to the usual expression for the extent of the harmonic oscillator ground state wavefunction,

$$C_0 = \left(\frac{\hbar}{2m_{\text{eff}}\omega}\right)^{\frac{1}{2}}. \tag{4.12}$$

Putting this expression with Eq. 4.10 in Eq. 4.8 we can characterize the motion of the ions for any particular distribution of Fock states. The motional amplitudes and frequencies are central in evaluating the interaction between a array of ions and applied laser beams.

The model discussed here represents an ideal linear Paul trap, with the addition of uniform bias fields. Any real trap will exhibit deviations from this ideal model. Although these deviations will usually be sufficiently small to keep the ion dynamics qualitatively unchanged, we mention some common imperfections here. First, the model ignores misalignment between the rf nodal line and the static potential axes. One way a misalignment is manifest is by the existence of a gradient of the x-y bias electric field as a function of the z coordinate. This particular effect can be accounted for in Eq. 4.1 by applying the appropriate functions $E_x(z)$ and $E_y(z)$. Another effect of trap asymmetry is axial micromotion, which refers to rf fields directed along the potential axis. The corresponding rf pseudopotential in the $\hat{z}$ direction can be accounted for by a modification of Eq. 4.2 to include a term that depends on the coordinates u_{3i+3}. A third complication which can occur is higher-order terms in both the static and rf potentials. Traps generally exhibit small anharmonicities but these effects can be significant in certain situations, particularly with multizone microfabricated traps [Rowe 02] and surface-electrode traps [Seidelin 06].

4.2 Ion Reordering

The transport of atomic ions has been studied in the context of single-zone linear traps [Splatt 09], multi-zone linear traps [Rowe 02], and two-dimensional trap structures [Hensinger 06, Blakestad 09]. The emphasis in these experiments was on the requirements for large-scale quantum information processing. A

sequence of quantum gates between selected groups of ions, may require different ions to interact at different steps in a single experiment. The problem discussed here, by contrast, concerns fixing an array of different-mass ions into a particular order independent of the initial order. These techniques are relevant for many experiments involving a small number of ions of unequal mass, including precision spectroscopy and quantum information experiments.

We consider a two-species ion array that has N_0 ions of mass m_0 and N_1 ions of mass m_1, ($N_0, N_1 \in [1, N]$). There are $N-1$ possible mass combinations, and for each of those there are $N!/N_0!N_1!$ ion orders. Those ion orders that are mirror images of each other will exhibit the same motional spectrum making them indistinguishable in our experiments, where we address all ions simultaneously with a uniform laser field. In the following discussion we group the mirror-image orders together and refer to them jointly as an ion configuration.

Uncontrollable collisions with background gas in the ion trap (typically with a timescale of minutes) will tend to heat the ions into a uncrystallized thermal state. Subsequent cooling of the ions into a linear array will put the ions in a random order. We desire, then, a method to rearrange the ions into a particular configuration independent of the initial order. If the radial confinement is sufficiently stronger than the axial confinement the ions will form an axial array with x_i, $y_i = 0$ for all i. Under these conditions, $V_{\mathrm{rf}} = 0$ so the total potential energy is independent of the mass and all $N!/N_0!N_1!$ ion orders will be stable. One way to change the ion configuration, is to increase the ratio ω_z/ω_x or ω_z/ω_y to a point where the ion array becomes purely radial. We use ω_x, ω_y and ω_z to refer to the secular frequencies for a single trapped ion. Another way to change the ion configuration is to introduce a radial bias field such that the ion pseudopotential energy is nonzero. By adjusting the trap voltages, we can find some conditions that have only one stable equilibrium configuration. This will not be a linear array of ions, but instead a two-dimensional ion geometry with some ions displaced radially into the pseudopotential.

4.2.1 Two Ions

We begin by considering the simplest case of two ions, one of mass m_0 and one of mass m_1 held together in a linear Paul trap. There is only one possible on-axis ion configuration since the two ion orders

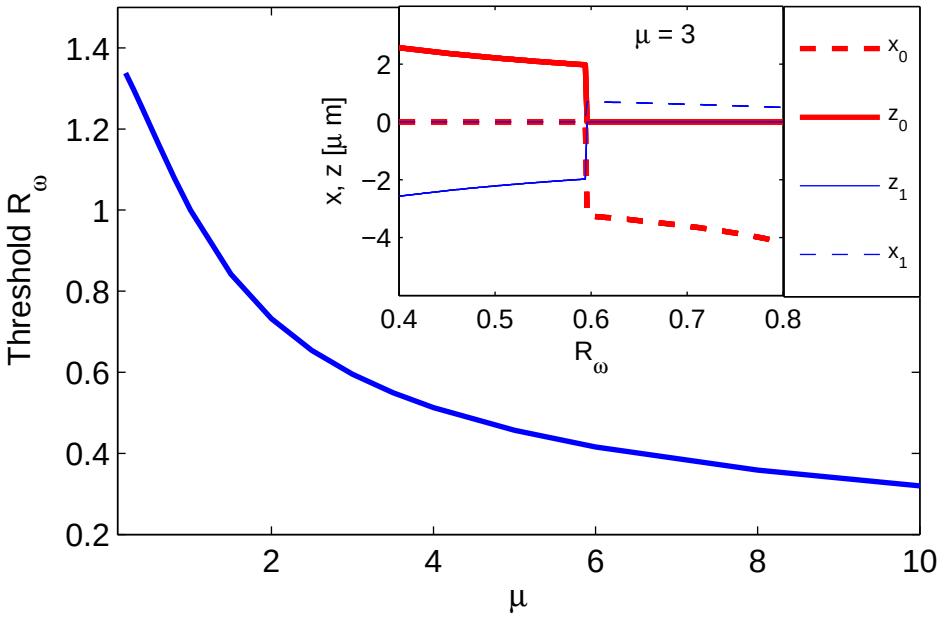

Figure 4.1: Threshold frequency ratio ($R_\omega = \omega_z/\omega_x$) as a function of mass ratio $\mu = m_0/m_1$ for two ions. Here R_ω refers the trap conditions for a single ion of mass m_1. (Inset) A particular example of the ion positions in two dimensions for $\mu = 3$ as a function of R_ω. The sharp change in ion position where $z_i \to 0$ indicates the threshold used to generate the larger plot.

are mirror images. To the extent that the laser intensity is uniform across the ions, the absorption spectrum of the two ion orders are equivalent, but it may be desirable to maintain a particular order to reduce the effect of laser intensity gradients, and it is instructive to examine how this case behaves when adjusting trap parameters.

For simplicity we consider the cylindrically symmetric case where $\kappa_1 = \kappa_2 = -\kappa_3/2$ and restrict the discussion to two dimensions, x and z, which captures the relevant features of the more general case. We specify the trap confinement in terms of the motional frequencies of a single ion of mass m_1 and define $\mu \equiv m_0/m_1$. We study first the conditions under which the axial ion array becomes radial as a function of the frequency ratio $R_\omega = \omega_z/\omega_x$. For $\mu = 1$, the ion array is radial if $R_\omega > 1$. As μ decreases, the threshold ratio increases because the lighter-mass ion is more tightly bound by the pseudopotential. Likewise, with higher μ, the heavier ion is less tightly bound radially and the threshold reduces. In Fig. 4.2.1 we plot the threshold R_ω at which the ions go from a radial to axial array as a function of μ.

Experimentally, R_ω can be raised by increasing endcap voltages, or, equivalently, by lowering the rf voltage. If we begin with an axial array and raise the endcap voltages, the ions reorient into a radial array. At the threshold conditions between a radial and axial array, one of the radial mode frequencies reduces to zero. Since the voltages are adjusted during a finite period of time, the transition is non-adiabatic and the ions will gain kinetic energy during the process, which generally causes them to decrystallize. If there is motional damping, for example due to laser cooling, the ions recrystallize into the new equilibrium positions. The threshold conditions correspond to parameters at which a radial mode frequency of the two-ion array reaches zero.[1] A vanishing mode frequency is a general feature of trap conditions at the boundary between ion configurations.

The inset of Fig. 4.2.1 shows a particular example ($\mu = 3$) of the equilibrium ion configurations as a function of the trap frequency ratio. Note that, in this example, a particular radial orientation has been chosen for the two ions, although the reverse arrangement (i.e. $x_i \rightarrow -x_i$ for $i = 1, 2$) is equivalent. There is a probability of 1/2 that either arrangement is observed. Similarly, if the trap conditions are relaxed back through the threshold to make an axial array, either ion order is equally probable. This means that changing R_ω alone is not useful for choosing an orientation of two ions.

The ion positions can also be manipulated by the application of a radial electric field, E_x. For $E_x \neq 0$ the heavier ion will occupy a position further from the axis due to the mass dependence of the ponderomotive potential. In Fig. 4.2.1 we give a particular example of the ion positions as a function of the radial bias field for $\mu = 3$ and $\{\omega_x, \omega_y, \omega_z\} = 2\pi \times \{13, 13, 4\}$ MHz. Here we note the qualitative differences between this case and the case of changing R_ω. First, there is no sudden change in position as the ions go from an axial to a radial array. However, as with the case of raising R_ω, a radial mode frequency drops to zero at the point where the ions form a radial array. Here, there is a particular orientation defined by the sign of E_x, which is important in fixing the ion order. With a radial array of known orientation, one can apply a electric field gradient, $E_z = dE_z/d_x \times x$, to turn the ion array [Splatt 09]. If the applied voltages are subsequently reduced to zero to form an axial array, the ions will have a known order. This technique has been applied

[1] For two ions there are four radial modes, two in radial direction. In one mode, the ions move in-phase, while in the other, the ions move out of phase. The out-of-phase mode is always lower in frequency and this is the mode that reaches zero frequency at threshold. Conceptually this makes sense because the ions must move in opposite directions to form a radial array

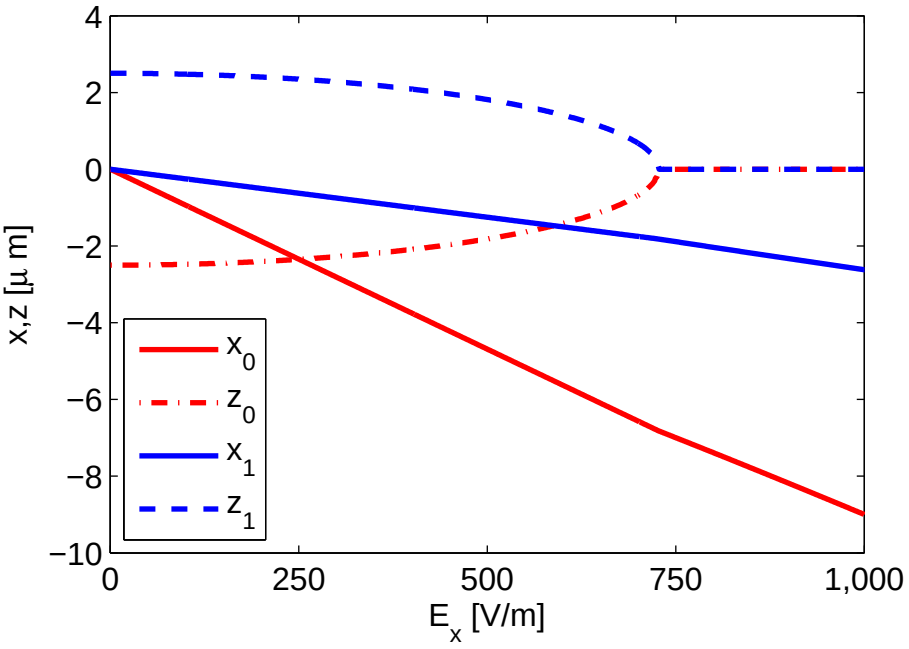

Figure 4.2: Plot of ion positions as a function of a bias field E_x in two dimensions for $\mu = 3$ and $\{\omega_x, \omega_y, \omega_z\} = 2\pi \times \{13, 13, 4\}$ MHz.

experimentally to arrange a particular order in an array of ions containing Mg^+ and Al^+ [Chou 10, Hume 09].

4.2.2 Three Ions

With three ions of masses m_1, m_0 and m_0 respectively, there are two possible ion configurations. These are distinguished by a unique mode spectrum. Specifically, the ion of mass m_1 can be in the center of the array (symmetric configuration) or on the outside (asymmetric configuration). In most experiments on such an ion array, we want to maintain a particular configuration so that we have fixed motional sideband frequencies and amplitudes. Here, again, we consider the ion configuration for a particular mass ratio μ as a function of R_ω.

We imagine beginning with an ion array in a particular axial configuration, then ramping R_ω adiabatically to a higher value and back down to the original value while laser cooling. As the trap conditions change, the ions take on particular arrangements. We characterize these arrangements based on which axial

configurations can be generated when R_ω is returned to the original value. An arrangement is asymmetric or symmetric if it can only return to that particular configuration when relaxed to the axial state. The ions can also form a radial array such that $z_i = 0$ for all i. In this case, neither configuration is deterministically generated as the trap relaxes. Finally, the trap conditions can be such that the ions are not confined.

For the case where the ions start as a symmetric array, the configuration regions are plotted in Fig. 4.2.2. There are several features to note from this diagram. First, it is impossible to make an asymmetric configuration if $\mu < 1$ by only adjusting the frequency ratio. The ion arrangement either transitions directly from symmetric to radial (at $R_\omega = 1$) or from symmetric to not confined, depending on μ. In the latter case, the boundary occurs at $\omega'_x/\omega'_z = 1$ where ω'_x and ω'_z refer to the mode frequencies for a single ion of mass m_0. For $\mu > 1$ there is an asymmetric region near $R_\omega = 1$ where only a triangular arrangement of ions is stable, with the heavier ions to one side. This region can be useful for deterministically reordering the ions. If R_ω is ramped adiabatically to a point in this region then adiabatically relaxed to the original conditions, the ions will assume an asymmetric configuration independent of the initial configuration. We note also that

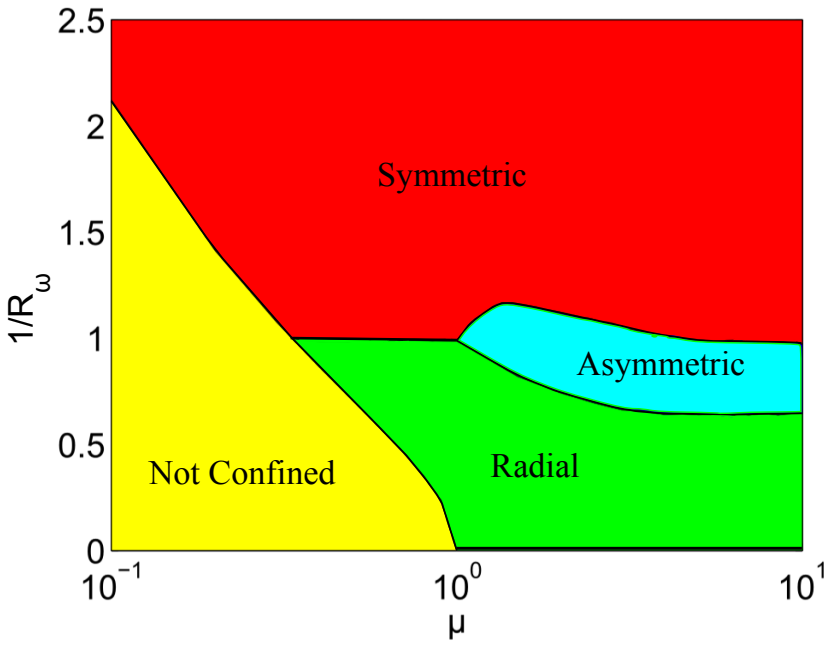

Figure 4.3: Diagram of ion configurations for three ions of masses $\{m_1, m_0, m_1\}$ as a function of μ and $1/R_\omega$, with $E_x = 0$

the lower bound of the graph, at the value $1/R_\omega = 0$, marks the transition from a radial ion array to one that is not confined for $\mu > 1$.

In a similar way, the symmetric 3-ion array can be deterministically produced by adjusting E_x for any value of $\mu \neq 1$. Imagine beginning from an asymmetric configuration with $\mu < 1$ (two heavier ions). As E_x is ramped up, the heavier ions are pushed deeper into the pseudopotential relative to the lighter ones. In the z direction, the barrier that keeps the heavier ions from assuming a position centered about the minimum of the external static potential is the Coulomb repulsion from the lighter ion. As the radial distance between the lighter and heavier ions grows with increasing E_x this potential barrier is reduced until the axial confining fields overcomes it and the ions move towards $z = 0$. With laser cooling, the ions will crystallize into a triangular array that can be adiabatically relaxed to an axial symmetric configuration. The same process will reconfigure three ions with $\mu > 1$.

4.2.3 Higher Ion Numbers

As the number of ions in an array increases the number of ion configurations also increases. For 2 ions of mass m_0 and 2 ions of mass m_1, there are four different ion configurations, for 2 ions of mass m_0 and 3 ions of mass m_1 there are six. In general, it will not be possible to deterministically produce all of these configurations using the techniques we have described. However, some subset of the configurations may be accessible. For example, for the four-ion case with $N_0 = N_1 = 2$, and $\mu = 3$ we find that the configuration $m_1 - m_0 - m_0 - m_1$ can be produced deterministically by raising R_ω. In addition, the configuration $m_0 - m_1 - m_0 - m_1$ can be produced by raising E_x. On the other hand, we have not found a way to produce the configuration $m_0 - m_1 - m_1 - m_0$ deterministically using these techniques. Other techniques, such as introducing field gradients [Splatt 09] may be useful. We note also that any configuration that cannot be produced deterministically can, in principle, be produced probabilistically. Since all configurations are distinguishable by their sideband motional spectrum, any one of them can be produced by randomly rearranging the ions (i.e. by decrystallizing then recooling), checking the sideband spectrum, then repeating the process until the desired configuration is observed.

4.3 Micromotion Measurement and Compensation

Micromotion or motion resulting from the rf trap fields at frequency ω_{rf} and is an unavoidable effect of the ponderomotive trapping potential. In ideal trapping conditions where $\omega_x, \omega_y \gg \omega_z$, such that the ions form a linear string along the rf nodal line, there is still some micromotion due to the finite extent of the ion wavepackets even in the ground state of motion. If, additionally, there are uncompensated radial electric fields, the ions will experience excess micromotion. Relatively high micromotion amplitudes can decrease the efficiency of laser cooling due to the depletion of the cooling resonance into the micromotion FM sidebands. Even if the micromotion amplitudes are very small they can limit the accuracy of precise frequency measurements due to relativistic time dilation [Rosenband 08, Chou 10].

In this section we focus on the effects of excess micromotion and the corresponding time-dilation on the measured frequency in precision spectroscopy. The fractional time dilation shift of a transition at frequency, ν_0, for an ion of mass, m_i, is given by

$$\frac{\Delta\nu}{\nu_0} \simeq -\frac{\langle KE\rangle}{m_i c^2}, \tag{4.13}$$

where $\langle KE\rangle$ is the time-averaged kinetic energy of the ion. The kinetic energy due to excess micromotion is equal to the pseudopotential energy of the ion at the equilibrium position. Using Eq. 4.2 we can write

$$\langle KE\rangle = \frac{a_r}{2m_i}(x_i^2 + y_i^2). \tag{4.14}$$

Suppose there are two ions of mass m_0 and m_1 ($\mu = m_0/m_1$) held in a trap, and consider the time dilation shift on the ion of mass m_1. For a given value for the uncompensated radial bias field, E_x, the equilibrium position will depend on ω_x, ω_z and μ. In Fig. 4.3 we plot the frequency shift from Eq. 4.13 and Eq. 4.14 as a function of $1/R_\omega$ for several values of μ. In this example, we have chosen $E_x = 10$ V/m and $\omega_x/2\pi = 6$ MHz. As long as we are considering small displacements such that $x_i/z_i \ll 1$ for both ions, the results are proportional to E_x^2 for a particular ω_x.

One conclusion we draw from Fig. 4.3 is that the sensitivity of a precision frequency measurement to uncontrolled radial electric fields depends on the mass ratio in a two-species ion array. The external electric field causes a tilt of the ion array with respect to the trap axis, which results in an additional radial

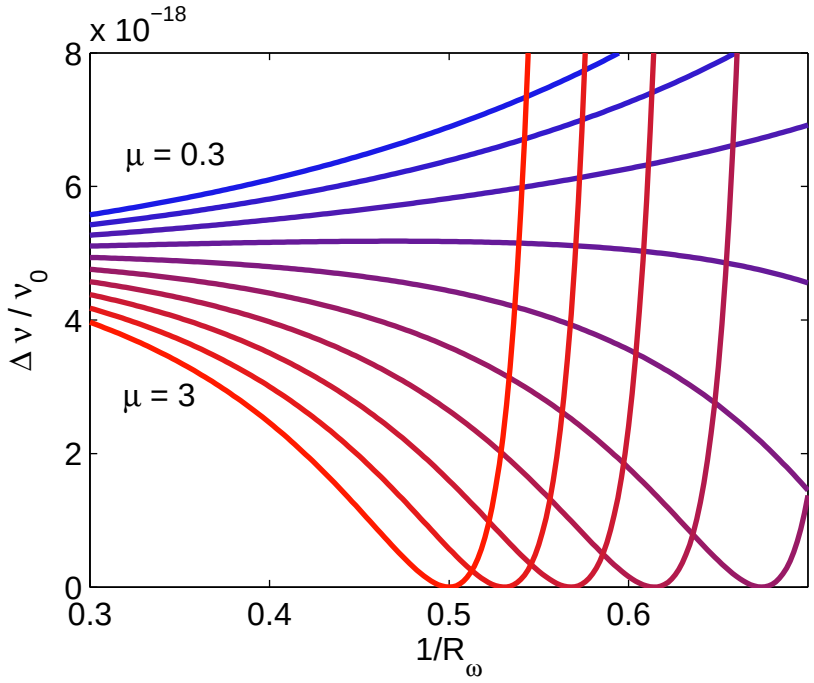

Figure 4.4: Time dilation shifts due to excess micromotion for a two ion array as a function of $1/R_\omega = \omega_x/\omega_z$, for several values of $\mu = m_0/m_1$

component of the Coulomb repulsion between the two ions. Depending on the mass ratio, this can enhance or diminish the effect of the external field on the position of the primary ion. In general, for the purpose of minimizing micromotion due to stray electric fields, it is preferable to use an ancillary ion that is heavier.

For certain conditions, the micromotion amplitude is nulled for the lighter-mass ion independent of E_x. This is the condition where E_x is equal to the x-component of the field from the heavier ion at the position $\{x_1, z_1\}$ and it occurs precisely when $\omega_x = \omega_z$ for the single, heavier ion. This electric-field-insensitive point may allow for passive nulling of excess micromotion for high accuracy measurements. Note, however, that these conditions cannot be simultaneously obtained for both the x and y directions because this implies a degeneracy in motional frequencies, which is incompatible with efficient cooling. A small difference in the radial motional frequencies can allow for near-perfect nulling of excess micromotion in the two radial directions while maintaining cooling efficiency.

Excess micromotion can also be actively compensated by detecting it and adjusting voltages on the

trap electrodes to suppress it. A direct method for doing this is by applying a laser beam at a frequency $\omega_0 \pm \omega_{RF}$, where ω_0 is the frequency of an optical resonance, and looking for fluorescence, or coherent Rabi flopping. Excess micromotion is minimized in the direction of the laser beam k-vector when the sideband at ω_{RF} is minimized. To do this in both radial directions, two nearly orthogonal laser beams in the x-y plane are required. However, stray electric fields causing excess micromotion also alter the motional mode amplitudes and directions in two-species ion arrays. The use of these effects for micromotion compensation has been explored previously [Barrett 03]. As a simple example, consider two ions of different mass aligned perfectly on the axis of a linear trap and probed with a laser beam directed along the trap axis. In this condition, the radial motion sidebands at frequencies $\omega_0 \pm \omega^{(\alpha)}$, with α referring to any mode in the x or y direction, will be absent. However, a bias electric field will displace the two different-mass ions into the pseudopotential, causing excess micromotion and altering the normal mode directions. As a result, the secular modes that are purely radial in the ideal configuration will have some axial component, which can be detected with the axial beams. To the extent that the probe beam is purely axial, the excess micromotion can be nulled by nulling these sidebands, which aligns the ion array along the trap axis. In the next section we will consider further the effect of bias fields on the amplitude and direction of secular motion in the context of sympathetic cooling.

4.4 Sympathetic Cooling

The precise manipulation of ion internal and external states requires low temperature. High motional temperature can cause broadening of or FM sidebands on atomic resonance, as well as shifts of the resonance frequency due to time dilation. In addition, the ion temperature affects the rate and coherence of Rabi flopping due to the Debye-Waller effect [Wineland 98]. For these reasons, in most experiments on individual trapped ions, the first step in the experimental process is Doppler laser cooling. This section addresses Doppler cooling efficiency in two-species ion arrays.

Sympathetic laser cooling using two ion species has been explored in the context of quantum information processing [Kielpinski 00, Barrett 03]. In this technique one (cooling) ion species acts as a refrigerant for the other (primary) species, with both species stored in the same trap and coupling through collective modes

of motion. There are several advantages of sympathetic cooling. First it allows laser cooling of ion species that cannot be directly cooled, which includes most atomic ions, molecular ions, and ions with no atomic structure such as a proton. Second, the spectroscopic isolation of the primary system from the cooling laser means that the laser cooling leaves the primary system largely undisturbed. Experiments where the ions must be cooled between or during coherent operations become possible. One potential problem with this idea is that there are N_0 ions scattering photons rather than N ($N = N_0 + N_1$). This means that there is less cooling power for the $3N$ motional modes compared to a single-species ion array.

The rate that energy is extracted from the ion system during laser cooling can limit both the experimental cycle time and the minimum temperature. For example, Doppler cooling times are often on the order of 1 ms, comparable with other rate-limiting steps such as fluorescence detection. The minimum temperature achievable is affected by the cooling rate compared to the external heating rate. Here, we ignore recoil heating and parameterize the laser cooling rate for a particular mode in terms of the damping time $\tau_d^{(\alpha)}$. The cooling rate is given by $\dot{n}^{(\alpha)} = -n^{(\alpha)}/\tau_d^{(\alpha)} + \dot{n}_{\text{ext}}$ where we assume a rate of external heating of $\dot{n}_{\text{ext}}$. The minimum temperature occurs when the heating rate and cooling rate are equal, yielding $n_{\text{min}}^{(\alpha)} = \tau_d^{(\alpha)}\dot{n}_{\text{ext}}$. The assumption that we can ignore the effects of recoil heating is justified to the extent that n_{min}^{α} is greater than the limit due to recoil heating, n_D. In ideal circumstances, $n_D \simeq \Gamma/2$, where Γ is the linewidth of the resonance used for cooling.

Damping times for Doppler cooling depend on a number of experimental parameters including the intensity, geometry and detuning of the cooling laser beams. Theoretical cooling rates have been derived for a range of conditions [Wineland 79, Itano 82]. In the following analysis we focus on the effect of ion mode amplitudes. Suppose a single cooling ion is trapped with another ion of a different species. Only the cooling ion motional amplitudes are relevant for the cooling rate. If the temperature is sufficiently low that the Doppler broadening of the cooling resonance is insignificant, $\tau_d^{(\alpha)} \propto (1/\eta_i^{(\alpha)})^2$ where $\eta_i^{(\alpha)}$ is the Lamb-Dicke parameter of ion i and mode α. If $\mathbf{r_i}^{(\alpha)}$ is the ground-state motional amplitudes for the cooling ion, and $\mathbf{k}$ is the cooling laser k-vector then $\eta_i^{(\alpha)} = \mathbf{k} \cdot \mathbf{r_i}^{(\alpha)}$.

The mode amplitudes represented by $\mathbf{r_i}^{(\alpha)}$ are determined based on Eq. 4.9, and Eq. 4.12. A pair of ions of unequal mass held in the same linear trap have unequal motional amplitudes for each mode. In

particular, the radial modes, affected by the mass-dependent pseudopotential, often exhibit large imbalances in mode amplitudes. As an example, we consider a $^{9}Be^{+}$-$^{27}Al^{+}$ array ($\mu = 3$). We take trap conditions such that a single Be^{+} has normal mode frequencies $\{\omega_x, \omega_y, \omega_z\} = 2\pi \times \{13, 14, 4\}$. The minimum mode amplitude for a single trapped Be^{+} is 6.3 nm. With the Be^{+} and Al^{+} in those trap conditions, the radial out-of-phase modes have amplitudes 0.3 and 0.4 nm for the x and y directions respectively. For typical laser geometries, the cooling rate of the lowest amplitude mode is more than 300 times lower than for a single Be^{+}. A mode with a small amplitude for the cooling ion will have a relatively large amplitude for the primary ion as shown in Eq. 4.11. The small amplitude for cooling can limit the minimum temperature for that mode and the large amplitude for the primary ion can make the elevated temperature a significant experimental issue. Furthermore, while external heating of an equal-amplitude, out-of-phase mode (i.e. with two equal mass ions) will be strongly suppressed [Kielpinski 00], modes with unbalanced amplitudes will heat under spatially uniform fluctuating electric fields. These factors together make unbalanced motional amplitudes problematic for effective sympathetic cooling.

The problematic mode amplitudes can often be enhanced significantly by adjusting trap parameters.

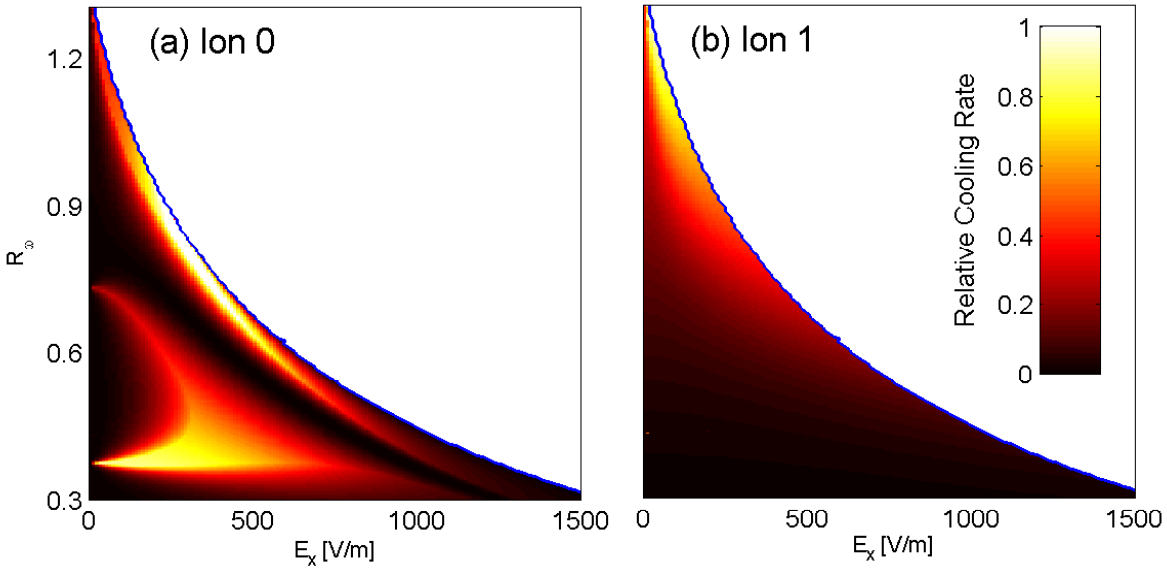

Figure 4.5: Relative cooling rates for a two ion array with $\mu = 3$ as a function of R_ω and E_x when: (a) Directly cooling the lighter ion. (b) Directly cooling the heavier ion.

We illustrate this in Fig. 4.4 (a) by plotting $|\mathbf{r}_1^{(\alpha_{\min})}|^2$ vs. R_ω and E_x for the $\mu = 3$ example, where $\alpha_{\min}$ is the mode with the lowest amplitude at each set of trap parameters. In most situations, this is the mode that will limit the rate of Doppler cooling, and, in the presence of external heating, limit the minimum temperature. Note that R_ω in these plots refers the ω_x/ω_z for the heavier ion (i = 0), and $|\mathbf{r}_i^{(\alpha_{\min})}|^2$ is normalized to the highest value in the respective plots. In Fig. 4.4 (b) we plot $|\mathbf{r}_0^{(\alpha_{\min})}|^2$ for the same parameters. The blue bounding line represents the threshold between an axial and radial array. For the case of directly cooling the lighter ion, the limiting rate can be significantly enhanced by adjusting the confinement parameters to a specific region. In an experiment, higher cooling efficiency and lower temperature can be reached by applying the proper endcap and radial bias voltages, then adiabatically relaxing the trap back to an axial array. An enhancement in mode amplitudes can also be made in the case of directly cooling the heavier ion, although the effect is not as pronounced and only occurs in one region close to the threshold for a radial array.

The qualitative features of Fig. 4.4 are very similar for other values of μ. In addition, the cooling rate for higher numbers of ions can be enhanced with this technique. As with two ions, the specific values for R_ω and E_x that are optimal depend on μ, and the details of the ion configuration. Other factors that affect the rate of cooling have been omitted from this discussion. Since $\eta_i^{(\alpha)} = \mathbf{k} \cdot \mathbf{r}_i^{(\alpha)}$, it is not only the absolute value $|\mathbf{r}_i^{(\alpha)}|$ that is important, but also its direction with respect to the cooling lasers. As the ions move off axis under the application of E_x, the mode vectors change direction. If $\mathbf{k} \cdot \mathbf{r_i} = 0$ for a particular mode, that mode will not be cooled and instead will heat due to recoil. Another important consideration is the excess micromotion the ions experience as they are pushed off axis. If the micromotion has a component in the direction of $\mathbf{k}$ it can reduce cooling efficiency and, in some cases, cause heating. These issues can generally be managed with the proper choice of trap conditions and cooling laser beam geometry.

4.5 Conclusion

We have examined several ways in which the dynamics of two-species ion arrays can affect experiments on trapped ions. In several aspects, including equilibrium positions, micromotion compensation, and laser cooling, these systems behave in a qualitatively different way than a single-species ion array. This both presents experimental challenges and provides methods for overcoming them. In addition to the benefits

of sympathetic cooling and indirect state detection, the behavior of a two-species ion array allows for new methods to measure and compensate excess micromotion. The examples presented mainly focused on two ions of different species, but using the same model discussed in Sec. 4.1, the results can be extended to larger ion numbers. The techniques and considerations discussed here apply to a number of experiments already performed, including the experiments of this thesis. Given the interest in two-species ion arrays for spectroscopy and quantum information processing, these considerations may also be helpful in future experiments.

Chapter 5

Quantum Nondemolition Measurements of Trapped Ions

Reliable state detection plays a central role in many quantum physics experiments including quantum-limited metrology and quantum information processing. In practice, detection fidelity is limited by state perturbations and noise during the measurement process. For example, for a single trapped ion, the discrimination between internal states presents a number of technical challenges. The excitation of a single atom by an optical or rf photon adds only a small amount of energy to the system ($\Delta E \simeq 10^{-25}$ to 10^{-19} J), and achieving high enough signal-to-noise ratio (SNR) requires a huge amplification. At the same time, it is important to reduce the time interval required for detection both for atomic clock experiments (to maximize clock stability) and for quantum computation (to reduce error correction overhead [DiVincenzo 01]).

These constraints together put a high performance requirement on any measurement scheme[1] . A couple of methods have been proposed and developed to detect the state of individual ions. For example, the Fock-state of cyclotron motion for a single electron in a Penning trap has been detected electronically by observing the spin-dependent current induced on a trap electrode [Peil 99]. However, the charge-to-mass ratio of the electron is thousands of times larger than for atomic ions. The higher mass and consequently lower motional frequencies lead to smaller currents that are difficult to detect in a reasonable integration time with sensitive electronics. The standard method for detecting the internal state of a single trapped ion, proposed by Hans Dehmelt [Dehmelt 75] and first implemented concurrently in three labs [Nagourney 86, Bergquist 86, Sauter 86], is state-dependent resonance fluorescence. One feature that ties this method together with the

[1] As a practical matter, it is also desirable to keep the ion trapped for subsequent experiments and keep its ionization state unchanged. This requirement eliminates possibilities such as using state-dependent photoionization and detecting the emitted electron with a microchannel plate.

observation of spin-dependent current is that they are both examples of quantum nondemolition (QND) measurements. The QND nature of these schemes allows for the huge amplification factors necessary to detect a single atom's excitation.

The outline of this chapter is as follows: Section 5.1 introduces the idea of a QND measurement, which will be the basis for all of the state detection protocols discussed. In our experiments, information is ultimately transferred from the ions to the measurement apparatus via resonantly scattered photons that impinge on a photon counter. Section 5.2.1 considers the Bayesian analysis of photon counts to determine the result of a measurement. This analysis is applied in Sec. 5.2.2 to measurements of Be^+ via resonance fluorescence. In Sec. 5.2.3, I present a method for indirectly performing adaptive QND measurements on a trapped ion by storing it with another ion of a different species. The measurement performance is characterized experimentally and the ideas are extended to the simultaneous, indirect state detection of multiple ion qubits. Finally, I consider alternative measurement schemes (Sec. 5.3.1) that may be more suitable for different atomic systems. These ideas are relevant to measurements that generate entanglement (Sec. 5.3.2) as well as a measurement protocol based on time-resolved photon counting (Sec. 5.3.3).

5.1 General QND measurements

The term nondemolition, loosely speaking, refers to the preservation of a projected eigenstate during measurement of a quantum system. To be clear, it does not concern the projection of the quantum system into an eigenstate of the measurement operator, which is an unavoidable consequence of the measurement postulate in quantum mechanics (Ch. 1). The idea of a QND measurement was originally developed in the context of gravitational wave detection [Caves 80], in which the measurement must distinguish harmonic motion at the quantum scale. Standard measurement schemes tend to perturb the system being measured, erasing the delicate information contained in the quantum state. The motivation behind a QND measurement is to construct a measurement scheme that does not perturb the observable being measured, so that the scheme can be repeated with the same outcome. As an imperfect QND measurement is repeated or applied continuously, the measurement error probability due to classical noise decreases, while the probability of state perturbation increases. This implies a minimum error probability at a particular measurement duration. The

measurement duration is a separate parameter to characterize the measurement efficiency.

The principles of a QND measurement can be stated succinctly in terms of general quantum mechanical operators. We consider a quantum system, $\mathcal{S}$, measured by another quantum system (meter), $\mathcal{M}$. We would like to measure an observable $\hat{O}_S$ by coupling system $\mathcal{S}$ to system $\mathcal{M}$. The interaction between the systems is described by the operator $\hat{H}_{SM}$, and we assume there is an observable of M, $\hat{O}_M$, that is directly measurable. The first condition,

$$[\hat{O}_M, \hat{H}_{SM}] \neq 0, \tag{5.1}$$

ensures that the interaction Hamiltonian $\hat{H}_{SM}$ indeed affects the state of the meter. However, this is not enough because the meter must evolve dependent on the state of the measured system. Therefore,

$$\hat{H}_{SM} \neq \hat{H}_S \otimes \hat{H}_M, \tag{5.2}$$

which is the condition that the interaction Hamiltonian is not separable into independent actions on $\mathcal{S}$ and $\mathcal{M}$. The final condition,

$$[\hat{O}_S, \hat{H}] = 0, \tag{5.3}$$

where $\hat{H} = \hat{H}_{SM} + \hat{H}_0$ and $\hat{H}_0$ describes the free evolution of the system, ensures that the projected state of system S remains stable in time. The details of these conditions and examples of their application can be found in two reviews of the subject [Caves 80, Braginsky 96].

No measurement of a real quantum mechanical system perfectly meets the condition of Eq. 5.3. For example, when detecting the state of a quantum harmonic oscillator, the surrounding environment will have finite temperature leading to a finite probability of thermal excitation during measurement. Similarly, the electronic states of atomic systems can decay, whether due to their finite natural lifetime or to weak off-resonant coupling to applied fields. The extent to which a QND measurement meets the criteria of Eq. 5.1 and 5.3 has been quantified formally in different contexts [Ralph 06, Holland 90]. Here, the performance of an imperfect quantum nondemolition measurement is quantified primarily in terms of a single parameter - the minimum error probability that can be achieved through repetitive measurements. If the conditions stated above are met in a meaningful way, an imperfect QND measurement can be repeated to decrease the probability of measurement error. As the repeated measurement cycles continue, however, the proba-

bility of perturbing the state increases. At a certain average measurement duration (or a average number of measurement cycles) these two counteracting effects give rise to a certain minimum error probability. The measurement duration itself is a separate, but often related, parameter describing the measurement performance. I explore both of these performance measures in the next sections.

5.2 Experimental QND Measurements

All of the detection protocols used in our experiments can be considered as a QND measurement, and in this section I discuss the measurement strategies in these terms. All of the information we extract from system $\mathcal{S}$ about the ion electronic states, S_i, comes in the form of photon counts from a photomultiplier tube (PMT). This is true whether we are directly measuring the ions via resonance fluorescence as in Sec. 5.2.2, or are indirectly inferring their state after interacting with other ions held in the same trap as in Sec. 5.2.3. To provide a basis for these particular types of measurement I first describe the statistical analysis of photon histograms.

5.2.1 Bayesian Analysis of Photon Histograms

The accurate evaluation of measurement outcomes depends on our previous knowledge of the photon histograms corresponding to the N_S possible ion states, $\{S_1, S_2, \ldots, S_{N_S}\}$. The observable measured is

$$\hat{O}_S = \sum_{i=1}^{N_S} \lambda_i |S_i\rangle\langle S_i|. \tag{5.4}$$

In most experiments we think of the ion states in terms of the electronic basis, with each of the N ions occupying either qubit state $|\downarrow\rangle$ or $|\uparrow\rangle$ so that $i \in [1,\ 2^N]$. However, in the case of direct fluorescence measurements we assume the ions are equally illuminated by the detection beam and equally imaged onto the PMT so that they cannot be distinguished. The observable in this case is the number of fluorescing ions, which is represented in $\hat{O}_S$ by assigning all states with equal number of ions in $|\downarrow\rangle$ the same eigenvalue.

If $P(p|S_i)$ is the probability of observing p photons given the state S_i, then Bayes' rule,

$$P(S_i|p) = \frac{P(p|S_i)}{\sum_k P(p|S_k)}, \tag{5.5}$$

gives the probability of the ion state being S_i given p photon counts. The measurement outcome is $S_{i'}$, for which $P(p|S_{i'})$ is greatest, and the probability of error is given by

$$P_{\rm err}(p) = 1 - P(S_{i'}|p). \tag{5.6}$$

The mean error probability can be written as

$$\overline{P}_{\rm err} = \sum_{p=0}^{\infty} P_{\rm err}(p) \left[\sum_{k=1}^{N_S} P_0(S_k) P(p|S_k) \right], \tag{5.7}$$

where $P_0(S_k)$ is the prior probability of state S_k and the factor in brackets gives the overall probability of observing p photons. The prior probabilities are usually assumed to be $1/N_S$ for all states. Substituting this and Eq. 5.6 and 5.5 into Eq. 5.7 we can write

$$\overline{P}_{\rm err} = \frac{1}{N_s} \sum_{p=0}^{\infty} \sum_{k \neq i'} P(p|S_k), \tag{5.8}$$

remembering that the value of i' depends on the value of p. Although this expression involves an infinite sum, as a practical matter it can be truncated at a reasonable maximum number of photons, ${p_{\rm max}}^2$.

The analysis above can be extended to indirect measurements of ion states. In indirect state measurements, information is transferred from the ions of system $\mathcal{S}$ to the ions of system $\mathcal{M}$ via a collective mode of motion, then system $\mathcal{M}$ is measured directly. With repeated cycles of this process, the outcome of a measurement is based on a series of photon counts, rather than the single number p. If C represents the number of measurement cycles, then the series of photon counts is represented by $\{p\} = \{p_1, p_2, \ldots, p_C\}$. Each number of photon counts carries information about the same state. Given a particular state, the probability of observing the whole set $\{p\}$ is

$$P(\{p\}|S_i) = \prod_{j=1}^{C} P(p_j|S_i). \tag{5.9}$$

Bayes' rule (Eq. 5.5) applied to the probability distributions of Eq. 5.9 provides the measurement outcome, $S_{i'}$ and the error probability is given by,

$$P_{\rm err}(\{p\}) = 1 - P(S_{i'}|\{p\}). \tag{5.10}$$

[2] In the experiments of this chapter a single fluorescing ion might produce an average of $\overline{p} = 10$ photons with a 1-σ spread of $\sqrt{\overline{p}}$ in the measurement duration so $p_{\rm max} \sim 30$ is a safe assumption. Depending on the desired accuracy of the calculation, one way to scale the cutoff with higher ion numbers N is $p_{\rm max} = N\overline{p} + X\sqrt{N\overline{p}}$, where X is the number of standard deviations required for the desired accuracy

All of the expressions above (Eq. 5.5- Eq. 5.7) can be applied equivalently to multiple measurements with the substitution $p \rightarrow \{p\}$. The mean error probability for a particular number of cycles is given by averaging over all possible sets $\{p\}$. As with the sum over p, above, there are an infinite number of terms in the series, but the series can be terminated using a reasonable maximum photon number. In this case, the number of terms summed is $p_{\max}^{C}$, leading to,

$$\overline{P}_{\text{err}} = \frac{1}{N_s} \sum_{l=1}^{p_{\max}^{C}} \sum_{k \neq i'} P(\{p\}_l | S_k). \tag{5.11}$$

Evaluating Eq. 5.11 can become computationally intensive for a relatively small number of ions and measurement cycles. An approximation to the mean error probability can be determined by a Monte-Carlo simulation. In this method, the set of conditional probabilities, $\{P(p|S_i) \,|\, i \in [1, N_S]\}$ are taken as input based on separate calculations (see, for example, Sec. 5.3.1). Each state in the set $\{S_1, S_2, ..., S_{N_S}\}$ acts as the input state to a certain number of trials of the Monte Carlo simulation. If S_1 is the input state then a series of C photon counts are randomly chosen based on the known distribution $P(p|S_1)$. The error probability is calculated based on Eq. 5.9 and Eq. 5.10 with $S_i, S_{i'} \rightarrow S_1$, and the mean error rate $\{\overline{P}_{\text{err}}(S_i)\}$ is the average of these individual error probabilities. Alternatively (and less efficiently) the most likely state $S_{i'}$ can be determined based on the set of probabilities $P(\{p\}|S_i)$. If $S_{i'} \neq S_1$ an error has occurred and the estimated mean error rate is the ratio of errors to trials. Depending on the accuracy desired, a certain number of trials are performed with each of the possible input states, yielding the set of mean error rates, $\{\overline{P}_{\text{err}}(S_i)\}$. The overall mean error rate is given by $\overline{P}_{\text{err}} = \sum_i P_0(S_i)\overline{P}_{\text{err}}(S_i)$. Known rates of spontaneous decay (or off-resonant repumping) can be applied to system $\mathcal{S}$ in the simulation to obtain a reasonable estimate for the minimum error probability. This numerical method has been used in several simulations for the different scenarios described below.

5.2.2 Be^+ Resonance Fluorescence as a QND measurement

In the experiments described in this chapter we use $^9Be^+$ as a sympathetic cooling ion, and, in the language QND measurements, as a quantum meter. Before discussing those experiments it is useful to consider the direct measurement of Be^+ through resonance fluorescence as a QND measurement. Here,

the primary system, $\mathcal{S}$, is the Be^+ atomic system with each Be^+ ion considered as a qubit. The meter system, $\mathcal{M}$, is not as well characterized, but consists of the set of electromagnetic modes connecting the ion to the PMT. The Be^+ qubit is comprised of two hyperfine Zeeman sublevels of the $^2S_{1/2}$ ground state, $|\downarrow\rangle_{Be} \equiv |F = 2, m_F = -2\rangle$ and $|\uparrow\rangle_{Be} \equiv |F = 1, m_F = -1\rangle$. If we define $|P\rangle_{Be} \equiv |^2P_{\frac{3}{2}}; F = 3, m_F = -3\rangle$, the states $|\downarrow\rangle_{Be}$ and $|\uparrow\rangle_{Be}$ are distinguished by applying a σ^- polarized laser pulse of duration t_D tuned to resonance for the $|\downarrow\rangle_{Be} \rightarrow |P\rangle_{Be}$ cycling transition [Monroe 95]. For a given photon collection efficiency, ϵ, and a given background count rate, γ_{BG}, the measurement fidelity for this system is limited by off-resonant repumping of $|\uparrow\rangle_{Be}$ to $|\downarrow\rangle_{Be}$. A detailed analysis of this process that considers electron shelving in different Zeeman sublevels is presented in [Langer 06], following [Acton 06]. For the repumping of $|\uparrow\rangle_{Be}$ to $|\downarrow\rangle_{Be}$ here, a simple exponentially decaying model is sufficient, for which the probability of having been repumped after detection interval, t_D is given by $1 - e^{-\gamma_r t_D}$. In terms of the saturation parameter, s_0, the laser detuning $\delta = \omega_{HF}$, and the $^2P_{3/2}$ linewidth, Γ, the repump rate is given by

$$\gamma_r = C_\downarrow \frac{\Gamma}{2} \frac{s_0}{1 + s_0 + (2\delta/\Gamma)^2}, \tag{5.12}$$

where $C_\downarrow$ is the coupling coefficient between the $|^2P_{\frac{3}{2}}; F = 3, m_F = -2\rangle$ and the hyperfine level $F = 2$. We make the realistic assumption that scattering from $|F = 2, m_F = -1\rangle$ to $|\downarrow\rangle_{Be}$ is fast compared to $1/\gamma_r$ and t_D.

The parameters, γ_r, γ_{BG} and $\gamma_c \equiv \epsilon\Gamma$, are sufficient for calculating photon histograms for any detection time. Fluorescence histograms for 0 to 4 fluorescing Be^+ ions based on realistic experimental parameters, are displayed in Fig. 5.1(a). For the case of all ions in state $|\uparrow\rangle_{Be}$ the histogram represents the low level of background counts as well as the long tail corresponding to ions fluorescing after being repumped. With larger numbers of ions the overlap between adjacent ion states becomes more significant, both because the repump probability increases and because the neighboring Poisson distributions have greater overlap. In general, this favors longer detection times in order to further disperse the Poisson means (at the expense of larger repump probability). Here, we assume that all of the ions are equally illuminated by the detection laser and are imaged with equal efficiency so that, if there are N_{Be} ions, there are $N_{Be}+1$ states to distinguish. The sets of photon histograms give the average measurement fidelity for distinguishing the states of using

Eq. 5.7. The simulated measurement error for $N_{\mathrm{Be}} \in [1, 4]$ as a function of t_D is shown in Fig. 5.1(b), with the minimum error for 1 Be^+ occurring at 200 μs while the minimum error probability for multiple Be^+ is approximately 500 μs.

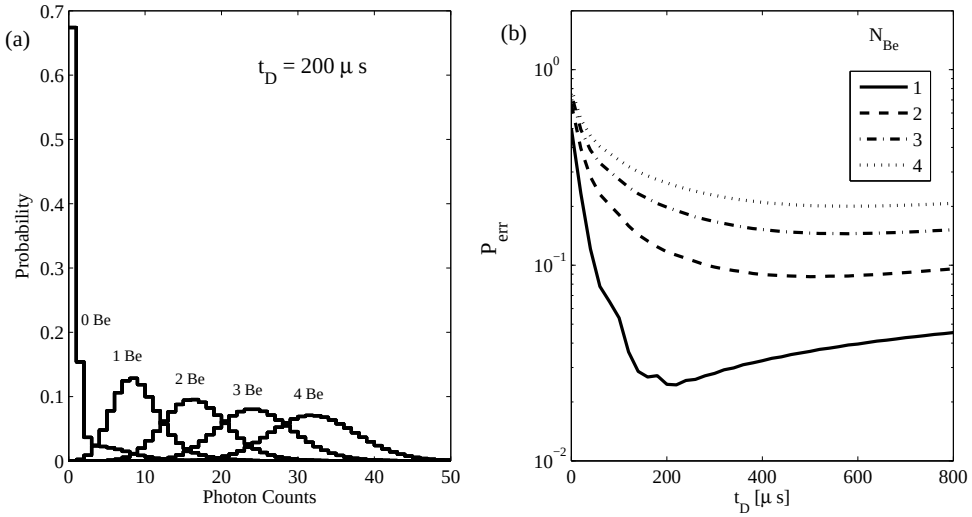

Figure 5.1: (a) Histograms of photon counts calculated from realistic experimental parameters including background counts and repumping from $|\uparrow\rangle_{\mathrm{Be}}$ to $|\downarrow\rangle_{\mathrm{Be}}$. (b) Mean measurement infidelity as a function of detection time t_D for different numbers of ions. The small wiggles are due to finite sampling.

Strictly speaking, this measurement does not satisfy the condition 5.3. To begin with, the interaction of the atom with the light field promotes $|\downarrow\rangle_{\mathrm{Be}}$ to $|P\rangle_{\mathrm{Be}}$ so that $\hat{H}_{SM}$ contains terms proportional to $|P\rangle_{\mathrm{Be}}\langle\downarrow|_{\mathrm{Be}}$, which does not commute with $\hat{O}_S = |\downarrow\rangle_{\mathrm{Be}}\langle\downarrow|_{\mathrm{Be}}$. This can be dealt with formally by identifying a scattering event as a two photon process (as in [Wineland 79]), which, to the extent that the polarization is pure $\hat{\sigma}^-$, leaves the internal state unchanged. Equivalently, we can identify the observable as $\hat{O}_S = |\downarrow\rangle_{\mathrm{Be}}\langle\downarrow|_{\mathrm{Be}} + |P\rangle_{\mathrm{Be}}\langle P|_{\mathrm{Be}}$ so that 5.3 is satisfied. An imperfection that cannot be formally avoided is off-resonant repumping

of $|\uparrow\rangle_{\mathrm{Be}}$, which introduces to $\hat{H}_{SM}$ terms proportional to $|\downarrow\rangle_{\mathrm{Be}}\langle\uparrow|_{\mathrm{Be}}$. However, every photon scattered is a complete measurement of the electronic state in that it results in the projection of the state into $|\downarrow\rangle_{\mathrm{Be}}$ or $|\uparrow\rangle_{\mathrm{Be}}$, and in principle can be counted. Since $\gamma_r \ll \Gamma$, Eq. 5.3 is a good approximation and since $\gamma_r/\gamma_c < 1$, Eq. 5.1 is satisfied in a meaningful way.

5.2.3 Qubit Detection through Repetitive QND Measurements

Direct detection of an ion qubit through resonance fluorescence requires a relatively strong interaction of the ion to the environment, since only a small fraction of the photons scattered are detected. One way to isolate a qubit further from the environment is to couple the primary quantum system, $\mathcal{S}$, to a controlled quantum meter, $\mathcal{M}$, which is then directly detected [DiVincenzo 01, Haroche 06, Schaetz 05, Schmidt 05, Gleyzes 07]. The measurement interaction, H_{SM}, is now a controlled coherent process between two quantum systems, which is inherently well insulated from the environment. Furthermore, the interaction between the meter system and the measuring apparatus need not involve the primary system at all. These conditions can help in satisfying Eq. 5.3. An important feature of a QND measurement is its repeatability [Meunier 06, Gleyzes 07, Lupascu 07], which allows for high fidelity state detection in the presence of noise. The repetitive transfer of information from $\mathcal{S}$ to $\mathcal{M}$ followed by detection of the meter state provides a natural mechanism for real-time measurement feedback, which can further enhance detection efficiency [Armen 02, Cook 07].

We now apply the ideas of QND measurements to high-fidelity indirect measurements of one and two-qubit systems in an ion trap. In these experiments, one or two $^{27}Al^{+}$ ions form the primary quantum system $\mathcal{S}$ and one or two Be^{+} ions make up $\mathcal{M}$. The ions are stored together in a linear, rf Paul trap and they are interact through their mutual Coulomb repulsion. Both ion species can be considered as qubits, each having an auxillary internal state used in the detection procedure (Fig. 5.2). In Al^{+}, the qubit states consist of the $|^1\mathrm{S}_0;\mathrm{F}=\frac{5}{2},\mathrm{m_F}=\frac{5}{2}\rangle \equiv |\downarrow\rangle_{\mathrm{Al}}$ ground state and the metastable $|^3\mathrm{P}_0;\mathrm{F}=\frac{5}{2},\mathrm{m_F}=\frac{5}{2}\rangle \equiv |\uparrow\rangle_{\mathrm{Al}}$ optically excited state. Motional sideband transitions through the $|^3\mathrm{P}_1;\mathrm{F}=\frac{7}{2},\mathrm{m_F}=\frac{7}{2}\rangle \equiv |^3\mathrm{P}_1\rangle_{\mathrm{Al}}$ auxillary state mediate the measurement interaction, transferring information from $\mathcal{S}$ to $\mathcal{M}$ as described below.

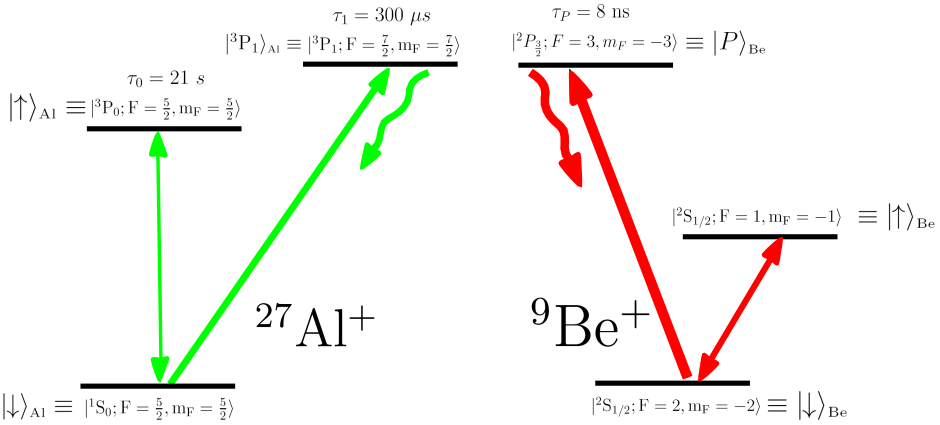

Figure 5.2: Relevant energy levels in $^{27}\mathrm{Al}^+$ and $^9\mathrm{Be}^+$. The states $|\downarrow\rangle_{\mathrm{Al}}$ and $|\uparrow\rangle_{\mathrm{Al}}$ form the qubit to be measured. The $m_F = \frac{7}{2}$ Zeeman sublevel of the $^3\mathrm{P}_1$ state forms a closed transition with $|\downarrow\rangle_{\mathrm{Al}}$. The widely separated excited state lifetimes in Al^+, 21 s and 300 μs, allow for many repetitions of the detection procedure in a single experiment. The qubit states in Be^+ are distinguished by state-dependent resonance fluorescence [Monroe 95].

5.2.3.1 Be-Al:

The simplest ion system to consider for repetitive QND measurements consists of two ions, one ion as the primary system and one as the meter. With Al^+ in an unknown qubit state, the measurement procedure begins by laser-cooling the two ions to the motional ground state [Barrett 03] and initializing Be^+ to $|\downarrow\rangle_{\rm Be}$ [Monroe 95]. Then, a series of laser pulses transfers the information in the Al^+ system first to a shared motional state then to the Be^+ internal state. The Be^+ ion is detected by resonance fluorescence as described in Sec. 5.2.2. The individual steps and their durations are:

(1) Doppler cooling all modes ($\simeq 600\ \mu s$)

(2) Raman cooling axial modes to ground state (1 ms)

(3) Be^+ preparation to the state $|\downarrow\rangle_{\rm Be}$ ($1\ \mu s$)

(4) State transfer between Al^+ and Be^+ ($\simeq 25\ \mu s$)

(5) Be^+ state detection ($200\ \mu s$).

In step (4) we couple the ions through the axial in-phase mode ($\omega_m = 2\pi \times 2.62$ MHz) [Schmidt 05]. Here, we denote Fock states of motion as $|n\rangle_m$. First, a π-pulse on the $|\downarrow\rangle_{\rm Al}|0\rangle_m \rightarrow |^3{\rm P}_1\rangle_{\rm Al}|1\rangle_{\rm m}$ sideband transition inserts a quantum of motion into the mode dependent on the ion being in the $|\downarrow\rangle_{\rm Al}$ state. The information in the collective motion is then transferred to the internal state of Be^+ using a π-pulse on the $|\downarrow\rangle_{\rm Be}|1\rangle_m \rightarrow |\uparrow\rangle_{\rm Be}|0\rangle_m$ transition. This sequence implements an entangling operation,

$$\big(\alpha|\downarrow\rangle_{\rm Al} + \beta|\uparrow\rangle_{\rm Al}\big)|\downarrow\rangle_{\rm Be} \rightarrow \alpha|^3{\rm P}_1\rangle_{\rm Al}|\uparrow\rangle_{\rm Be} + \beta|\uparrow\rangle_{\rm Al}|\downarrow\rangle_{\rm Be}. \tag{5.13}$$

After measurement, the Al^+ ion is projected into $|\uparrow\rangle_{\rm Al}$ with probability $|\beta|^2$. Because the $^1{\rm S}_0$ to $^3{\rm P}_1$ transition is closed, the Al^+ ion is projected into the manifold of the $|\downarrow\rangle_{\rm Al}$ and $|^3{\rm P}_1\rangle_{\rm Al}$ states with probability $|\alpha|^2$. Although temporary optical excitation into $|^3{\rm P}_1\rangle_{\rm Al}$ represents a departure from the strict definition of a QND measurement, we can formally address this (as in Sec. 5.2.2) by defining the state $|\downarrow\rangle_{\rm Al}$ to include the eigenspace spanned by the $^1{\rm S}_0$ and $^3{\rm P}_1$ states. Spontaneous emission from the $^3{\rm P}_1$ state ($\tau_1 \simeq 300\ \mu s$)

effectively re-prepares Al^+ back to $|\downarrow\rangle_{Al}$ with probability greater than 99 % before another detection cycle is implemented.

Imperfect cooling and transfer pulses give rise to a single-cycle detection error of approximately 15 %. However, the fidelity can be improved by repeating the procedure. For the jth cycle of the measurement procedure, a number of photons p_j is scattered from the Be^+ ion and collected in a photomultiplier tube. The entire measurement yields a series of photon counts, $\{p\}$, that are used to determine the Al^+ state (see Sec. 5.2.1). Here, we analyze the photon counts in real-time, providing the means to actively control the measurement process. Before the first cycle, we assume equal prior likelihoods for Al^+ qubit states. The probability, $P(p|S_i)$, of observing p photons given state S_i of the Al^+ system is determined based on histograms continuously updated from previous measurements [3] . The probability, $P(\{p\}|i)$, of S_i producing the observed series of photon counts is $P(\{p\}|S_i) = \prod_j P(p_j|S_i)$. Applying Bayes' rule,

$$P(S_i|\{p\}) = \frac{P(\{p\}|S_i)}{\sum_k P(\{p\}|S_k)}, \tag{5.14}$$

yields the probability of a particular state S_i given the observed series of photon counts. Here, k spans all states in the Al^+ system, in this case $|\downarrow\rangle_{Al}$ and $|\uparrow\rangle_{Al}$. This procedure provides both the most likely state of Al^+, $S_{i'}$, and also the probability of measurement error, $1-P(S_{i'}|\{p\})$. The first assigns detection outcomes, while the second is used to optimize the measurement process. Specifically, we repeat the detection cycles only until the aggregate detection reaches a desired (threshold) error probability.

To experimentally determine the error rate for state discrimination, we compare two consecutive detection sequences, each of which separately determines $S_{i'}$ and reaches a specified minimum error probability. If the two results agree, both detections are counted as correct, while disagreement signifies an error. This analysis allows us to compare the actual error rate with the real-time prediction. Errors quantified in this way also represent the fidelity of quantum state preparation [Lupascu 06]. The results for a single Al^+ ion are plotted in Fig. 5.3 as a function of the specified threshold likelihood ratio (the greater of $P(\{p\}||\uparrow\rangle_{Al})/P(\{p\}||\downarrow\rangle_{Al})$ and $P(\{p\}||\downarrow\rangle_{Al})/P(\{p\}||\uparrow\rangle_{Al})$). The observed errors agree well with the predicted error rate for fidelities up to 99.94 %. In the case of detecting $|\downarrow\rangle_{Al}$, the observed error rate is as low as

[3] Updates are made by applying an exponential filter to previous measurement results (1/e at 100 to 1000 measurements), providing accurate histograms even if experimental parameters slowly drift.

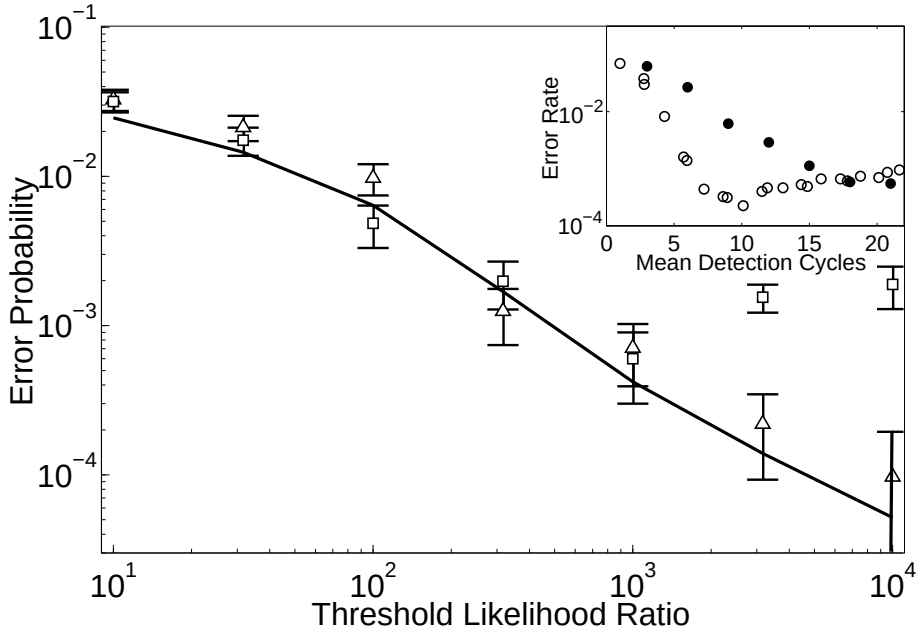

Figure 5.3: Observed (symbols) and calculated (solid line) error rates for repeated detections plotted as a function of the threshold likelihood ratio, which is defined as the greater of $P(\{p\}||\uparrow\rangle_{A1})/P(\{p\}||\downarrow\rangle_{A1})$ and $P(\{p\}||\downarrow\rangle_{A1})/P(\{p\}||\uparrow\rangle_{A1})$. The $^1S_0$ detections (triangles) reach a repeatability of 99.99 % while $^3P_0$ detections (squares) are limited by the state lifetime to 99.94 %. This is achieved for a desired likelihood ratio of 10^3, requiring a mean number of detection cycles equal to 6.54. Inset: Simulation of qubit detection, using experimental histograms, comparing the case in which the number of detection cycles is fixed (filled circles) to that in which it is adaptive (open circles). The ability to estimate errors in real time significantly increases measurement efficiency.

9×10^{-5} consistent with the threshold chosen. However, for $|\uparrow\rangle_{A1}$ detections, the state lifetime $\tau_0 = 21$ s limits the number of times the detection cycle can be repeated and still yield an accurate prediction. Here, the observed error rate reaches a minimum at 6×10^{-4}, then increases to above 1×10^{-3} as we demand higher measurement confidence through more repetitions. This error rate agrees with that predicted from the decay rate and the interval between detection cycles. The $|\uparrow\rangle_{A1}$ state lifetime and measurement cycle duration, t_c, set an upper bound on the attainable detection fidelity; that is, no measurement can achieve an error rate lower than the probability of decay before the first detection, $t_c/\tau_0 \simeq 10^{-4}$ in the experiment here.

To investigate the gain in sensitivity achieved with adaptive measurements, we perform a Monte-Carlo simulation of the detection procedure based on experimentally observed histograms. We compare the adaptive scheme, which uses the minimum number of cycles necessary to achieve a given fidelity, to

a detection scheme where the number of detection cycles is set to a particular value [Fig. 5.3(inset)]. The simulation assumes uncorrelated errors and includes spontaneous decay based on the known $^3P_0$ state lifetime and an experimental cycle time. In both the adaptive and fixed cases the final state determination results from Bayesian analysis, which gives optimal results based on the detection record. As a function of mean detection duration, the adaptive detection gives an exponentially lower error rate until reaching the minimum error imposed by spontaneous decay. Although the minimum error achieved is nearly equal for both cases, the adaptive scheme decreases the average time required to reach the minimum by more than a factor of two. In the absence of effects such as spontaneous decay, which disturb state populations, this gain in measurement efficiency would continue independent of the detection time.

5.2.3.2 Al-Be-Al:

Adaptive detection also provides a means to measure and prepare the state of a multiple qubit system without the need for individual qubit addressing. To demonstrate the detection of two Al^+ ions, we investigate two different schemes. First, we describe detection with a three ion array (one Be^+ centered between the two Al^+), then show how we improve the measurement performance by using a four ions (two Al^+ centered between two Be^+). The single meter qubit in the three ion array can yield at best one bit of information in a measurement cycle. However, repeating the measurement process and varying the parameters of the interaction yields more information [Haroche 06].

The first step in the three ion experiments is to ensure that the ions occupy the correct configuration (Al-Be-Al). This is accomplished by applying a bias field perpendicular to the trap axis, $E_R \simeq 500$ V/m, which is strong enough to put the ions in a triangular configuration with the two Al^+ ions on the outside because of the mass dependence of the pseudopotential. Relaxing to $E_R = 0$ V/m prepares the symmetric axial ion configuration. In each measurement cycle all nine normal modes are Doppler cooled. The antisymmetric modes, which normally do not couple to Be^+, are Doppler cooled sympathetically by again distorting the ion array with a bias field, $E_R \simeq 300$ V/m, then adiabatically relaxing the system back to the aligned configuration (see Sec. 4.4). The two axial modes that couple to Be^+ are cooled to the ground state and then Be^+ is prepared in $|\downarrow\rangle_{\mathrm{Be}}$.

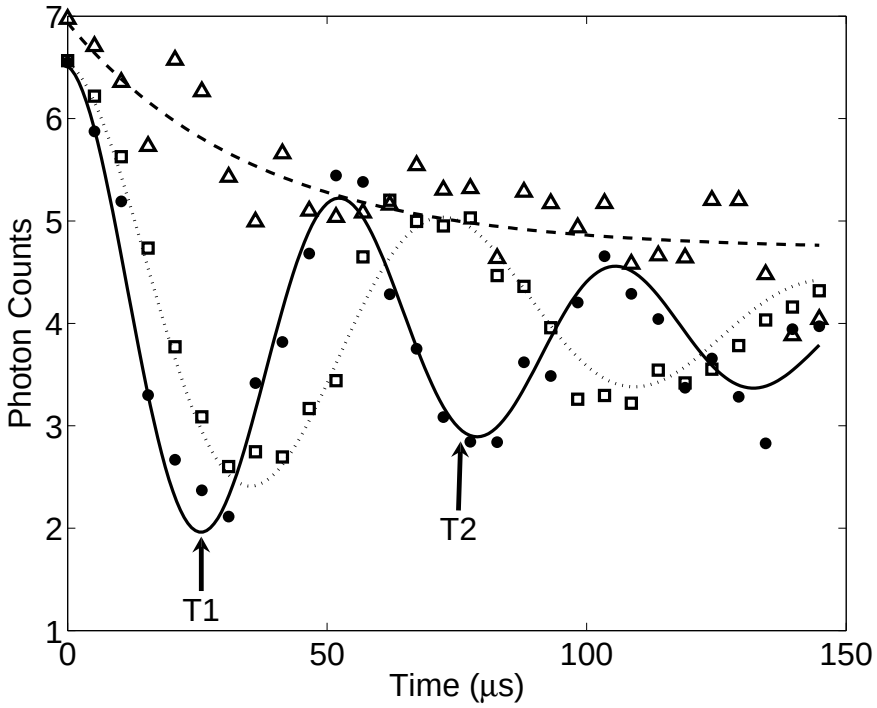

Figure 5.4: Red sideband Rabi flopping on the $|\downarrow\rangle_{\mathrm{Al}} - |^3\mathrm{P}_1\rangle_{\mathrm{Al}}$ transition beginning with one quantum of motion. The fluorescence signal is obtained after transferring the motional information to the qubit state of Be^+. The three possible numbers of ground state Al^+ ions, $N_\downarrow = 2$ (solid circles), $N_\downarrow = 1$ (empty squares), and $N_\downarrow = 0$ (empty triangles), are distinguished by their sideband Rabi rate. For zero ground state ions, the known signal admixture from one ground state ion due to detection errors was removed. We determine the state of excitation in the aluminum ion system after making multiple mapping sequences with pulses of duration T1 or T2.

While the primary steps of the 3-ion procedure are identical to the 2-ion procedure above, the weaker mode couplings for Be^+ lead to a longer Doppler cooling duration ($\sim$ 4 ms) and Raman cooling duration ($\sim$ 2 ms). To couple the Al^+ system to the Be^+ system (step 4) we use a slightly different procedure:

(1) $|\downarrow\rangle_{\rm Be}|0\rangle_m \rightarrow |\uparrow\rangle_{\rm Be}|1\rangle_m$ π-pulse

(2) $|\downarrow\rangle_{\rm Al}|1\rangle_m \leftrightarrow |^3{\rm P}_1\rangle_{\rm Al}|0\rangle_m$ (variable duration)

(3) $|\uparrow\rangle_{\rm Be}|1\rangle_m \rightarrow |\downarrow\rangle_{\rm Be}|0\rangle_m$ π-pulse,

where the total duration is approximately 50 - 100 μs. The first pulse inserts a quantum of motion and the second pulse removes it dependent on the Al^+ state. If we apply the Morris-Shore transformation (see Sec. 2.3) to the $|\downarrow\downarrow\rangle_{\rm Al}$ state evolution in step (2) we can describe the rsb Rabi flopping for this case in terms of an effective two-state system. The Al^+ states, then, are distinguished by their relative Rabi flopping rates between $|1\rangle_m$ and $|0\rangle_m$, which depend only on the number of ions, $N_\downarrow \in \{0, 1, 2\}$, in the state $|\downarrow\rangle_{\rm Al}$. Step (3) translates a motional excitation into a flipped spin in the Be^+ qubit. Experimental excitation curves for these three cases are plotted in Fig. 5.4 as a function of pulse duration. With $N_\downarrow = 0$ no Rabi flopping occurs. With $N_\downarrow = 1$, in the Lamb-Dicke limit, Rabi flopping between $|\downarrow\rangle_{\rm Al}|1\rangle_m$ and $|^3{\rm P}_1\rangle|0_{\rm m}\rangle$ will proceed with a Rabi rate given by $\Omega_{R,1} \simeq \Omega_c\eta$, where Ω_c is the carrier Rabi frequency and η is the Lamb-Dicke parameter for each of the aluminum ions [Monroe 95]. With $N_\downarrow = 2$, both ions contribute coherently to the sideband excitation. Rabi flopping carries the aluminum system to an entangled state, $|\downarrow\downarrow\rangle_{\rm Al}|1\rangle_m \rightarrow \frac{1}{\sqrt{2}}\big(|^3{\rm P}_1\uparrow\rangle_{\rm Al} + |\downarrow {}^3{\rm P}_1\rangle_{\rm Al}\big)|0\rangle_{\rm m}$ with characteristic Rabi rate $\Omega_{R,2} \simeq \sqrt{2}\Omega_c\eta$ [King 98]. We find good agreement between the fitted Rabi flopping rates and the rates expected based on separate calibrations of Ω_c and η.

Two particular transfer pulse durations, T1 = 30 μs and T2 = 80 μs, exhibit good discrimination between one particular state and the other two. A combination of detection cycles using these two pulse durations distinguishes the three states. In this scheme, the real-time Bayesian analysis plays the additional role of determining the pulse duration that maximizes contrast between the two most-likely states based on previous measurements. As before, we measure the error rate for state discrimination by comparing consecutive detection sequences, and find a detection fidelity of 98.3%.

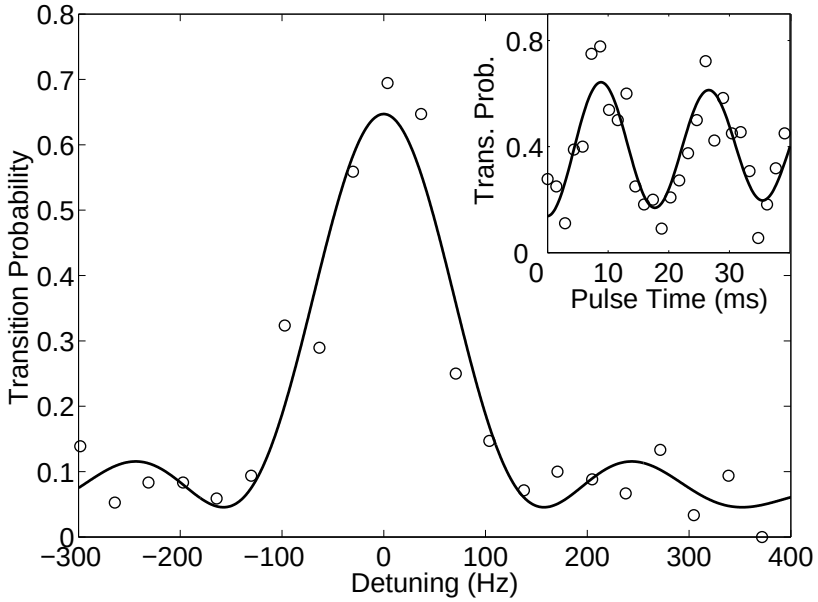

Figure 5.5: Signal from $^3P_0$ spectroscopy using two Al^+ and one Be^+. Obtaining this signal depends on the ability to prepare the $|\downarrow\downarrow\rangle_{Al}$ or $|\uparrow\uparrow\rangle_{Al}$ state of the Al^+ system because transitions between $|\downarrow\uparrow\rangle_{Al}$ and $|\uparrow\downarrow\rangle_{Al}$ will not be detected. Inset: Rabi flopping on the $^3P_0$ transition. Signal contrast is limited by fluctuations in the $^3P_0$ excitation, rather than detection efficiency.

We have performed spectroscopy of the $|\downarrow\rangle_{Al} \rightarrow |\uparrow\rangle_{Al}$ transition on two Al^+ ions using this scheme. Note that the observation of a full-contrast $|\downarrow\rangle_{Al} \rightarrow |\uparrow\rangle_{Al}$ resonance depends on our ability to prepare the state $|\downarrow\downarrow\rangle_{Al}$ or $|\uparrow\uparrow\rangle_{Al}$ before the spectroscopy pulse since transitions from $|\downarrow\uparrow\rangle_{Al}$ to $|\uparrow\downarrow\rangle_{Al}$ will not be distinguished. Figure 5.5 shows a Fourier-limited lineshape and Rabi flopping (inset), for which the experiments beginning in the states $|\downarrow\uparrow\rangle_{Al}$ and $|\uparrow\downarrow\rangle_{Al}$ have been filtered out in post-processing. Deterministic preparation of states $|\uparrow\uparrow\rangle_{Al}$ or $|\downarrow\downarrow\rangle_{Al}$ could be performed efficiently by use of sideband pulses mapping the Al^+ state to Be^+ [Schmidt 05]. Although we have high detection fidelity (98.3 %), the temperature of some radial secular modes limits signal contrast. Also, the measurement is slow, taking more than 0.5 s to reach the minimum error probability. This is due to the poor signal contrast seen in Fig. 5.4 as well as the relatively long cooling times necessary in each measurement cycle.

5.2.3.3 Be-Al-Al-Be:

To explore the improvement of measurement fidelity and efficiency by using more Be^+ ions, we have carried out experiments with two Al^+ ions positioned in the center of two Be^+ ions. This can improve the cooling rate and increase the fluorescence signal. We choose trap conditions such that $\{\omega_x, \omega_y, \omega_z\} = \{13.5, 14.1, 3.0\}$ MHz for a single Be^+, which leads to good separation in frequency for all 12 normal modes of the Be-Al-Al-Be ion array. The ions are ordered by reducing the rf trap power by 5 dB to form a diamond-shaped configuration with Al^+ ions displaced radially from the axis, then returning the rf power to the experimental settings.

The steps in the detection procedure are identical to the steps for 1 Al^+ and 1 Be^+, although the laser cooling durations are somewhat greater. This results in a total cycle time of ~ 4.5 ms. As with 1 Al^+ and 1 Be^+, the transfer of state information (step (4)) consists of a blue sideband pulse on the $|\downarrow\rangle_{Al} \rightarrow |^3P_1\rangle_{Al}$ transition in Al^+ followed by a red sideband pulse on the Be^+ qubits. In this case, the first pulse will lead to motional state $|0\rangle_m$, $|1\rangle_m$, or $|2\rangle_m$ depending on the number of Al^+ in $|\downarrow\rangle_{Al}$ and on the duration of the sideband pulse. For the state $|\uparrow\uparrow\rangle_{Al}$, no motional excitation will occur, while for $|\uparrow\downarrow\rangle_{Al}$ and $|\downarrow\uparrow\rangle_{Al}$ there will be at most one excitation. For $|\downarrow\downarrow\rangle_{Al}$, a distribution of $|0\rangle_m$, $|1\rangle_m$, and $|2\rangle_m$ will occur. We desire a pulse duration that differentiates the three Al^+ states well. To find this we note that the π-pulse

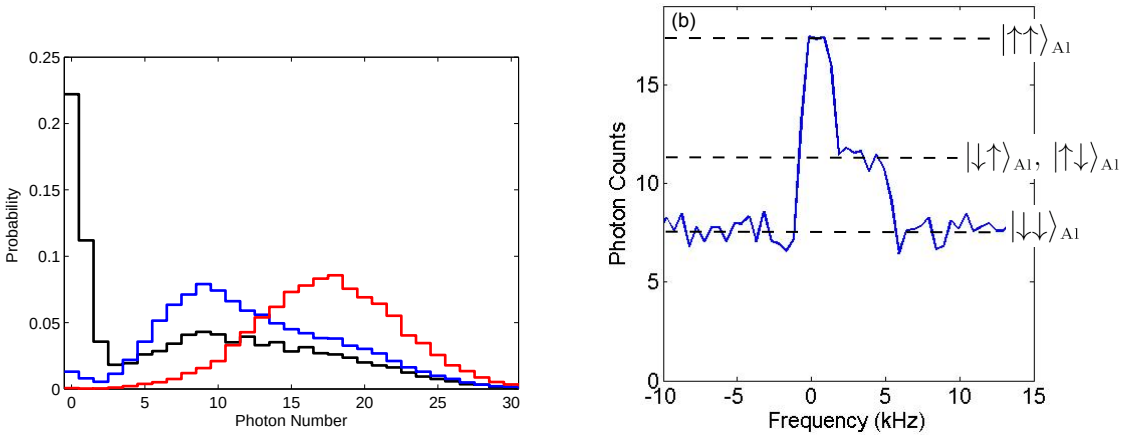

Figure 5.6: Data from the measurement of 2 Al^+ with 2 Be^+. (a) Experimental photon histograms displayed as stepped lines for the three relevant Al^+ states: $|\downarrow\downarrow\rangle_{Al}$ (black), $|\downarrow\uparrow\rangle_{Al}$ and $|\uparrow\downarrow\rangle_{Al}$ (blue), and $|\uparrow\uparrow\rangle_{Al}$ (red). (b) Demonstration of quantum jumps between the three Al^+ states. The frequency of the laser probing the transition $|\downarrow\rangle_{Al} \rightarrow |\uparrow\rangle_{Al}$ (x axis) was scanned during the experiment. Each point represents the average of 190 detection cycles.

duration, $t_\downarrow$, that achieves full transfer from $|0\rangle_m$ to $|1\rangle_m$ for $|\downarrow\uparrow\rangle_{Al}$ and $|\uparrow\downarrow\rangle_{Al}$ is close to the pulse duration, $t_{\downarrow\downarrow}$, that maximizes the probability of two motional excitations for $|\downarrow\downarrow\rangle_{Al}$. Specifically, in the Lamb-Dicke limit, $t_{\downarrow\downarrow} = (2/3)^{1/2} t_\downarrow = \pi/\sqrt{6}\Omega_c\eta$ [King 98]. We choose an intermediate pulse duration (the average of $t_{\downarrow\downarrow}$ and $t_\downarrow$) that is near optimum for both cases simultaneously. Similarly, when choosing a pulse duration for transferring the motional excitation to the Be^+ qubits, we want to maximize the distinction between the three motional states. Once again, the pulse durations t_1 and t_2 that achieve maximum transfer for $|1\rangle_m$ and $|2\rangle_m$ respectively are similar ($t_1 = (3/4)^{1/2} t_2 = \pi/\sqrt{8}\Omega_c\eta$) a duration equal to the mean of t_1 and t_2 was chosen.

As opposed to the experiment with 1 Be^+ and 2 Al^+, this single set of pulse durations was used for all detection cycles. The resulting experimental fluorescence histograms are plotted in Fig. 5.6 (a). In Fig. 5.6 (b), we plot the first quantum jump signal observed with this scheme. Three distinct fluorescence levels are observed for the cases of $N_\downarrow = 0$, 1, and 2. In this experiment, we used 190 detection cycles for each data point. The points with an intermediate fluorescence level, as the fluorescence drops from one value to a lower value, are most likely due to a spontaneous decay that occurred during the detection cycles. [4]

[4] Note that the mean fluorescence gathered at any one point leaves out all higher-order moments of the photon distribution. To see this, as a hypothetical example, consider a point where the mean fluorescence signal is half that for two fluorescing Be^+. The distribution might be evenly divided between signals from 0 and 2 fluorescing Be^+, or purely due to 1 fluorescing Be^+.

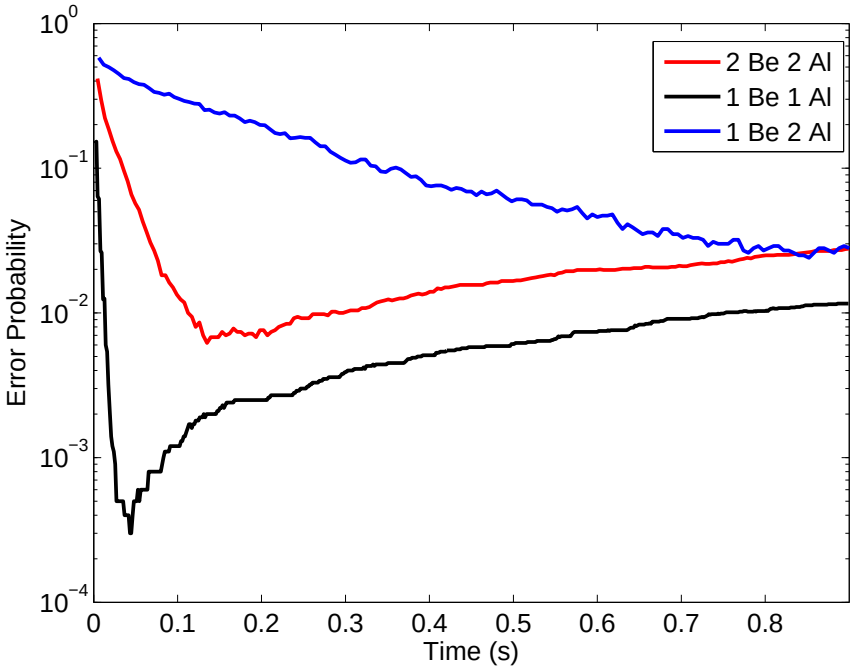

Figure 5.7: Comparison of the detection error as a function of time for the three protocols studied, 1 Al^+ 1 Be^+ (black), 2 Al^+ 1 Be^+ (blue), and 2 Al^+ 2 Be^+ (red). The curves come from a Monte-Carlo simulation of the detection process based on experimental histograms and cycle times for each case(See Sec. 5.2.1). The fidelity limit in the simulation comes from the $|\uparrow\rangle_{\mathrm{Al}}$ lifetime of $\tau_0 = 21.4$ s limits.

To quantify the fidelity using the maximum likelihood method, we perform an experiment with two independent measurement sets, separately reaching a maximum error probability. The histograms used for the likelihood determination come from experimental histograms for the three states that are continuously updated. We record a 99.8 % fidelity in a measurement duration of ~ 130 ms, which represents a substantial increase in measurement efficiency compared the previous case with 1 Be^+ and 2 Al^+.

To summarize the measurement efficiency results, we compare the efficiency of the three detection schemes by performing a Monte-Carlo simulation using experimental photon histograms and cycle times together with the known lifetime of state $|\uparrow\rangle_{\mathrm{Al}}$. The results are plotted in Fig. 5.7. We note that when the minimum measurement error is limited by the spontaneous decay, as we have assumed here, a good approximation for the error is $I = 1 - e^{-t_{opt}/N_{\mathrm{Al}}\tau_0}$, where t_{opt} is the optimum average measurement duration, and N_{Al} is the number of Al^+ ions. Thus, for a particular N_{Al}, a higher optimum fidelity will always be achieved in a shorter measurement duration, although the source of the improvement may be either shorter measurement cycles or more accurate single-shot measurements. The minimum infidelities observed by the simulation for 1 Be^+ and 1 Al^+, as well as 2 Be^+ and 2 Al^+ are slightly different from the measured minimum infidelities. This is partly due to statistical fluctuations in both the simulation and the experiment. It might also indicate slightly correlated errors between measurement cycles. The histograms tend to change slowly over time because of laser frequency drifts, magnetic field fluctuations and drifts in laser alignment. If these occur on a timescale longer than t_c, but short compared to the histogram update rate it would result in correlated errors, which are not present in the simulation. Unaccounted drifts in photon histograms could also affect the results by causing a deviation of the photon histograms used in the simulation from those sampled in the experiment.

As a concluding remark, although both experiments involving 2 Al^+ were performed with an axially symmetric ion configuration, the use of an asymmetric configuration has advantages. In some cases, the Doppler cooling rate is improved because the $3N$ modes of motion couple more strongly to the cooling ion. For example, in the case of Al-Be-Al, 3 different modes (one mode in each direction x, y and z) do not

Using only the mean fluorescence measurement these two possibilities would appear identical, but the maximum likelihood method described above would clearly distinguish them.

couple to Be^+. In these, the mode amplitudes for the two Al^+ are equal and opposite while the amplitude for Be^+ is zero. On the other hand, all nine modes of the asymmetric configuration, Be-Al-Al and its mirror image, couple to Be^+ with finite amplitude. Furthermore, numerical simulations have shown that the cooling rates achievable by distorting the asymmetric configuration with a bias field are higher than those for the symmetric case. Another potentially beneficial feature of any asymmetric configuration, independent of the total ion number, is that each ion generally exhibits a unique set of mode amplitudes. In contrast to the experiments above, this permits discrimination between states like $|{\downarrow}{\uparrow}\rangle_{\mathrm{Al}}$ and $|{\uparrow}{\downarrow}\rangle_{\mathrm{Al}}$. The unique sideband coupling strength for the different eigenstates results in a unique distribution of Fock states after a sideband pulse. As opposed to the other detection protocols described here, including resonance fluorescence detection, this enables discrimination of the 2^N eigenstates of N ion qubits without the need for individual ion addressing or spatially resolved photon counting, which might be useful in both ion spectroscopy and quantum information processing. For example at the end of a quantum computation, in general, all 2^N states must be distinguished. In spectroscopy this capability would avoid the necessity of preparing $\mathcal{S}$ in a particular state before the spectroscopy pulse.

5.3 Generalizing Indirect QND Measurements

In the preceding sections we have shown how the transfer of atomic state information can be accomplished by use of resolved sideband pulses on both the $\mathcal{M}$ and $\mathcal{S}$. This protocol uses several special features of the Al^+ system to enable both efficient transfer of state information and repetitive measurements. In particular, the scheme relies on the condition that $1/\omega_m \ll \tau_1 \ll \tau_0$, which allows resolved sideband pulses and efficient repreparation of the state $|{\downarrow}\rangle_{\mathrm{Al}}$. To limit the effect of τ_1 on measurement efficiency, we desire the more stringent constraint that $\tau_1 \ll t_c$, so that the duty cycle for measurement is not dominated by the decay time of the $^3P_1$ excited state. This inequality is satisfied to varying degrees in the experiments of Sec. 5.2.3. Another simplifying feature of the Al^+ system is that a closed transition can be isolated between the $|{\downarrow}\rangle_{\mathrm{Al}}$ and $|^3P_1\rangle$ states by using pure $\hat{\sigma}^+$ or $\hat{\sigma}^-$ polarized light, which ensures that Eq. 5.3 is satisfied. Interesting atomic and molecular systems rarely exhibit this combination of conditions. Here I briefly consider other methods for state-dependent motional excitation that may relax the requirements on the primary atomic

system.

5.3.1 QND Detection through Arbitrary States of Motion

A general formulation of the indirect detection of ion states makes no assumption about the method used to map electronic state information from $\mathcal{S}$ into the motion, nor the method used to transfer motional excitation into the electronic state of $\mathcal{M}$. However, I still assume that resonance fluorescence detection ultimately transfers information in $\mathcal{M}$ to the measuring apparatus. The efficiency for any such measurement depends only on a single set of conditional probabilities $\{P(p|S_i)\}$, relating photon probabilities to the initial state. In principle, the process that leads to these conditional probabilities can be completely incoherent and might not involve the electronic state of $\mathcal{M}$ at all, e.g. a state-dependent heating of the ion array leads to a loss in fluorescence from $|\downarrow\rangle_{\mathrm{Be}}$ (see Sec. 5.3.3). In this section I restrict my discussion to processes that involve the electronic state of $\mathcal{M}$, like the detection protocols described above. If we expand an arbitrary motional state in terms of the Fock states, we can write,

$$P(p|S_i) = \sum_{j,n} P(p|M_j)P(M_j|n)P(n|S_i). \tag{5.15}$$

This divides the problem of calculating $P(p|S_i)$ into three distinct steps. The factor $P(p|M_j)$ has already been calculated numerically in Sec. 5.2.2 for Be^+ from considerations of the photon counting rate and repumping rate. A similar calculation can be applied to other atomic ions. In what follows we individually consider the factors $P(M_j|n)$ and $P(n|S_i)$.

A first step in expanding the applicability of indirect state detection to a larger group of atomic and molecular ions is to consider producing state-dependent motion without driving resolved sideband transitions on system $\mathcal{S}$. The synthesis and analysis of various ion motional states have been described previously [Meekhof 96, Leibfried 96]. In that work they show that general Fock state distributions can be sensitively reconstructed by analyzing state populations for a single ion qubit after applying a sideband pulse of variable duration. We consider here the use of sideband pulses on system $\mathcal{M}$ to distinguish arbitrary states of motion for the purpose of detecting the electronic state of $\mathcal{S}$. We also point out where these ideas could be useful for spectroscopy of atomic or molecular systems with certain features. As before, the quantum coherence

between individual Fock state components does not affect the measurement statistics, and the probabilities represented by $P(n|S_i)$ are just the diagonal elements of the reduced density matrix after tracing over electronic degrees of freedom.

As an example, with a single ion in system $\mathcal{M}$ and for a general distribution of Fock states, P_n, we consider applying a laser pulse tuned to the red sideband of the $|\downarrow\rangle_{\mathcal{M}} \rightarrow |\uparrow\rangle_{\mathcal{M}}$ resonance . The ion state probability evolves as,

$$P(|\downarrow\rangle_{\mathcal{M}}) = \sum_{n=0}^{\infty} P_n \cos^2(\Omega_n t) \tag{5.16}$$

$$P(|\uparrow\rangle_{\mathcal{M}}) = 1 - P(|\downarrow\rangle_{\mathcal{M}}), \tag{5.17}$$

where $\Omega_n = \sqrt{n}\Omega_c\eta$ in terms of the meter ion's Lamb-Dicke parameter, $\eta \ll 1$. The amplitude of spectral components in the red sideband state evolution at frequencies $\{\Omega_n | \, n \in [0\,\infty]\}$ can be used to reconstruct Fock state distributions P_n. To efficiently distinguish only a limited set of known distributions, a small number of measurements at one or more particular pulse durations are sufficient. The pulse durations can be optimized (as in Sec. 5.2.3) by minimizing Eq. 5.8 as a function of t. With more than one ion in system $\mathcal{M}$, the state evolution during a sideband pulse becomes more complicated. For any set of states in $\mathcal{M}$ the coupling strengths between states can be calculated as in Eq. 2.9, and the state evolution can be determined numerically by integrating Schrodinger's equation.

5.3.1.1 Thermal States:

Two important classes of ion motional states are thermal states and coherent states. Thermal states occur as the result of stochastic processes such as laser cooling or heating due to electric field fluctuations. From the ground state, an array of ions can be heated to a thermal state characterized by the mean motional occupation, $\overline{n}_{\text{th}}$, which is an ensemble average over many preparations of the same state. The individual Fock state probabilities are given by,

$$P_{\text{th}}(n) = \frac{\overline{n}_{\text{th}}^{\,n}}{(\overline{n}_{\text{th}}+1)^{n+1}}. \tag{5.18}$$

By substituting Eq. 5.18 into Eq. 5.16 and evaluating the sum, we obtain the $|\downarrow\rangle_{\mathcal{M}}$ probability as a function of the pulse duration, which can be optimized for minimum detection error. As an illustration, consider a

system $\mathcal{S}$ comprised of a single ion with the same basic features in its atomic structure as Be^+ (Fig. 5.2). The relevant features are qubit levels $|\downarrow\rangle$ and $|\uparrow\rangle$, with $|\downarrow\rangle$ connected to an auxiliary excited state with resonant linewidth $\Gamma_{\mathcal{S}}$. We assume that $\Gamma \gg \omega_m$ so that the motional sidebands are not resolved. Beginning with $\mathcal{S}$ in an unknown state, the system is prepared by laser cooling to the ground state using system $\mathcal{M}$. Then a laser pulse detuned by $\Gamma_{\mathcal{S}}/2$ blue of the strong resonance in $\mathcal{S}$ is applied, which heats the ions depending on the qubit state. If the ion is in $|\downarrow\rangle_{\mathcal{M}}$ the ion array will heat, while if it is in $|\uparrow\rangle_{\mathcal{M}}$ they will remain close to the ground state. These two states of motion can be distinguished as described above.

In the absence of resolved sidebands, the use of thermal states for transferring information would be advantageous in any scenario where it is less efficient or impractical to directly collect the photons from the auxiliary resonance in $\mathcal{S}$. For example, the resonance in $\mathcal{S}$ might be at a laser wavelength beyond the spectral response of efficient optics and detectors. Alternatively, the rate of photon scattering from $\mathcal{S}$ might be too low for efficient optical detection. This can occur if the linewidth $\Gamma_{\mathcal{S}}$ is relatively small, or if there exists a slow decay channel branching from the auxiliary excited state. In either case more efficient detection could be achieved by analyzing ion motion with $\mathcal{M}$. Finally, we note that the fidelity of fluorescence detection can be limited (as with Be^+) by off-resonant repumping of $|\uparrow\rangle_{\mathcal{M}}$. Since optical collection efficiency is generally on the order of 1×10^{-3}, many photons are scattered for every one collected. With detection by ion heating, relatively few scattered photons will create a measurable change in ion motion, and in some cases the maximum detection fidelity with thermal state detection could be better than with direct fluorescence detection.

5.3.1.2 Coherent States:

Another important class of motional states are the coherent states (a general discussion of coherent state properties is presented in [Haroche 06] and [Walls 08]). These states can be generated by applying a classical driving force to the ions, i.e. by applying an oscillating electric field at frequency ω_m. A coherent state $|\alpha\rangle$ is decomposed in the Fock state basis as,

$$|\alpha\rangle = e^{\frac{-|\alpha|^2}{2}} \sum_{n=0}^{\infty} \frac{\alpha^n}{\sqrt{n!}} |n\rangle, \tag{5.19}$$

where α is a complex number. The probabilities of the individual Fock states are

$$|\langle n|\alpha\rangle|^2 = \frac{e^{-|\alpha|^2}|\alpha|^{2n}}{n!}. \tag{5.20}$$

A coherent state can be generated dependent on the electronic state by applying Raman beams with frequency ω_L and $\omega_L - \omega_m$ respectively, detuned from an optical resonance of one qubit state in $\mathcal{S}$ by a frequency $\Delta_R \gg \omega_m$ [Wineland 98].

For a relevant example consider a single Al^+ as system $\mathcal{S}$. Suppose the Raman lasers have k-vectors $\mathbf{k}_1$ and $\mathbf{k}_2$ with k-vector difference $\mathbf{\Delta k} \equiv \mathbf{k}_1 - \mathbf{k}_2 = \Delta k\hat{z}$. The σ^+ components of the lasers set up an oscillating dipole force at frequency ω_m that couples only to the state $|\downarrow\rangle_{\mathrm{Al}}$[5] . A resonant classical force applied to an ion for some time t_F acts as a displacement operator $D(\alpha)$ in phase space. For the purposes of this section we are concerned only with the absolute value, $|\alpha(t)|$, since the phase of the coherent state does not affect the measurement outcome. We assume that the electric field amplitude for the σ^+ components of both Raman beams are equal so that we can quantify their coupling strength to the carrier transition $|\downarrow\rangle_{\mathrm{Al}} \rightarrow |^3\mathrm{P}_1\rangle_{\mathrm{Al}}$ with a single Rabi frequency Ω_0. Then the magnitude of the coherent state is $|\alpha(t)| = \eta\Omega_0^2 t_F/\Delta_R$. State dependent coherent states can be produced up to an amplitude near the Lamb-Dicke regime $\eta \sim 1$, $\sqrt{2|\alpha(t)|^2+1}\Delta k_z z_0 \simeq 1$, where extent of the motional wavepacket is on the same order as the effective wavelength of the driving fields. Note also, that in this scheme, with a component of σ^- polarization, that it is possible to drive two-photon Raman transitions between the groundstate $m_F = 5/2$ and $m_F = 1/2$. This process can be avoided by going to a sufficient magnetic field such that the Zeeman transition is sufficiently detuned, or by going to a counter-propagating beam configuration with only σ^+ polarization.

The main benefit of transferring information between ion systems through coherent states of motion is that excitation to the intermediate electronic state, in this case $|^3\mathrm{P}_1\rangle_{\mathrm{Al}}$, can be strongly suppressed. If negligible state population is transferred to the intermediate state, Eq. 5.3 can be satisfied without the presence of a cycling transition. This capability could be applied to atomic and molecular systems with complicated structures, to allow repeated detection of a long-lived state. The use of Raman beams also suppresses the probability of spontaneous emission, P_{SE} which is essential for maintaining coherence between

[5] In general, the magnitude of the dipole force depends on the polarizabilities of the electronic states of $\mathcal{S}$ at the frequency ω_L, and a variety of laser configurations can be utilized dependent on the details of the atomic system.

electronic eigenstates (See Sec. 5.3.2). In the Al^+ example,

$$P_{SE} = \frac{t_F}{\tau_1}\left(\frac{2\Omega_0^2}{\Delta_R^2} + \frac{\Omega_{3/2}^2}{\Delta_{3/2}^2}\right), \tag{5.21}$$

where $\Omega_{3/2}$ and $\Delta_{3/2}$ are the coupling strength and detuning respectively of the $\hat{\sigma}^-$ polarization component coupling to the state $|^3\mathrm{P}_1, \mathrm{m_F} = 3/2\rangle$. With typical experimental parameters $P_{SE} < 1 \times 10^{-2}$, $|\alpha| \sim 1$ and $t_F < 100\ \mu$s.

5.3.2 QND Measurements for Entanglement Generation

Resonance fluorescence detection projects the ion into an eigenstate of the atomic system on a timescale of nanoseconds, extinguishing any coherence that existed in the atomic state before measurement. Likewise, the techniques for indirect detection presented thus far project the system S into an atomic eigenstate with near unit probability after a single measurement cycle. This happens primarily as a result of photon scattering from system M, but also as a result of spontaneous emission from $|^3\mathrm{P}_1\rangle_{\mathrm{Al}}$. Measurements that result in only partial quantum state collapse are an interesting way of studying the progressive loss of coherence during measurement [Katz 06]. This could be achieved in our experiments by transferring information through coherent states, as described above, or by other mechanisms that avoid spontaneous decay from $|^3\mathrm{P}_1\rangle_{\mathrm{Al}}$. It could also be beneficial to make measurements that project the ion state into a basis other than the basis of atomic eigenstates. For both fluorescence detection and indirect detection it is possible to effectively make a measurement in any basis by first mapping the desired measurement basis into atomic eigenstates, measuring as usual, then mapping the atomic eigenstates back into the measurement basis. However the measurement fidelity and the fidelity of the final state in the measurement basis are both limited by the fidelity of the mapping operation. To state it a different way, this is a QND measurement only to the extent that the mapping operations are perfect. In the case of effectively projecting a state into an entangled basis, for example, the process requires two entangling operations, which typically have low fidelity.

Entanglement has been generated deterministically and observed in trapped ions in a number of different ways. For example, the original Cirac-Zoller proposal has been implemented [Schmidt-Kaler 03], and several subsequent proposals that address sources of infidelity in the Cirac-Zoller proposal have been ex-

plored experimentally [Leibfried 03, Benhelm 08]. Entanglement has also been generated probabilistically by observing coincidence counts in scattered photons from two ions [Matsukevich 08]. In this section, motivated by the high fidelities achieved in measuring atomic eigenstates, we explore a different method for probabilistically generating entangled states through indirect measurements. As in the previous probabilistic scheme, the entanglement is heralded. This means that, when the entangling operation has been successful, there is an observable effect that does not disturb the entanglement, i.e. fluorescence from the Be^+ system. In principle, the measurement can be repeated to achieve higher fidelity, since it is a QND measurement. Below we show how these features provide a means to reduce the effects of most sources of infidelity, such as residual Stark shifts and photon scattering, at the expense of a lower rate for generating entanglement.

The basis for our entanglement scheme is a two-ion parity measurement. The parity operator for two qubits is given by,

$$\hat{\Pi} = |\uparrow\uparrow\rangle\langle\uparrow\uparrow| + |\downarrow\downarrow\rangle\langle\downarrow\downarrow| - (|\uparrow\downarrow\rangle\langle\uparrow\downarrow| + |\downarrow\uparrow\rangle\langle\downarrow\uparrow|). \tag{5.22}$$

We refer to the states with eigenvalue 1 as even-parity states and states with eigenvalue -1 as odd-parity states. Suppose we measure $\hat{\Pi}$ for a general 2-qubit pure state, $|\psi\rangle = c_0|\downarrow\downarrow\rangle + c_1|\downarrow\uparrow\rangle + c_2|\uparrow\downarrow\rangle + c_3|\uparrow\uparrow\rangle$, with $\sum_{i=0}^{3} |c_i|^2 = 1$. We will observe an even-parity state with probability $P_1 = |c_0|^2 + |c_3|^2$ and an odd parity state with probability $P_{-1} = |c_1|^2 + |c_2|^2$. The state projection during such a measurement produces the final states,

$$|\psi_1\rangle = \frac{c_0|\downarrow\downarrow\rangle + c_3|\downarrow\downarrow\rangle}{\sqrt{P_1}} \tag{5.23}$$

$$|\psi_{-1}\rangle = \frac{c_1|\downarrow\uparrow\rangle + c_2|\uparrow\downarrow\rangle}{\sqrt{P_{-1}}}. \tag{5.24}$$

In general, these are entangled states and the degree of entanglement can be controlled by the preparation of $|\psi\rangle$. Maximal entanglement can be generated from a separable state if, for instance, $c_i = 1/2$ for all i. On the other hand if the state before measurement is the separable state $|\downarrow\downarrow\rangle$, the projected state after measurement will still be $|\downarrow\downarrow\rangle$. Therefore, parity measurements are not measurements in an entangled basis, but, with the proper preparation of the input state, the measurement can project a separable state into an entangled state. To accomplish this, there is an additional requirement beyond the QND requirements of Eq. 5.1-Eq. 5.3. Specifically, coherence between any states of the same parity must be maintained. Thus,

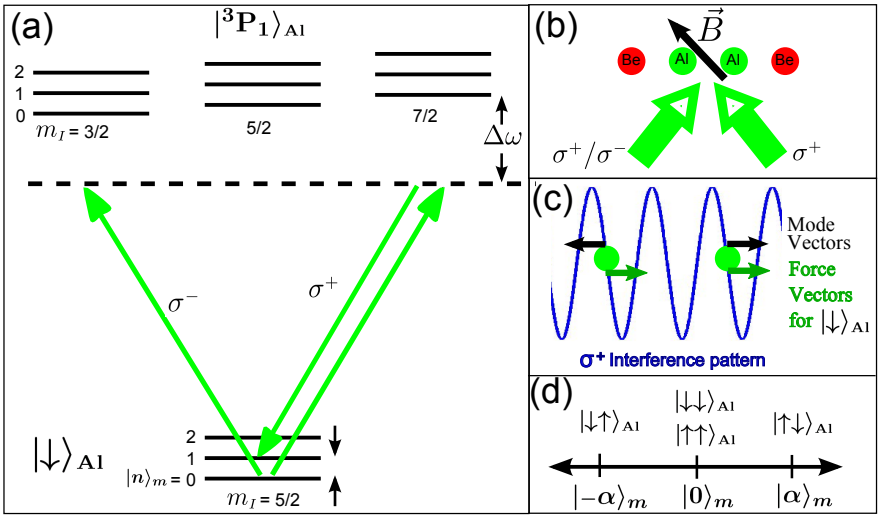

Figure 5.8: A set of drawings that portray several aspects of the scheme for projecting two Al^+ into an entangled state by QND measurements. (a) States of Al^+ and laser configuration (b) Laser beam geometry and ion configuration. (c) Mode vectors for the mode at ω_m and dipole force vectors for the state $|\downarrow\downarrow\rangle_{Al}$. The states $|\uparrow\downarrow\rangle_{Al}$ and $|\downarrow\uparrow\rangle_{Al}$ will experience this force for only the ion in state $|\downarrow\rangle_{Al}$, while the state $|\uparrow\uparrow\rangle_{Al}$ experiences negligible forces. (d) The forces and mode vectors in (c) result in the excitation of coherent states of motion depending on the ion states. For $|\downarrow\downarrow\rangle_{Al}$ and $|\uparrow\uparrow\rangle_{Al}$ no motional excitation occurs, whereas $|\downarrow\uparrow\rangle_{Al}$ and $|\uparrow\downarrow\rangle_{Al}$ are excited to coherent states of magnitude $|\alpha|$ but out of phase by π rad.

the effects that can limit the fidelity in deterministic entanglement protocols, such as spontaneous emission and fluctuating Stark shifts, can also limit the fidelity for this probabilistic protocol.

In measurements of atomic eigenstates, neither spontaneous emission nor Stark shifts, affect the measurement fidelity. The relatively straightforward protocols of Sec. 5.2.3 have a high probability of spontaneous emission from $|^3P_1\rangle_{Al}$ and Stark shifts on $|\downarrow\rangle_{Al}$ of ~ 10 rad in a single measurement cycle. To maintain coherence between states of equal parity, we need a protocol that reduces both of these effects. I have already described how to avoid spontaneous emission by mapping information through coherent states of motion, and will apply those ideas to a scheme for entangling two Al^+ ions. A pair of off-resonant Raman beams, with frequencies ω_L and $\omega_L - \omega_m$ respectively, detuned from the $|\downarrow\rangle_{Al} \rightarrow |^3P_1\rangle_{Al}$ resonance by Δ_R produce a coherent motional state with small probability of excitation to $|^3P_1\rangle_{Al}$. In Fig. 5.8 (a), we show the directions of the laser beams and the external magnetic bias field relative to the ion array. As in Sec. 5.2.3 (c) we choose a symmetric configuration with 2 Al^+ centered between 2 Be^+ because we can fix the ion array in this order by adjusting trap parameters and the symmetry ensures equal mode amplitudes for both Al^+

ions for all modes. The two laser beam k-vectors, k_1 and k_2, are oriented such that $\Delta k = k_1 - k_2$ is directed along the trap axis. The frequencies and polarizations chosen set up a sinusoidal interference pattern in the σ^+ polarized light that causes a z-dependent Stark shift, E_S. The corresponding dipole force, $F = -\partial E_S/\partial z$ oscillating at frequency ω_m acts as a resonant, classical driving force on an in state $|\downarrow\rangle_{\mathrm{Al}}$. In Fig. 5.8 (b) we present a conceptual picture of the intensity modulation and the resulting forces with respect to the mode vectors for stretch mode ($\Delta\phi_m = \pi$).

We choose the Al^+ ion spacing, d, such that $\Delta k d = 2\pi l_\lambda$, where l_λ is a whole number. For Be-Al-Al-Be this occurs, for instance, when the stretch mode frequency is $\omega_m = 4.778$ MHz, for which $d = 3.02\mu$m and $l_\lambda = 16$. Since any Al^+ in state $|\uparrow\rangle_{\mathrm{Al}}$ experiences negligible force, and the force vectors for $|\downarrow\downarrow\rangle_{\mathrm{Al}}$ do not overlap with the mode vectors, ideally, no motion will be produced for the even parity states. In particular, $F_{\downarrow\downarrow} = F_{\uparrow\uparrow} = 0$, likewise $F_{\downarrow\uparrow} = -F_{\uparrow\downarrow} = F_0 \sin(\omega_m t)$, where F_0 is the peak force magnitude for a single ion. A resonant classical force acts like a displacement operator, $D(\alpha) = e^{\alpha a^\dagger + \alpha^* a}$ in phase space. The displacements for each state are depicted in Fig. 5.8 (c). The magnitude of the displacement for $|\uparrow\downarrow\rangle_{\mathrm{Al}}$ and $|\uparrow\downarrow\rangle_{\mathrm{Al}}$ is given by $|\alpha| = F_0 z_0 t_F/2\hbar$, where t_F is the duration of the driving force, and z_0 is the ground state amplitude of motion for the Al^+ ions. For the trap conditions described above $z_0 = 3.57$ nm. The presence or absence of motion can be used to distinguish the parity of the two Al^+ state using a red sideband transition on the Be^+ system.

The Stark shifts that drive the coherent motion also introduce phase shifts to the atomic states. The phase shift is the accumulated Stark shift over the duration of the drive pulse and is given by,

$$\Delta\Phi = \frac{N_\downarrow E_S^{\max}}{2} \int_{t=0}^{t_F} \cos^2\left(-\frac{\omega_m t}{2}\right) dt = \frac{N_\downarrow E_S^{\max} t_F}{4}, \tag{5.25}$$

where $N_\downarrow$ is the number of Al^+ in state $|\downarrow\rangle_{\mathrm{Al}}$. To the extent that the laser beam intensity is equal across the two ions, the differential Stark shift between $|\downarrow\uparrow\rangle_{\mathrm{Al}}$ and $|\uparrow\downarrow\rangle_{\mathrm{Al}}$ will be zero. However for the even parity states, the overall differential Stark shift is $\frac{E_S^{\max} t_F}{2}$. With reasonable parameters, i.e. those for which $\alpha > 1$, The differential Stark shift between $|\downarrow\downarrow\rangle_{\mathrm{Al}}$ and $|\uparrow\uparrow\rangle_{\mathrm{Al}}$ is on the order of ~ 20 rad. With slow intensity drifts, which can arise from fluctuations in the laser beam position, this can cause significant decoherence between the even parity states. One way to reduce the effects of these fluctuations is to switch the detuning of the

laser beams between Δ_R and $-\Delta_R$. This changes the sign of the Stark shift on $|\downarrow\rangle_{\mathrm{A1}}$. If the detuning is switched on a timescale fast compared to the timescale of intensity fluctuations it will suppress slow drifts in the Stark shift. However, the sign of the force on the two ions also reverses. To compensate for this, the differential phase between the two Raman beams can be switched between $\Delta\phi = 0$ and $\Delta\phi = \pi$.

With the techniques described, we can produce coherent motion dependent on the parity of the two-ion state, with a small probability of spontaneous emission and suppressed Stark shifts. Now we describe two particular schemes to exploit this capability to produce heralded entangled states. The process for both follows these steps:

(1) Doppler cool using Be^+ (600 - 2000 μs)

(2) Cool axial states near the ground state of motion (~ 1500 μs)

(3) Apply a $\pi/2$ pulse on the $|\downarrow\rangle_{\mathrm{A1}} \rightarrow |\uparrow\rangle_{\mathrm{A1}}$ transition (~ 500 μs)

(4) Apply coherent displacement ($\alpha = 0.1 - 2$, $t_F = 10 - 200$ μs)

(5) Be^+ rsb (~ 10 μs)

(6) Be^+ fluorescence detection ~ 400 μs

Step (3) produces the equal superposition $|\psi\rangle_{\mathrm{A1}} = \frac{1}{2}(|\downarrow\downarrow\rangle_{\mathrm{A1}} + |\downarrow\uparrow\rangle_{\mathrm{A1}} + |\uparrow\downarrow\rangle_{\mathrm{A1}} + |\uparrow\uparrow\rangle_{\mathrm{A1}})$ to which a parity measurement is applied. The duration of step (4) is an estimate based on experimental observations and is adjusted based on the intensity of the laser beams and whether the intent is to produce $\frac{1}{\sqrt{2}}(|\downarrow\downarrow\rangle_{\mathrm{A1}} + |\uparrow\uparrow\rangle_{\mathrm{A1}})$ or $\frac{1}{\sqrt{2}}(|\downarrow\uparrow\rangle_{\mathrm{A1}} + |\uparrow\downarrow\rangle_{\mathrm{A1}})$ as described below.

To produce the even parity entangled state $|\uparrow\downarrow\rangle_{\mathrm{A1}}$ and $|\downarrow\uparrow\rangle_{\mathrm{A1}}$ are driven to a coherent state of amplitude, $\alpha = 1 - 2$, so that $|\langle 0|\alpha\rangle|^2 = e^{-|\alpha|^2}$ is relatively low, and a high measurement fidelity can be obtained with a small number of measurements. To maximize this fidelity at the expense of entanglement success rate, we can select only those experiments where all Be^+ measurements of step (6) indicate the state $|\downarrow\downarrow\rangle_{\mathrm{Be}}$, i.e. no motion was excited by the displacement drive. One difficulty with this protocol is that the long drive times lead to larger Stark shifts, which may not be perfectly canceled by switching Δ_R. Another option is to produce $\frac{1}{\sqrt{2}}(|\downarrow\uparrow\rangle_{\mathrm{A1}} + |\uparrow\downarrow\rangle_{\mathrm{A1}})$, which will experience no differential Stark shifts to the extent that the laser

beam intensity is balanced between the two ions. However, because the sign of α is opposite for the two odd-parity states, the phase difference between $|{\downarrow\uparrow}\rangle_{\mathrm{Al}}$ and $|{\uparrow\downarrow}\rangle_{\mathrm{Al}}$ in the projected state,

$$|\psi\rangle\langle n|\alpha\rangle = \frac{e^{\frac{1}{2}|\alpha|^2}|\alpha|^n}{\sqrt{2n!}}(|{\downarrow\uparrow}\rangle_{\mathrm{Al}} + (-1)^n|{\uparrow\downarrow}\rangle_{\mathrm{Al}}), \tag{5.26}$$

depends on whether the state of motion projects into an even or odd Fock state. The Fock state number can generally not be determined based on the Be^+ fluorescence measurement. One way to control the Fock-state number is to use only a small displacement $\alpha \sim 0.2$, for which the probability of projecting the odd parity states projecting into a Fock state higher than $|1\rangle$ is small. In particular, $|\langle 2|\alpha\rangle|^2/|\langle 1|\alpha\rangle|^2 = |\alpha|^2/2$, so that, for example, the value $\alpha = .2$ gives a probability of $n = 1$ that is 50 times that of $n = 2$. However, if only those detection results that show $n > 0$ are taken as a success, the probability of success in a single experiment is $|\langle 1|\alpha\rangle|^2 = 0.04$. One issue in this protocol, is that the ground state cooling must be nearly perfect to ensure that $P_{th}(|1\rangle) \ll |\langle 1|\alpha\rangle|^2$. This concern and others make the realistic prospect of reaching $F > 0.9$ experimentally challenging. Independent of entanglement fidelity it may provide and interesting path to study quantum coherence by partial-collapse measurements.

In the above, I have presented some details of a new protocol for generating entangled states based on QND measurements of the parity of an unentangled states. I specifically explored the experimental issues for carrying out the protocol on a Be-Al-Al-Be ion array. Two significant challenges are Stark-Shift cancelation for Al^+ and the relatively low fidelity of fluorescence measurements on Be^+, both of which may be improved with other atomic systems, or improved experimental protocols. At the time of writing this thesis we have demonstrated most individual steps in this protocol experimentally. We have shown ground state cooling of Be-Al-Al-Be. We have produced coherent states dependent on the Al^+ states with these four ions and have shown elimination of the motion for the case $|{\downarrow\downarrow}\rangle_{\mathrm{Al}}$ by adjustment of the Al^+ ion spacing. In addition we measured Stark shifts from the coherent drive with a single Al^+ and demonstrated the suppression of the Stark shifts during the coherent drive by switching Δ_R and $\Delta\phi$ simultaneously. Unfortunately the experiment was not completed because of by experimental difficulties, the failure of a laser system and other experimental priorities. It is possible also that a two-photon Zeeman state-changing process was affecting the experiment, which is a fact that we had not appreciated at the time. Although the experiments are

challenging, they present a novel approach to generating entangled two-ion states and provide a means to address some of the infidelities present in deterministic protocols. In addition, these ideas can be used to study the loss of coherence due to partial quantum state collapse in ions, which has previously not been studied.

5.3.3 Detection by Modulated Fluorescence

The detection schemes discussed so far require several separate laser beams for system $\mathcal{M}$ to perform Doppler cooling, detection, repumping and Raman pulses. In this section I discuss the possibility of eliminating the need for resolved-sideband Raman pulses on system $\mathcal{M}$ and performing indirect state detection with only a single laser beam tuned near resonance of a strongly allowed transition in the measurement system. I consider again detecting the state of one ion by coupling it electrostatically to a meter ion in the same trap. The basic idea behind the scheme is to use the meter ion to detect the presence of a state-dependent classical driving force near resonance with a secular mode frequency. This can be created by applying Raman beams that have a difference frequency tuned to the motional frequency for an axial mode. The effect we observe is a modulation of the fluorescence rate as a function of the phase of the classical driving force. In particular, we consider applying a Doppler cooling laser, propagating along direction $\hat{k}_L$, to the meter ion tuned to frequency ω_L such that $\omega_L - \omega_0 = -\Gamma/2$, where ω_0 is the resonance frequency for the cooling transition, and Γ is its linewidth.

The ion system simultaneously subjected to laser cooling and a harmonic driving force can be accurately modeled as a classical damped, driven harmonic oscillator. The one-dimensional equation of motion for such a system is

$$\ddot{z} + 2\gamma_d \dot{z} + \omega_M^2 z = F_0 \cos(\omega_F t + \theta_F), \tag{5.27}$$

where we have denoted the relevant motional degree of freedom as z. Here γ_d is the classical amplitude damping rate, and F_0 is the amplitude of the driving force at frequency ω_F and phase θ_F. This differential equation can be solved by assuming oscillatory solutions of the form

$$z = z_0 e^{i\omega_F t}. \tag{5.28}$$

We substitute z, $\dot{z}$ and $\ddot{z}$ in Eq. 5.27 and equate real and imaginary components. The steady-state motional amplitude, z_S, is given by,

$$z_S = \frac{F_0}{m} \frac{1}{\sqrt{(\omega_M^2 - \omega_F^2)^2 + (2\gamma_d \omega_F)^2}}. \tag{5.29}$$

which is independent of initial conditions.

The ion velocity is just the real part of the derivative of Eq. 5.28. If we assume that the ion is driven on resonance, then the peak velocity is given by

$$V_0 = \frac{F_0}{2m\gamma_d}. \tag{5.30}$$

If we denote the peak ion velocity in the direction of the laser beam used for detection as $V_k = V_0 \hat{z} \cdot \hat{k}_D$, in the rest frame of the ion the laser frequency observed will be modulated at the frequency of the secular motion such that

$$\omega_L' = \omega_L[1 + V_k \cos(\omega_M t + \theta_M)]. \tag{5.31}$$

The scattering rate as a function of time can now be written as

$$R(t) = \frac{R_0}{1 + \left[\frac{2\omega_L V_k \cos(\omega_M t + \theta_M)}{c\Gamma} - 1\right]^2}, \tag{5.32}$$

where R_0 is the on-resonance scattering rate assuming the saturation parameter, $S_0 \ll 1$. If we also assume that the maximum Doppler shift is small compared to the atomic linewidth, or $2\omega_L V_0/c\Gamma \ll 1$ (a condition which is justified with experimental parameters later), we can expand the scattering rate to first order in this parameter and arrive at the expression,

$$R(t) = \frac{R_0}{2}[1 + \frac{2\omega_L V_k}{c\Gamma} \cos(\omega_M t + \theta_M)] \tag{5.33}$$

Thus, we can detect the presence of a classical driving force by looking for a sinusoidal modulation of the fluorescence rate at frequency ω_M.

A figure of merit for any implementation of this detection scheme is the modulation depth defined as $M \equiv \Delta R/R_0$, where $\Delta R \equiv R_+ - R_-$ is the difference between the maximum and minimum fluorescence rate of Eq. 5.32. For $M \ll 1$, this becomes

$$M = \frac{2\omega_L V_k}{c\Gamma}. \tag{5.34}$$

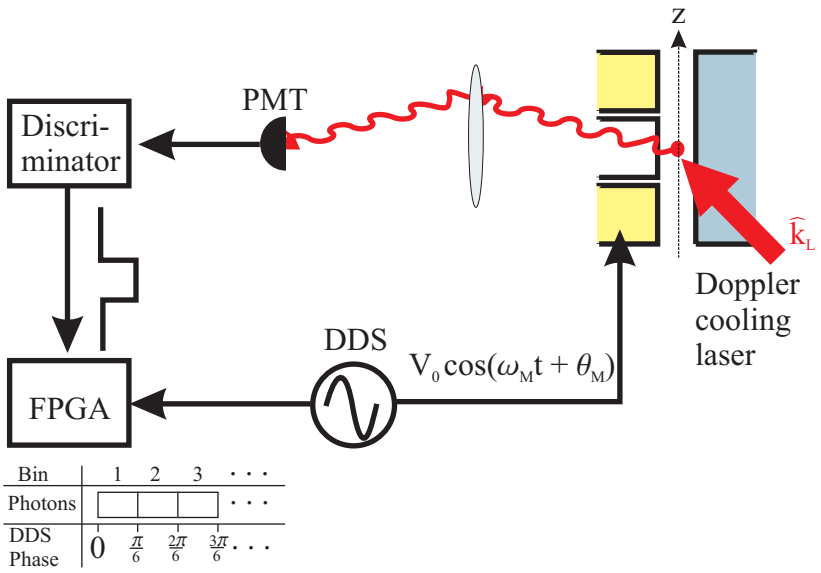

Figure 5.9: A simple schematic of the experimental setup for detecting modulation of the fluorescence from $^{25}Mg^{+}$ at the axial motion frequency. The ion is driven near a motional resonance by a DDS applying an rf signal to one endcap. Meanwhile a Doppler cooling laser is applied to the $(^2S_{1/2}, F = 3) \rightarrow {}^2P_{3/2}$ transition and the fluorescence counts from a PMT are recorded by an FPGA. The counts are binned in 12 different bins according to the rf phase at the time they were recorded, so that differences in the fluorescence rate in an rf cycle can be distinguished.

One approximation to the maximum modulation achievable would be the situation where $R_+ = R_0$. Using Eq. 5.32, this requires that $2\omega_L V_k/c\Gamma = 1$. Under this condition $R_- = R_0/5$. Because $\Delta R \sim R_0$ the minimum time scale to distinguish a driven ion from an undriven ion is approximately the same as the time scale for fluorescence detection.

We demonstrate some aspects of the detection of a classical driving force using a single $^{25}Mg^{+}$. The experimental setup is sketched in (Fig. 5.9). We perform laser cooling and detection on the $(^2S_{1/2}, F = 3) \rightarrow {}^2P_{3/2}$ cycling transition with $\Gamma = 2\pi \times 41.4$ MHz. We apply a classical driving force by modulating the voltage on one endcap at a frequency close to the axial mode frequency, $\omega_M = 2\pi \times 3.06$ MHz. The modulation signal is also fed into an FPGA board that records photon counts from the PMT. Photon counts are binned based on the phase of the modulation signal at the time they occurred [Berkeland 98].

We can observe a motional resonance by scanning the frequency of the endcap modulation and analyzing the photon count rate as a function of modulation phase. At each drive frequency, ω_F, we compute a

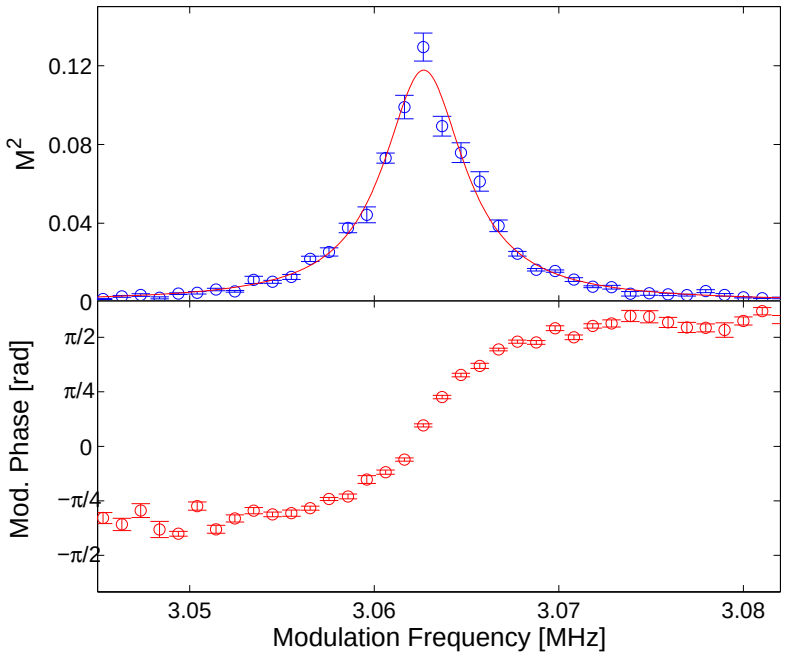

Figure 5.10: Modulation of ion fluorescence at the motional resonance frequency. (a) The square of the modulation depth (Eq. 5.34) as a function of drive frequency frequency (blue circles). (b) Modulation phase (θ_m in the text) as a function of the drive frequency. The error bars in (a) and (b) represent a 68% confidence interval in the fit of observed fluorescence to to a sine function.

weighted least-squares fit to the function

$$R(t) = \frac{R_0}{2}[1 + M\cos(\omega_F t + \theta_M)], \tag{5.35}$$

which comes from the substitution of Eq. 5.34 into Eq. 5.33. This provides the modulation depth, M, as well as the modulation phase θ_M. In Fig. 5.10 (a) we plot M^2 vs. ω_F for a particular magnitude of the driving field. We observe a Lorentzian lineshape with a linewidth of 5.3 kHz. This corresponds to a damping time of the axial mode due to Doppler laser cooling of 30 μs, which agrees well with the prediction from laser cooling theory of 34 μs. In Fig. 5.10 (b) we plot θ_M as a function of the drive frequency and observe a π phase shift as the frequency is scanned through resonance.

To use this type of signal for state detection we trap the sympathetic cooling ion together with the

ion to be studied. The classical driving force is created by two Raman beams with difference frequency ω_m. Generally the propagation direction of the two beams is set such that $\Delta\mathbf{k} = \mathbf{k}_1 - \mathbf{k}_2$ is parallel to the z-axis of the ion trap, but here we assume an arbitrary direction for $\Delta\mathbf{k}$. In this scheme the Lamb-Dicke limit imposes a bound on the achievable fluorescence modulation. The motional amplitude at the boundary of the Lamb-Dicke regime, z_{LD} is defined by $\Delta\mathbf{k} \cdot \hat{z} z_S = |\Delta k| z_S \cos(\theta_k) = 1$ where θ_k is the angle between $\Delta\mathbf{k}$ and the z axis. The peak velocity of the cooling ion in the direction of the detection laser is then

$$V_k = \frac{\omega_M}{|\Delta_k| \cos(\theta_k)} \frac{z_2}{z_1} \hat{z} \cdot \hat{k}_D, \tag{5.36}$$

where z_2 and z_1 are the relative amplitudes of motion for the meter ion and primary ion respectively for the particular secular mode chosen. It is important to note that although the Lamb-Dicke limit becomes less restrictive for smaller $|\Delta_k|$, the driving force is also reduced, requiring more laser power to achieve high motional amplitudes for a given motional damping rate.

The primary benefit of the scheme discussed here is the elimination of several separate laser beams used for Raman transitions and ground state cooling. This might significantly simplify the experimental requirements for spectroscopy of Al^+, by reducing the complexity of the laser setup and reducing the laser power requirement. Although a state-dependent measurement has not yet been perfomed on Al^+ in this way, we have demonstrated the principle with motion driven by an rf field, and further experiments are currently underway.

5.4 Conclusion

In this chapter I have explored several techniques for indirect state detection of Al^+ ions and demonstrated high-fidelity state detection on systems with one and two Al^+ ions. I also explored ideas for performing indirect state detection by use of coherent states of motion. Many of the protocols described can be adapted to other ion systems, and in some cases may perform better with alternate atomic structures. The fidelity of detection demonstrated and the flexibility of detection mediated by ion motion may lead to new experiments making measurements of otherwise unexplored atomic and molecular systems. These techniques may enable a broad array interesting experiments in spectroscopy and quantum information science.

Chapter 6

Preparation of Dicke States in an Ion Chain

Entanglement is a fundamentally nonclassical feature of quantum mechanics and has been recognized as an important resource in quantum information science [Nielsen 00]. The coherent manipulation of entangled quantum states can be useful for important tasks such as computation, cryptography, and metrology. In addition, the insights gained from research with entangled states may contribute to a better understanding of the foundations of quantum theory and shed light on physics at the boundary between the quantum and classical worlds.

Various entangled states have been experimentally demonstrated in a wide variety of physical systems including photons, condensed matter systems, atoms in optical lattices, and trapped ions [Insight 08]. In the case of trapped ions, Bell states have been generated with high fidelities [Leibfried 03, Benhelm 08]. For larger numbers of ion qubits, GHZ states [Leibfried 05, Sackett 00] and W states [Häffner 05] have been realized. As the number of physical parts in a quantum system grows, we can find more classes of entangled states [Dür 00] and potentially more interesting applications, but the state preparation and verification becomes more challenging. Here we explore numerically an approach to preparing multiple trapped ions in a general class of entangled states called Dicke states. We then demonstrate the basic protocol on a mixed-species ion chain composed of two Mg^+ ions coupled to a single Al^+ ion.

The Dicke state $|D_N^{(m)}\rangle$ is the equal superposition of all basis states of N qubits having exactly m excitations [Dicke 54]. If we denote the qubit states as $|\downarrow\rangle$ and $|\uparrow\rangle$, we can write an arbitrary Dicke state in the following form

$$|D_N^{(m)}\rangle = \binom{N}{m}^{-\frac{1}{2}} \sum_k P_k \left(|\downarrow^{\otimes(N-m)} \uparrow^{\otimes m} \rangle \right). \tag{6.1}$$

The sum is over all $\binom{N}{m}$ permutations (produced by the permutation operator P_k) with m qubits in the state $|\uparrow\rangle$. The W states are a special case of $|D_N^{(m)}\rangle$ with $m = 1$. Entanglement in Dicke states is highly resilient against external perturbations and measurements on individual qubits [Stockton 03, Dür 01]. Through projective measurements on some of the qubits in the system, we can obtain states of different entanglement classes. Thus, the Dicke states can serve as a versatile resource for the preparation of multipartite entangled states.

In addition to the technique used in [Häffner 05], other methods for the generation of Dicke states with trapped-ion qubits have been proposed [Retzker 07, Linington 08a, López 07]. The basic features of our approach follow those proposals. We consider a chain of N ion qubits each initialized in the state $|\downarrow\rangle$ and collectively cooled to the ground state of motion for a particular mode. By addressing a single ion in the chain with a laser pulse tuned to the m^{th} higher-frequency motional sideband (blue sideband) [Meekhof 96] we produce the state

$$|\psi\rangle = |\downarrow_1\downarrow_2 \ldots \downarrow_{\mathrm{N}}\rangle \otimes |m\rangle_{\mathrm{M}}, \tag{6.2}$$

where we have labeled the motional Fock state with a subscript M. From $|\psi\rangle$, a laser pulse of appropriate duration addressing all N qubits and tuned to the first lower-frequency motional sideband (red sideband), creates a state that is a close approximation of $|D_N^{(m)}\rangle$.

We define the fidelity for an arbitrary final state, ρ, as $F \equiv \langle D_N^{(m)}|\rho|D_N^{(m)}\rangle$. In the case with $m = 1$ (W states), the procedure outlined above can achieve arbitrarily high fidelity. For higher-order Dicke states the attainable fidelity is reduced because the red sideband pulse does not transfer population completely from $|\psi\rangle$ to $|D_N^{(m)}\rangle$. The previous proposals showed that this imperfection can be mitigated by postselection [Retzker 07], or by a generalization of adiabatic rapid passage [Linington 08b, Linington 08a]. However, the simplified method presented here is sufficient to achieve fidelities limited by other experimental imperfection for a range of Dicke states.

One experimental challenge in the above scheme is to individually address a single ion to produce the state $|\psi\rangle$. High confinement frequencies, and consequently small inter-ion spacing, are desirable to resolve the motional sideband spectrum. This makes individual spatial addressing difficult. We avoid this problem by introducing to the N-qubit ion chain a single ancillary ion of a different atomic species. Simultaneous

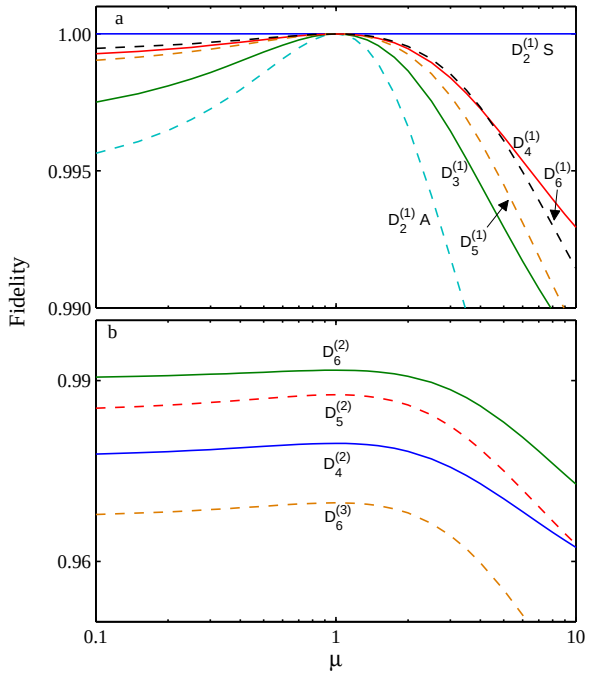

Figure 6.1: (a) Fidelity of $|D_N^{(1)}\rangle$ state generation (by use of the in-phase axial mode of motion) as a function of mass ratio, μ, for $N = 2 \ldots 6$. In the case of $N = 2$ we consider both the symmetric case labeled S, with the ancillary ion in the center, and the asymmetric case labeled A, with the ancillary ion on the outside. The latter case is the one chosen in the experiment. For $N = 3$ to $N = 6$ we assume that the ancillary ion occupies a central position in the ion chain. (b) Fidelity of $|D_N^{(2)}\rangle$ and $|D_N^{(3)}\rangle$ state generation as a function of mass ratio for $N = 4 \ldots 6$. Here the ancilla ion occupies a central position for all cases.

trapping of individual ions of two species has been used for sympathetic cooling [Barrett 03] and indirect state detection [Hume 07]. Spectroscopic resolution of the two atomic species ensures that any laser pulse applied to one species will leave the internal states of the other ion species unchanged. The state $|\psi\rangle$ can be created by applying a global laser pulse tuned to the m^{th} sideband (or equivalently m pulses sequentially tuned to the first sideband) of an accessible transition in the ancilla.

Two-species ion chains typically contain ions of unequal mass, which leads to unequal motional mode couplings. To see how this affects state fidelity, we consider the generation of W states ($|D_N^{(1)}\rangle$), for which the fidelity can be perfect in the case of equal masses. For the i^{th} ion in the chain, we denote the ground-state motional amplitude as z_i. The Lamb-Dicke parameter is defined by $\eta_i \equiv kz_i$, where k is the laser beam k-vector projection along the $\hat{z}$ direction. In the Lamb-Dicke limit ($\eta_i \ll 1$), the strength of the ion's coupling to the red sideband pulse is $\Omega_i = \Omega_0\eta_i$, where Ω_0 is the carrier ($|\downarrow\rangle|m\rangle_M \rightarrow |\uparrow\rangle|m\rangle_M$) Rabi rate.

Beginning from the state $|\psi\rangle$ with $m = 1$, under the red sideband interaction, the N-ion state acts like a two-level system as described by the Morris-Shore transformation [Morris 83]. The motion undergoes Rabi oscillations between the two Fock states $|1\rangle$ and $|0\rangle$ at a frequency, Ω' that obeys the relation

$$\Omega'^2 = \sum_{i=1}^{N} \Omega_i^2 \tag{6.3}$$

with all Ω_i real. Meanwhile the qubits evolve from $|\psi\rangle$ to the state

$$|\psi'\rangle = \frac{1}{\Omega'}\Big(\Omega_1|\uparrow\downarrow\ldots\downarrow\rangle + \Omega_2|\downarrow\uparrow\ldots\downarrow\rangle + \ldots + \Omega_N|\downarrow\downarrow\ldots\uparrow\rangle\Big), \tag{6.4}$$

in which the terms in the superposition are the same as those in $|D_N^{(1)}\rangle$ but the state amplitudes are proportional to the individual ion coupling strengths, Ω_i. The obtainable W-state fidelity, $F = |\langle D_N^{(1)}|\psi'\rangle|^2$, can be written in terms of the coupling strengths as

$$F = \frac{1}{N\Omega'^2}\left(\sum_{i=1}^{N}\Omega_i\right)^2. \tag{6.5}$$

To quantify the effect on fidelity of different mass ratios and different ion configurations, we first calculate the motional amplitudes [Kielpinski 00]. Each configuration is specified by the number of qubit ions, N, and the mass ratio $\mu = M_{\text{ancilla}}/M_{\text{qubit}}$. With one exception noted below we assume that the position of the ancilla is at the center of the chain (for N even) or adjacent to the center of the chain (for N odd). These configurations can be prepared deterministically by adjusting trap parameters. We calculate equilibrium positions for the $N + 1$ ions, then determine the amplitude of small oscillations about equilibrium. The in-phase, axial mode of motion exhibits the smallest deviations between individual ion motional amplitudes and is used for all fidelity calculations. These amplitudes give us the coupling strengths, Ω_i, and F follows from Eq. (6.5). The results are presented in Fig. 6.1(a), where we have assumed the Lamb-Dicke limit for simplicity, although fidelities for $\{\eta_i\} \approx 1$ are similar. The case labeled $D_2^{(1)}$ S is the only one that yields a theoretically perfect fidelity for any $\mu \neq 1$ because that symmetric configuration, with the ancilla in the center of two qubits, gives equal motional amplitudes for the two outer ions. The cases with $N = 3\ldots6$, as well as that labeled $D_2^{(1)}$ A, with the ancilla at the outside position, allow high fidelity over a wide range of mass ratios.

In Fig. 6.1 (b) we present the result of a similar calculation for the states $|D_N^{(2)}\rangle$ and $|D_N^{(3)}\rangle$ with

$N = 4 \ldots 6$. During the application of the red sideband pulse the ions state evolves in a complicated manner. To determine a practical upper limit on the fidelity, we numerically find the first maximum of the quantity $F = \langle D_N^{(2)} | \rho(t) | D_N^{(2)} \rangle$ as a function of the red sideband pulse duration. Here $\rho(t)$ is the reduced density matrix of the qubit system at pulse duration t after tracing over the motional degrees of freedom. We find fidelities for the case $m = 2$ as high as 0.99 and for $m = 3$ above 0.96. The effect of unequal masses is found to be similar to the W state case with a mass ratio of 10 reducing the optimum fidelity at the 1 % to 2 % level. These numbers refer to the fidelities at the first maximum during the red sideband evolution, but, in the absence of decoherence, F could in general be made higher by evolving for a longer duration and reaching a later maximum.

Note that the fidelities for $\mu = 1$ in Fig. 6.1 are equal to the fidelities obtainable in the case where there is no ancilla and $|\psi\rangle$ is generated by spatially addressing a single ion with a strongly focussed laser beam. Here, there are only N ions in the chain, and they share equal motional amplitudes for the in-phase axial mode. Under the red sideband interaction beginning from $|\psi\rangle$ the system can be transformed to a basis where it evolves as a ladder of $m + 1$ states spaced equally in energy [Rangelov 06]. Here the red sideband Hamiltonian is symmetric with respect to ion exchange, so all ions participate equally in the entangled state.

We have demonstrated the basic features of the protocol in an experiment with one $^{27}Al^+$ ancillary ion and two $^{25}Mg^+$ qubit ions. The ions are trapped in a linear RF Paul trap [Rowe 02], with trap frequencies for a single $^{25}Mg^+$ ion $\{\omega_x, \omega_y, \omega_z\} = 2\pi \times \{5.54, 6.46, 2.55\}$ MHz where z denotes the axis of the ion chain. In $^{25}Mg^+$ we use two Zeeman sub-levels of the ground-state hyperfine manifold as a qubit. We define $|\downarrow\rangle \equiv |^2\mathrm{S}_{\frac{1}{2}}, F = 3, m_F = -3\rangle$ and $|\uparrow\rangle \equiv |^2\mathrm{S}_{\frac{1}{2}}, F = 2, m_F = -2\rangle$. In $^{27}Al^+$ the relevant qubit levels are defined as $|^1S_0\rangle \equiv |^1\mathrm{S}_0, F = \frac{5}{2}, m_F = -\frac{5}{2}\rangle$ and $|^3P_1\rangle \equiv |^3\mathrm{P}_1, F = \frac{7}{2}, m_F = -\frac{7}{2}\rangle$. The ions are loaded into the trap via photo-ionization.

The order of the ions is maintained as Mg-Mg-Al by monitoring the motional spectrum and adjusting DC voltages of the trap electrodes to regain the correct order when necessary. Specifically, we raise the DC endcap voltages and apply a radial bias field to configure a radially oriented, linear ion chain with Al at one end. Then we apply differential endcap voltages to twist the radial chain to the desired orientation and finally relax the voltages back to the experimental parameters. In the order Mg-Mg-Al, the amplitudes of

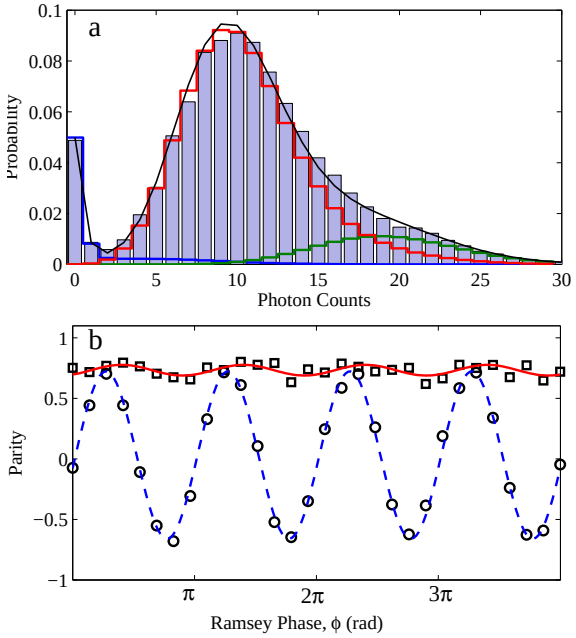

Figure 6.2: (a) Example experimental histogram of photon counts from fluorescence detection of entangled ions (bars) and its fit (dot-dashed line). The stepped lines represent calibrated histograms $P(n|0)$, $P(n|1)$, and $P(n|2)$, scaled respectively by the fit parameters $\{c_0, c_1, c_2\} = \{0.08, 0.80, 0.12\}$. This contributes to the overall fidelity with $\rho_{\downarrow\uparrow,\downarrow\uparrow} + \rho_{\uparrow\downarrow,\uparrow\downarrow} = 0.80(1)$. (b) Parity of qubit state after applying a rotation $R(\frac{\pi}{2}, \phi)$ of varying phase (squares) and the parity after first applying the rotation $R(\frac{\pi}{2}, \frac{\pi}{2})$, then applying a second rotation, $R(\frac{\pi}{2}, \phi)$, of varying phase (circles). The residual oscillation in the former case (squares) arises from small even-parity populations in ρ. The measurements give a an overall fidelity $F = 0.77(2)$.

motion for the Mg^+ ion in the in-phase mode are equal to within 1%, having a negligible impact on fidelity, while the Mg^+ ion spacing is small (3 μm) to facilitate equally strong interaction with the laser beams.

Initially, the three axial motional modes of the ions are cooled close to the ground state by resolved sideband Raman cooling of Mg^+ [Monroe 95]. This process fills the largest part of our experimental duty cycle, about 2 ms. We observe residual phonon numbers $\overline{n} < 0.1$ for all axial modes. Optical pumping ideally prepares the system in $|\downarrow\downarrow\rangle|^1S_0\rangle|0\rangle_M$. The preparation of $|D_2^{(1)}\rangle$ starts with a laser pulse that adds one phonon to the in-phase axial mode by driving the blue sideband transition $|^1S_0\rangle|0\rangle_M \rightarrow |^3P_1\rangle|1\rangle_M$ in the Al^+ ion, changing the ion state to $|\downarrow\downarrow\rangle|^3P_1\rangle|1\rangle_M$. Then a laser pulse removes one phonon from the in-phase mode by driving the red sideband transition in the Mg^+ ions. This ideally produces the state $\frac{1}{\sqrt{2}}(|\downarrow\uparrow\rangle + |\uparrow\downarrow\rangle)|^3P_1\rangle|0\rangle_M$ [King 98].

In terms of the individual density matrix elements, the fidelity of the final Mg^+ state, ρ, is

$$F = \frac{1}{2}(\rho_{\downarrow\uparrow,\downarrow\uparrow} + \rho_{\uparrow\downarrow,\uparrow\downarrow} + \rho_{\downarrow\uparrow,\uparrow\downarrow} + \rho_{\uparrow\downarrow,\downarrow\uparrow}). \tag{6.6}$$

We measure the fidelity with the same technique used in previous experiments [Sackett 00]. The odd-parity population, $\rho_{\downarrow\uparrow,\downarrow\uparrow} + \rho_{\uparrow\downarrow,\uparrow\downarrow}$, is measured using resonance fluorescence histograms from ρ. The off-diagonal term, $\rho_{\downarrow\uparrow,\uparrow\downarrow} + \rho_{\uparrow\downarrow,\downarrow\uparrow}$, is inferred from the parities of the states obtained by applying a qubit rotation $R(\frac{\pi}{2}, \phi)$ of variable phase. Here we use the convention that $R(\theta, \phi)$ implements the transformation, $|\downarrow\rangle \rightarrow \cos\left(\frac{\theta}{2}\right)|\downarrow\rangle - ie^{-i\phi}\sin\left(\frac{\theta}{2}\right)|\uparrow\rangle$ and $|\uparrow\rangle \rightarrow -ie^{+i\phi}\sin\left(\frac{\theta}{2}\right)|\downarrow\rangle + \cos\left(\frac{\theta}{2}\right)|\uparrow\rangle$. In terms of the parity operator for two qubits,

$$\Pi = |\downarrow\downarrow\rangle\langle\downarrow\downarrow| + |\uparrow\uparrow\rangle\langle\uparrow\uparrow| - \left(|\downarrow\uparrow\rangle\langle\downarrow\uparrow| + |\uparrow\downarrow\rangle\langle\uparrow\downarrow|\right), \tag{6.7}$$

we define $\Pi(\theta, \phi) \equiv tr\left(R^\dagger(\theta, \phi)\rho R(\theta, \phi)\Pi\right)$. We can then write $\rho_{\downarrow\uparrow,\uparrow\downarrow} + \rho_{\uparrow\downarrow,\downarrow\uparrow} = \frac{1}{2}[\Pi(\frac{\pi}{2}, 0) + \Pi(\frac{\pi}{2}, \frac{\pi}{2})]$. A signature of the state $|D_2^{(1)}\rangle$ is that it produces an even parity state independent of the $\pi/2$ analysis pulse phase.

We detect the state of the Mg^+ qubit by applying $\sigma-$polarized laser pulse of duration 200 μs resonant with the $|\downarrow\rangle \rightarrow |^2\mathrm{P}_{\frac{3}{2}}, F = 4, m_F = -4\rangle$ cycling transition and counting photons. We fit observed photon histograms to a weighted sum of the distributions $P(n|0)$, $P(n|1)$ and $P(n|2)$, which correspond to the probability of observing n photons given 0, 1 or 2 ions in the state $|\downarrow\rangle$. Assuming equal illumination and equal photon collection efficiency for the two ions, we can write the distributions above in terms of single-ion count distributions as

$$P(n|0) = P_{BG}(n) * P_\uparrow(n) * P_\uparrow(n) \tag{6.8}$$

$$P(n|1) = P_{BG}(n) * P_\uparrow(n) * P_\downarrow(n) \tag{6.9}$$

$$P(n|2) = P_{BG}(n) * P_\downarrow(n) * P_\downarrow(n), \tag{6.10}$$

where $G(n) * H(n) \equiv \sum_{m \leq n} G(n-m)H(m)$ is the discrete convolution of the distributions G and H. Here the convolved distributions refer to photon count probabilities from background scattering (BG), as well as the two qubit states $|\downarrow\rangle$ and $|\uparrow\rangle$. In the case of $P_\uparrow(n)$ we account for off-resonant repumping from $|\uparrow\rangle$ to $|\downarrow\rangle$ by assuming an exponential decay rate, γ, such that if the ion began in $|\uparrow\rangle$, the state probabilities at time t

are given by $c_\uparrow = e^{-\gamma t}$ and $c_\downarrow = 1 - c_\uparrow$ [Langer 06]. The photon count rates and repump rate that determine the distributions result from a simultaneous fit to two reference histograms taken just before or after the experiment.

In any particular measurement, we fit the unknown distribution

$$P_\rho(n) = \sum_{i=0}^{2} c_i P(n|i) \tag{6.11}$$

with $\sum_i c_i = 1$ to the observed series of N_p samples of photon counts, $\{n_1, n_2 \ldots n_{N_p}\}$. We use a maximum likelihood method where we maximize the quantity

$$L = \prod_{j=1}^{N_p} P_\rho(n_j) \tag{6.12}$$

by adjusting the parameters c_i.

An example of the results of measuring photon counts from the entangled state as well as a fit to the distribution are shown in Fig. 6.2(a). We measure odd-parity populations of the initial entangled state of $c_1 = -0.80(1)$. In Fig. 6.2(b) we display the measured parity of our state as a function of the phase of the analysis pulse (squares) as well as a sinusoidal fit. The mean value of $\Pi(\frac{\pi}{2}, 0)$ and $\Pi(\frac{\pi}{2}, \frac{\pi}{2})$ is 0.74(2). These numbers together yield an overall fidelity of $F = 0.77(2)$. To further confirm the presence of entanglement, we applied the pulse $R(\frac{\pi}{2}, 0)$ to ρ followed by a second analysis pulse $R(\frac{\pi}{2}, \phi)$ of varying phase (circles), again measuring the parity of the final state. Here we observe quantum state interference in the sinusoidal parity oscillation with a period of π and an amplitude of 0.70(3).

Several experimental imperfections contribute to the overall infidelity of $1 - F = 0.23(2)$. The largest error stems from random failures to optically pump to the Al^+ $|^1S_0, m_F = -\frac{5}{2}\rangle$ ground state at the 10 % level, which has been tested in separate experiments. The next largest error is due to beam pointing fluctuations. If the two Mg^+ ions are unequally illuminated by the Raman beams during the entangling pulse, two errors arise. The state amplitudes will accumulate a differential phase due to unequal Stark shifts and the state probabilities will be different due to unequal coupling strengths. We balance the Stark shifts by suppressing the beating of fringes in a Ramsey experiment, in which each Raman beam is applied separately during the wait period. Even at the optimum beam position, beam pointing fluctuations can cause errors, which we estimate to be approximately 5 %. Additional errors are caused by imperfect ground-state cooling

of the in-phase mode of motion (0.05 quanta remaining, 3 % infidelity), Al^+ decoherence from laser and magnetic field noise (3 % infidelity), and Al^+ spontaneous emission (300 us upper state lifetime) during the $|^1S_0\rangle|0\rangle_M \rightarrow |^3P_1\rangle|1\rangle_M$ pulse ($15\,\mu s$ pulse duration, 1 % infidelity). These estimated errors add to 0.22 and agree with the experimental fidelity.

In summary, we have explored numerically and experimentally a protocol for the creation of Dicke states in a trapped ion chain. The pulse sequence we use involves just two consecutive laser pulses, tuned to the resonance of a motional sideband and addressing all ions simultaneously. Infidelities due to unequal ion masses and inequivalent positions in the chain can be small ($\ll 1\%$) for creating W states, and the infidelity for creating Dicke states of two and three excitations can be sufficiently low to enable future interesting experiments. We have demonstrated the basic features of the process on an ion chain composed of two Mg^+ ions coupled to a single Al^+. If the technical errors observed in this demonstration are reduced, scaling the experiment to a larger number of ions would require the same number of steps, which makes it an attractive method for enabling the study of multipartite entangled states.

Bibliography

[Acton 06] M. Acton, K.-A. Brickman, P.C. Haljan, P.J. Lee, L. Deslauriers & C. Monroe. Near-Perfect Simultaneous Measurement of a Qubit Register. Quant. Inf. Comp., vol. 6, no. 6, pages 465–482, 2006.

[Armen 02] Michael A. Armen, John K. Au, John K. Stockton, Andrew C. Doherty & Hideo Mabuchi. Adaptive Homodyne Measurement of Optical Phase. Phys. Rev. Lett., vol. 89, no. 13, page 133602, Sep 2002.

[Aspect 82] Alain Aspect, Jean Dalibard & Gérard Roger. Experimental Test of Bell's Inequalities Using Time- Varying Analyzers. Phys. Rev. Lett., vol. 49, no. 25, pages 1804–1807, Dec 1982.

[Barrett 03] M. D. Barrett, B. Demarco, T. Schaetz, V. Meyer, D. Leibfried, J. Britton, J. Chiaverini, W. M. Itano, B. Jelenkovic, J. D. Jost, C. Langer, T. Rosenband & D. J. Wineland. Sympathetic cooling of $^9Be^+$ and $^{24}Mg^+$ for quantum logic. Phys. Rev. A, vol. 68, no. 4, page 042302, October 2003.

[Bell 64] J. S. Bell. On the Einstein Podolsky Rosen Paradox. Physics, vol. 1, pages 195–200, 1964.

[Benhelm 08] Jan Benhelm, Gerhard Kirchmair, Christian F. Roos & Rainer Blatt. Towards fault-tolerant quantum computing with trapped ions. Nat. Phys., vol. 4, no. 6, pages 463–466, 2008.

[Bennett 84] C.H. Bennett, G. Brassardet al. Quantum cryptography: Public key distribution and coin tossing. In Proceedings of IEEE International Conference on Computers, Systems and Signal Processing, volume 175. Bangalore, India, 1984.

[Bergquist 86] J. C. Bergquist, Randall G. Hulet, Wayne M. Itano & D. J. Wineland. Observation of Quantum Jumps in a Single Atom. Phys. Rev. Lett., vol. 57, no. 14, pages 1699–1702, Oct 1986.

[Bergquist 92] J. C. Bergquist, W. M. Itano & D. J. Wineland. Laser Stabilization to a Single Ion. In T. W. Hansch & M. Inguscio, editeurs, Proc. 1992 Intl. School Phys., pages 359 – 376. North-Holland, Amsterdam, 1992.

[Bergquist 10] J. C. Bergquist. private communication, 2010.

[Berkeland 98] D. J. Berkeland, J. D. Miller, J. C. Bergquist, W. M. Itano & D. J. Wineland. Minimization of ion micromotion in a Paul trap. Journal of Applied Physics, vol. 83, no. 10, pages 5025–5033, 1998.

[Blakestad 09] R. B. Blakestad, C. Ospelkaus, A. P. VanDevender, J. M. Amini, J. Britton, D. Leibfried & D. J. Wineland. High-Fidelity Transport of Trapped-Ion Qubits through an [bold X]-Junction Trap Array. Physical Review Letters, vol. 102, no. 15, page 153002, 2009.

[Blinov 02] B. B. Blinov, L. Deslauriers, P. Lee, M. J. Madsen, R. Miller & C. Monroe. Sympathetic cooling of trapped $Cd+$ isotopes. Phys. Rev. A, vol. 65, no. 4, page 040304, Apr 2002.

[Braginsky 96] V. B. Braginsky & F. Ya. Khalili. Quantum nondemolition measurements: the route from toys to tools. Rev. Mod. Phys., vol. 68, no. 1, pages 1–11, Jan 1996.

[Caves 80] Carlton M. Caves, Kip S. Thorne, Ronald W. Drever, Vernon D. Sandberg & Mark Zimmermann. On the measurement of a weak classical force coupled to a quantum-mechanical oscillator. I. Issues of principle. Rev. Mod. Phys., vol. 52, no. 2, page 341, April 1980.

[Chou 10] C. W. Chou, D. B. Hume, J. C. J. Koelemeij, D. J. Wineland & T. Rosenband. Frequency Comparison of Two High-Accuracy $Al+$ Optical Clocks. Phys. Rev. Lett., vol. 104, no. 7, page 070802, Feb 2010.

[Cirac 95] J. I. Cirac & P. Zoller. Quantum Computations with Cold Trapped Ions. Phys. Rev. Lett., vol. 74, no. 20, pages 4091–4094, May 1995.

[Cook 07] Robert L. Cook, Paul J. Martin & J. M. Geremia. Optical coherent state discrimination using a closed-loop quantum measurement. Nature, vol. 446, no. 7137, pages 774–777, 2007.

[Dehmelt 75] H. G. Dehmelt. Bull. Am. Phys. Soc., vol. 20, no. 60, 1975.

[Dehmelt 81] H. Dehmelt. Mono-ion oscillator as potential ultimate laser frequency standard. In Annual Frequency Control Symposium, 35 th, Philadelphia, PA, pages 596–601, 1981.

[DeMille 02] D. DeMille. Quantum Computation with Trapped Polar Molecules. Phys. Rev. Lett., vol. 88, no. 6, page 067901, Jan 2002.

[Deslauriers 06] L. Deslauriers, S. Olmschenk, D. Stick, W. K. Hensinger, J. Sterk & C. Monroe. Scaling and Suppression of Anomalous Heating in Ion Traps. Physical Review Letters, vol. 97, no. 10, page 103007, 2006.

[Deutsch 85] D. Deutsch. Quantum theory, the Church-Turing principle and the universal quantum computer. Royal Society of London Proceedings Series A, vol. 400, pages 97–117, July 1985.

[Dicke 54] R. H. Dicke. Coherence in Spontaneous Radiation Processes. Phys. Rev., vol. 93, no. 1, page 99, Jan 1954.

[Diedrich 89] F. Diedrich, J. C. Bergquist, Wayne M. Itano & D. J. Wineland. Laser Cooling to the Zero-Point Energy of Motion. Phys. Rev. Lett., vol. 62, no. 4, pages 403–406, Jan 1989.

[DiVincenzo 01] D. P. DiVincenzo. Scalable quantum computers. Wiley-VCH, Berlin, 2001.

[Dubessy 09] R. Dubessy, T. Coudreau & L. Guidoni. Electric field noise above surfaces: A model for heating-rate scaling law in ion traps. Physical Review A (Atomic, Molecular, and Optical Physics), vol. 80, no. 3, page 031402, 2009.

[Dür 00] W. Dür, G. Vidal & J. I. Cirac. Three qubits can be entangled in two inequivalent ways. Phys. Rev. A, vol. 62, no. 6, page 062314, 2000.

[Dür 01] W. Dür. Multipartite entanglement that is robust against disposal of particles. Phys. Rev. A, vol. 63, no. 2, page 020303, 2001.

[Einstein 17] A. Einstein. On the quantum theory of radiation. Phys. Z, vol. 18, pages 121–128, 1917.

[Einstein 35] A. Einstein, B. Podolsky & N. Rosen. Can Quantum-Mechanical Description of Physical Reality Be Considered Complete? Phys. Rev., vol. 47, no. 10, pages 777–780, May 1935.

[Ghosh 95] P. K. Ghosh. Ion traps. Clarendon, Oxford, 1995.

[Gleyzes 07] Sbastien Gleyzes, Stefan Kuhr, Christine Guerlin, Julien Bernu, Samuel Delglise, Ulrich B. Hoff, Michel Brune, Jean-Michel Raimond & Serge Haroche. Quantum jumps of light recording the birth and death of a photon in a cavity. Nature, vol. 446, no. 7133, pages 297–300, 2007.

[Gordon 54] J. P. Gordon, H. J. Zeiger & C. H. Townes. Molecular Microwave Oscillator and New Hyperfine Structure in the Microwave Spectrum of N$H3$. Phys. Rev., vol. 95, no. 1, pages 282–284, Jul 1954.

[Hafele 72] J. C. Hafele & R. E. Keating. Around-the-World Atomic Clocks: Predicted Relativistic Time Gains. Science, vol. 177, pages 166–168, 1972.

[Häffner 05] H. Häffner, W. Hänsel, C. F. Roos, J. Benhelm, D. Chek-Al-Kar, M. Chwalla, T. Körber, U. D. Rapol, M. Riebe, P. O. Schmidt, C. Becher, O. Gühne, W. Dür & R. Blatt. Scalable multiparticle entanglement of trapped ions. Nature, vol. 438, no. 7068, pages 643–646, 2005.

[Hansch 80] T.W. Hansch & B. Couillaud. Laser frequency stabilization by polarization spectroscopy of a reflecting reference cavity. Optics Communications, vol. 35, no. 3, pages 441 – 444, 1980.

[Haroche 06] S. Haroche & J.-M. Raimond. Exploring the quantum. Oxford University Press, Oxford, 2006.

[Hensinger 06] W. K. Hensinger, S. Olmschenk, D. Stick, D. Hucul, M. Yeo, M. Acton, L. Deslauriers, C. Monroe & J. Rabchuk. T-junction ion trap array for two-dimensional ion shuttling, storage, and manipulation. Applied Physics Letters, vol. 88, no. 3, page 034101, 2006.

[Holland 90] M. J. Holland, M. J. Collett, D. F. Walls & M. D. Levenson. Nonideal quantum nondemolition measurements. Phys. Rev. A, vol. 42, no. 5, pages 2995–3005, Sep 1990.

[Home 09] J.P. Home, D. Hanneke, J.D. Jost, J.M. Amini, D. Leibfried & D.J. Wineland. Complete methods set for scalable ion trap quantum information processing. Science, vol. 325, no. 5945, page 1227, 2009.

[Hume 07] D. B. Hume, T. Rosenband & D. J. Wineland. High-Fidelity Adaptive Qubit Detection through Repetitive Quantum Nondemolition Measurements. Phys. Rev. Lett., vol. 99, no. 12, page 120502, 2007.

[Hume 09] D. B. Hume, C. W. Chou, T. Rosenband & D. J. Wineland. Preparation of Dicke states in an ion chain. Phys. Rev. A, vol. 80, no. 5, page 052302, Nov 2009.

[Insight 08] Nature Insight. Nature, vol. 453, no. 7198, June 2008.

[Itano 82] Wayne M. Itano, L. L. Lewis & D. J. Wineland. Shift of ${}^2S_{\frac{1}{2}}$ hyperfine splittings due to blackbody radiation. Phys. Rev. A, vol. 25, no. 2, pages 1233–1235, Feb 1982.

[James 98] DFV James. Quantum dynamics of cold trapped ions with application to quantum computation. Applied Physics B: Lasers and Optics, vol. 66, no. 2, pages 181–190, 1998.

[Jones 00] D.J. Jones, S.A. Diddams, J.K. Ranka, A. Stentz, R.S. Windeler, J.L. Hall & S.T. Cundiff. Carrier-envelope phase control of femtosecond mode-locked lasers and direct optical frequency synthesis. Science, vol. 288, no. 5466, page 635, 2000.

[Jost 09] J. D. Jost, J. P. Home, J. M. Amini, D. Hanneke, R. Ozeri, C. Langer, J. J. Bollinger, D. Leibfried & D. J. Wineland. Entangled mechanical oscillators. Nature, vol. 459, no. 7247, pages 683–685, June 2009.

[Katz 06] N. Katz, M. Ansmann, Radoslaw C. Bialczak, Erik Lucero, R. McDermott, Matthew Neeley, Matthias Steffen, E. M. Weig, A. N. Cleland, John M. Martinis & A. N. Korotkov. Coherent State Evolution in a Superconducting Qubit from Partial-Collapse Measurement. Science, vol. 312, no. 5779, pages 1498–1500, 2006.

[Kielpinski 00] D. Kielpinski, B. E. King, C. J. Myatt, C. A. Sackett, Q. A. Turchette, W. M. Itano, C. Monroe, D. J. Wineland & W. H. Zurek. Sympathetic cooling of trapped ions for quantum logic. Phys. Rev. A, vol. 61, no. 3, page 032310, Feb 2000.

[Kielpinski 02] D. Kielpinski, C. Monroe & DJ Wineland. Architecture for a large-scale ion-trap quantum computer. Nature, vol. 417, no. 6890, pages 709–711, 2002.

[King 98] B. E. King, C. S. Wood, C. J. Myatt, Q. A. Turchette, D. Leibfried, W. M. Itano, C. Monroe & D. J. Wineland. Cooling the Collective Motion of Trapped Ions to Initialize a Quantum Register. Phys. Rev. Lett., vol. 81, no. 7, pages 1525–1528, Aug 1998.

[Lamb 47] Willis E. Lamb & Robert C. Retherford. Fine Structure of the Hydrogen Atom by a Microwave Method. Phys. Rev., vol. 72, no. 3, pages 241–243, Aug 1947.

[Langer 06] C. Langer. PhD thesis, University of Colorado, 2006.

[Leibfried 96] D. Leibfried, D. M. Meekhof, B. E. King, C. Monroe, W. M. Itano & D. J. Wineland. Experimental Determination of the Motional Quantum State of a Trapped Atom. Phys. Rev. Lett., vol. 77, no. 21, pages 4281–4285, Nov 1996.

[Leibfried 03] D. Leibfried, B. DeMarco, V. Meyer, D. Lucas, M. Barrett, J. Britton, W. M. Itano, B. Jelenkovic, C. Langer, T. Rosenband & D. J. Wineland. Experimental demonstration of a robust, high-fidelity geometric two ion-qubit phase gate. Nature, vol. 422, pages 412–415, March 2003.

[Leibfried 05] D. Leibfried, E. Knill, S. Seidelin, J. Britton, R. B. Blakestad, J. Chiaverini, D. B. Hume, W. M. Itano, J. D. Jost, C. Langer, R. Ozeri, R. Reichle & D. J. Wineland. Creation of a six-atom 'Schrödinger cat' state. Nature, vol. 438, no. 7068, pages 639–642, 2005.

[Linington 08a] I. E. Linington & N. V. Vitanov. Decoherence-free preparation of Dicke states of trapped ions by collective stimulated Raman adiabatic passage. Phys. Rev. A, vol. 77, no. 6, page 062327, 2008.

[Linington 08b] I. E. Linington & N. V.Vitanov. Robust creation of arbitrary-sized Dicke states of trapped ions by global addressing. Phys. Rev. A, vol. 77, no. 1, page 010302, 2008.

[López 07] C. E. López, J. C. Retamal & E. Solano. Selective control of the symmetric Dicke subspace in trapped ions. Physical Review A (Atomic, Molecular, and Optical Physics), vol. 76, no. 3, page 033413, 2007.

[Lupascu 06] A. Lupascu, E. F. C. Driessen, L. Roschier, C. J. P. M. Harmans & J. E. Mooij. High-Contrast Dispersive Readout of a Superconducting Flux Qubit Using a Nonlinear Resonator. Phys. Rev. Lett., vol. 96, no. 12, 2006.

[Lupascu 07] A. Lupascu, S. Saito, T. Picot, P. C. de Groot, C. J. P. M. Harmans & J. E. Mooij. Quantum non-demolition measurement of a superconducting two-level system. Nat Phys, vol. 3, no. 2, page 119, February 2007.

[Ma 94] L.S. Ma, P. Jungner, J. Ye & J.L. Hall. Delivering the same optical frequency at two places: accurate cancellation of phase noise introduced by an optical fiber or other time-varying path. Opt. Lett, vol. 19, pages 1777–1779, 1994.

[Maiman 60] T.H. Maiman. Stimulated optical radiation in ruby. Nature, vol. 187, no. 4736, pages 493–494, 1960.

[Major 05] F. G. Major, V. N. Gheorghe & G. Werth. Charged particle traps. Springer, Berlin, Heidelberg, 2005.

[Matsukevich 08] D. N. Matsukevich, P. Maunz, D. L. Moehring, S. Olmschenk & C. Monroe. Bell Inequality Violation with Two Remote Atomic Qubits. Phys. Rev. Lett., vol. 100, no. 15, page 150404, Apr 2008.

[McLachlan 47] N. W. McLachlan. Theory and applications of mathieu functions. Clarendon Press, Oxford, 1947.

[Meekhof 96] D. M. Meekhof, C. Monroe, B. E. King, W. M. Itano & D. J. Wineland. Phys. Rev. Lett., vol. 76, no. 11, pages 1796–1799, Mar 1996.

[Metcalf 99] H. Metcalf & P. van der Straten. Laser cooling and trapping. Springer, 1999.

[Meunier 06] T. Meunier, I. T. Vink, L. H. Willems van Beveren, F. H. L. Koppens, H. P. Tranitz, W. Wegscheider, L. P. Kouwenhoven, & L. M. K. Vandersypen. Nondestructive Measurements of Electron Spins in a Quantum Dot. Phys. Rev. B, vol. 74, no. 19, page 195303, 2006.

[Monroe 95] C. Monroe, D. M. Meekhof, B. E. King, S. R. Jefferts, W. M. Itano, D. J. Wineland & P. Gould. Resolved-Sideband Raman Cooling of a Bound Atom to the 3D Zero-Point Energy. Phys. Rev. Lett., vol. 75, no. 22, page 4011, November 1995.

[Morris 83] James R. Morris & Bruce W. Shore. Reduction of degenerate two-level excitation to independent two-state systems. Phys. Rev. A, vol. 27, no. 2, pages 906–912, Feb 1983.

[Motz 67] H. Motz & C.J.H. Watson. The Radio-Frequency Confinement and Acceleration of Plasmas. volume 23 of Advances in Electronics and Electron Physics, pages 153 – 302. Academic Press, 1967.

[Nagourney 86] Warren Nagourney, Jon Sandberg & Hans Dehmelt. Shelved optical electron amplifier: Observation of quantum jumps. Phys. Rev. Lett., vol. 56, no. 26, pages 2797–2799, Jun 1986.

[Nielsen 00] M. A. Nielsen & I. L. Chuang. Quantum computation and quantum information. Cambridge University Press, Cambridge, England, 2000.

[Parker 10] Thomas E Parker. Long-term comparison of caesium fountain primary frequency standards. Metrologia, vol. 47, no. 1, page 1, 2010.

[Paul 90] W Paul. Electromagnetic traps for charged and neutral particles. vol. 62, pages 531–540, 1990.

[Peil 99] S. Peil & G. Gabrielse. Observing the Quantum Limit of an Electron Cyclotron: QND Measurements of Quantum Jumps between Fock States. Phys. Rev. Lett., vol. 83, no. 7, page 1287, 1999.

[Prestage 89] J. D. Prestage, G. J. Dick & L. Maleki. New ion trap for frequency standard applications. Journal of Applied Physics, vol. 66, no. 3, pages 1013–1017, 1989.

[Preston 96] Daryl W. Preston. Doppler-free saturated absorption: Laser spectroscopy. American Journal of Physics, vol. 64, no. 11, pages 1432–1436, 1996.

[Raizen 92] M. G. Raizen, J. M. Gilligan, J. C. Bergquist, W. M. Itano & D. J. Wineland. Ionic crystals in a linear Paul trap. Phys. Rev. A, vol. 45, no. 9, pages 6493–6501, May 1992.

[Ralph 06] TC Ralph, SD Bartlett, JL OBrien, GJ Pryde & HM Wiseman. Quantum nondemolition measurements for quantum information. Physical Review A, vol. 73, no. 1, page 12113, 2006.

[Rangelov 06] A. A. Rangelov, N. V. Vitanov & B. W. Shore. Extension of the Morris-Shore transformation to multilevel ladders. Physical Review A (Atomic, Molecular, and Optical Physics), vol. 74, no. 5, page 053402, 2006.

[Retzker 07] A. Retzker, E. Solano & B. Reznik. Phys. Rev. A., vol. 75, no. 022312, 2007.

[Rosenband 07] T. Rosenband, P. O. Schmidt, D. B. Hume, W. M. Itano, T. M. Fortier, J. E. Stalnaker, K. Kim, S. A. Diddams, J. C. J. Koelemeij, J. C. Bergquist & D. J. Wineland. Observation of the $^1S_0 \rightarrow ^3P_0$ Clock Transition in $^{27}Al^+$. Physical Review Letters, vol. 98, no. 22, page 220801, 2007.

[Rosenband 08] T. Rosenband, D. B. Hume, P. O. Schmidt, C. W. Chou, A. Brusch, L. Lorini, W. H. Oskay, R. E. Drullinger, T. M. Fortier, J. E. Stalnaker, S. A. Diddams, W. C. Swann, N. R. Newbury, W. M. Itano, D. J. Wineland & J. C. Bergquist. Frequency Ratio of Al+ and Hg+ Single-Ion Optical Clocks; Metrology at the 17th Decimal Place. Science, vol. 319, no. 5871, pages 1808–1812, 2008.

[Rowe 01] MA Rowe, D. Kielpinski, V. Meyer, CA Sackett, WM Itano, C. Monroe & DJ Wineland. Experimental violation of a Bell's inequality with efficient detection. Nature, vol. 409, no. 6822, pages 791–794, 2001.

[Rowe 02] M.A. Rowe, A. Ben-Kish, B. DeMarco, D. Leibfried, V. Meyer, J. Beall, J. Britton, J. Hughes, W.M. Itano, B. Jelenkovic, C. Langer, T. Rosenband, & D.J. Wineland. Transport of quantum states and separation of ions in a dual RF ion trap. Quant. Inf. Comp., vol. 2, no. 4, pages 257–271, 2002.

[Sackett 00] C. A. Sackett, D. Kielpinski, B. E. King, C. Langer, V. Meyer, C. J. Myatt, M. Rowe, Q. A. Turchette, W. M. Itano, D. J. Wineland & C. Monroe. Experimental entanglement of four particles. Nature, vol. 404, no. 6775, pages 256–259, March 2000.

[Santarelli 99] G. Santarelli, Ph. Laurent, P. Lemonde, A. Clairon, A. G. Mann, S. Chang, A. N. Luiten & C. Salomon. Quantum Projection Noise in an Atomic Fountain: A High Stability Cesium Frequency Standard. Phys. Rev. Lett., vol. 82, no. 23, pages 4619–4622, Jun 1999.

[Sauter 86] T. Sauter, W. Neuhauser, R. Blatt & PE Toschek. Observation of quantum jumps. Physical Review Letters, vol. 57, no. 14, pages 1696–1698, 1986.

[Schaetz 05] T. Schaetz, M. D. Barrett, D. Leibfried, J. Britton, J. Chiaverini, W. M. Itano, J. D. Jost, E. Knill, C. Langer & D. J. Wineland. Enhanced Quantum State Detection Efficiency through Quantum Information Processing. Phys. Rev. Lett., vol. 94, no. 1, page 010501, 2005.

[Schmidt-Kaler 03] F. Schmidt-Kaler, H. Häffner, M. Riebe, S. Gulde, G. P. T. Lancaster, T. Deuschle, C. Becher, C. F. Roos, J. Eschner & R. Blatt. Realization of the Cirac-Zoller controlled-NOT quantum gate. Nature, vol. 422, pages 408–411, March 2003.

[Schmidt 05] P. O. Schmidt, T. Rosenband, C. Langer, W. M. Itano, J. C. Bergquist & D. J. Wineland. Spectroscopy Using Quantum Logic. Science, vol. 309, no. 5735, pages 749–752, July 2005.

[Schmidt 06] P. O. Schmidt, T. Rosenband & J. C. J. Koelemeij. Spectroscopy of atomic and molecular ions using quantum logic. In U Uggerhoj M. Drewsen & H. Knudsen, editeurs, Non-Neutral Plasma Physics VI, pages 305 – 312. American Institute of Physics, 2006.

[Schuessler 69] H. A. Schuessler, E. N. Fortson & H. G. Dehmelt. Hyperfine Structure of the Ground State of $He + 3$ by the Ion-Storage Exchange-Collision Technique. Phys. Rev., vol. 187, no. 1, page 5, Nov 1969.

[Seidelin 06] S. Seidelin, J. Chiaverini, R. Reichle, J. J. Bollinger, D. Leibfried, J. Britton, J. H. Wesenberg, R. B. Blakestad, R. J. Epstein, D. B. Hume, W. M. Itano, J. D. Jost, C. Langer, R. Ozeri, N. Shiga & D. J. Wineland. Microfabricated Surface-Electrode Ion Trap for Scalable Quantum Information Processing. Phys. Rev. Lett., vol. 96, no. 25, page 253003, Jun 2006.

[Shor 94] P. W. Shor. Algorithms for quantum computation: discrete logarithms and factoring. In SFCS '94: Proceedings of the 35th Annual Symposium on Foundations of Computer Science, pages 124–134, Washington, DC, USA, 1994. IEEE Computer Society.

[Splatt 09] F. Splatt, M. Harlander, M. Brownnutt, F. Zahringer, R. Blatt & W. Hansel. Deterministic reordering of 40Ca+ ions in a linear segmented Paul trap. New Journal of Physics, vol. 11, no. 10, page 103008, 2009.

[Stockton 03] John K. Stockton, J. M. Geremia, Andrew C. Doherty & Hideo Mabuchi. Characterizing the entanglement of symmetric many-particle spin-12 systems. Phys. Rev. A, vol. 67, no. 2, page 022112, Feb 2003.

[Turchette 00] Q. A. Turchette, Kielpinski, B. E. King, D. Leibfried, D. M. Meekhof, C. J. Myatt, M. A. Rowe, C. A. Sackett, C. S. Wood, W. M. Itano, C. Monroe & D. J. Wineland. Heating of trapped ions from the quantum ground state. Phys. Rev. A, vol. 61, no. 6, page 063418, May 2000.

[Vessot 80] R. F. C. Vessot, M. W. Levine, E. M. Mattison, E. L. Blomberg, T. E. Hoffman, G. U. Nystrom, B. F. Farrel, R. Decher, P. B. Eby, C. R. Baugher, J. W. Watts, D. L. Teuber & F. D. Wills. Test of Relativistic Gravitation with a Space-Borne Hydrogen Maser. Phys. Rev. Lett., vol. 45, no. 26, pages 2081–2084, Dec 1980.

[Walls 08] D. F. Walls & Gerard J. Milburn. Quantum optics. Springer, 2nd edition, February 2008.

[Wineland 78] D. J. Wineland, R. E. Drullinger & F. L. Walls. Radiation-Pressure Cooling of Bound Resonant Absorbers. Phys. Rev. Lett., vol. 40, no. 25, pages 1639–1642, Jun 1978.

[Wineland 79] D. J. Wineland & Wayne M. Itano. Laser cooling of atoms. Phys. Rev. A, vol. 20, no. 4, pages 1521–1540, Oct 1979.

[Wineland 98] D. J. Wineland, C. Monroe, W. M. Itano, D. Leibfried, B. E. King & D. M. Meekhof. Experimental issues in coherent quantum-state manipulation of trapped atomic ions. J. Res. NIST, vol. 103, page 259, 1998.

[Wineland 02] D. J. Wineland & et. al. Proc. symp. freq. stand. met. World Scientific, Singapore, 2002.

[Wootters 82] W. K. Wootters & W. H. Zurek. A single quantum cannot be cloned. Nature, vol. 299, no. 5886, pages 802–803, October 1982.

[Young 99] BC Young, FC Cruz, WM Itano & JC Bergquist. Visible lasers with subhertz linewidths. Physical Review Letters, vol. 82, no. 19, pages 3799–3802, 1999.